COMPUTATIONAL AND EXPERIMENTAL INVESTIGATION OF BRAZILIAN FREE-TAILED BAT EAR TUBERCLES ON AN AIRFOIL LEADING EDGE

By

SARA JOY FRESELLA FISHER

Bachelor of Science in Aerospace Engineering

Bachelor of Science in Mechanical Engineering

Oklahoma State University

Stillwater, Oklahoma

2018

Submitted to the Faculty of the
Graduate College of the
Oklahoma State University
in partial fulfillment of
the requirements for
the Degree of
MASTER OF SCIENCE
May, 2020

COMPUTATIONAL AND EXPERIMENTAL INVESTIGATION OF BRAZILIAN FREE-TAILED BAT EAR TUBERCLES ON AN AIRFOIL LEADING EDGE

Thesis Approved:

Dr. Brian R. Elbing

Thesis Adviser

Dr. Aaron S. Alexander

Dr. Jamey D. Jacob

ACKNOWLEDGEMENTS

In part, this work was supported by Dr. B. R. Elbing's Halliburton Faculty Fellowship endowed professorship.

Computational resources were provided by Oklahoma State University's High Performance Computing Center facilities.

I would like to thank Dr. Elbing and my committee for their guidance and advice on this work. I would also like to thank my lab mates for their encouragement and support, particularly Real KC, Bryce Lindsey, and Garrett Clay for their exceptional generosity in helping with my lab experiments. This work could not have been completed without their aid. Finally, I would like to thank my family: my parents Dave and Dianna Fresella for their encouragement; my daughter Georgie for her cuteness; and most importantly my husband Greg for his practical support that enabled me to complete this work, his engagement with and discussion of my research, and for his love and friendship.

Name: SARA JOY FRESELLA FISHER

Date of Degree: MAY, 2020

Title of Study: COMPUTATIONAL AND EXPERIMENTAL INVESTIGATION OF BRAZILIAN FREE-TAILED BAT EAR TUBERCLES ON AN AIRFOIL LEADING EDGE

Major Field: MECHANICAL AND AEROSPACE ENGINEERING

Abstract: Preliminary experimental data has indicated that the tubercles on Brazilian Free-Tailed bat ears, when applied to an airfoil leading edge, reduce drag and delay aerodynamic stall. This study's objective was to investigate the potential drag reduction from the tubercles using a Computational Fluid Dynamics (CFD) model that was validated against experimental data. Initial CFD simulations at Reynolds numbers (Re) of 5,600 and 16,800 and angles of attack of 0 and +/-5 degrees showed slight drag reduction at the non-zero angles, but also indicated inconsistencies with previous experimental work. New experimental data was acquired using particle image velocimetry at Re of 5,600, 16,800, and 20,700. The angle of attack was varied between 0 and 6 degrees in 2 degree increments. The CFD simulations were updated to match these new experimental conditions. At 4 and 6 degrees for Re = 20,700, the experimental and CFD data both confirmed that the tubercles reduced drag, although they differed on the drag reduction magnitude. Since the clean models matched experimental data and the drag reduction trends followed experimental trends at Re = 20,700, these simulations were assumed to be capturing the drag reduction mechanism(s). Conversely, the simulations at low angles of attack (0 and 2 degrees) as well as all angles at Re = 5,600 showed disagreement with the experiments for both the drag reduction trends and magnitudes. The experimental data in these cases exhibited high uncertainties. Improvements are required to reduce experimental uncertainty at Re = 5,600, and further mesh refinements on the tubercled cases and possible changes in flow solvers at the low Reynolds numbers are required to investigate drag reduction magnitudes. Preliminary analysis of the CFD results showed that the drag reduction was possibly caused by increased boundary layer vorticity that streamlined the wake.

TABLE OF CONTENTS

Chapter Page

Chapter Page

LIST OF TABLES

Table Page

Table Page

LIST OF FIGURES

Figure Page

Figure Page

Figure Page

Figure Page

NOMENCLATURE

α	=	angle of attack
c	=	chord
C_d	=	drag coefficient
C_l	=	lift coefficient
D	=	drag force
dt	=	time delay between laser pulses
L	=	lift force
ν	=	kinematic viscosity
p	=	percent drag reduction
ρ	=	density
Re	=	chord based Reynolds number
S	=	wing area
σ	=	uncertainty or standard deviation
U	=	local velocity
U_∞	=	freestream velocity
x	=	downstream distance from the airfoil's trailing edge
y	=	distance above and below wing thickness
z	=	distance along wing span

CHAPTER I

INTRODUCTION

In the modern age, biomimetics is becoming an increasingly pertinent field of study for many engineering applications. Especially within the fields of aerodynamics and hydrodynamics, a significant performance disparity still exists between man-made designs and their biological counterparts. Investigating these natural designs and the physical environments surrounding them can provide novel insights to reduce the gap. Scientists and researchers, recognizing this opportunity, are increasingly utilizing biomimetics to further their fields.

While biomimetics offers inspiration for countless design challenges, winged and sea creatures in particular often exhibit efficient implementation of passive flow control devices. Passive flow control devices are geometric modifications on an object's surface that generally re-energize the boundary layer by generating vortices. This re-energizing of the boundary layer, which helps the boundary layer stay attached to the surface, improves aerodynamic and hydrodynamic performance, often delaying the stall angle and decreasing drag or increasing lift. In nature, leading edge tubercles are a specific instance of these passive flow control devices. For example, Fish and Battle (1995) and others have studied the tubercles on the leading edge of a humpback whale flipper and found that these tubercles improve its hydrodynamic performance. The tubercles delay the flipper's stall and, when the flipper reaches post-stall angles of attack, increase its lift and decrease its drag (Miklosovic et al., 2004). The humpback whale possesses impressive hydrodynamic

capabilities including high maneuverability (Miklosovic et al., 2004). The flipper's tubercles clearly contribute to those capabilities, making them a worthwhile research candidate. Such drastic aerodynamic improvements as generated by these tubercles could benefit a host of engineering applications.

Brazilian free-tailed bats are another aerodynamically remarkable animal, with maximum ranges of 100 km (Williams et al., 1973), maximum flight altitudes of 3,000 m (Williams et al., 1973), and maximum flight speeds of 27 m/s (Davis et al., 1962). They also exhibit tubercles, in their case lining the leading edge of their ears. Martin (2017) and Petrin et al. (2018) hypothesized that the bat's tubercles improve its aerodynamic performance in ways similar ways to the humpback whale's tubercles. Preliminary research done by Martin (2017) and Petrin et al. (2018) suggested that the bat's tubercles do indeed delay aerodynamic stall, like the humpback whale's tubercles. They also found that these tubercles likely decrease drag but at pre-stall angles of attack as opposed to post-stall angles in the humpback whale's case (Martin, 2017; Petrin et al., 2018).

These bat ear tubercles could potentially increase the efficiency of many aerodynamics designs, from aircraft wings to wind turbine blades. To apply these tubercles to a host of applications, though, their performance must be studied for many Reynolds numbers and angles of attack. To understand their effects in different flow regimes, the flow structures generated by the tubercles must be analyzed. The current research on these tubercles has only investigated low Reynolds numbers and a small range of angles of attack (-5° to 20°). Computational models of the tubercles could quicken the research process by allowing simple adjustment of flow parameters and a straightforward method for investigating the fundamental flow structures. These models could also enable researchers to easily test different tubercle sizes and configurations, thus allowing for design optimization.

This work had three primary goals. The first goal was to create computational fluid dynamics (CFD) simulations of clean and tubercled wing sections. As mentioned previously, accurate CFD models would enable the quick investigation of the tubercles within many different flow regimes and with varying geometries. Particularly, this study's models were to investigate the tubercles' potential drag reducing properties and the study's scope was limited to small Reynolds numbers and small angles of attack. The limited scope was chosen to enable comparisons between CFD and existing experimental data and to avoid the complications associated with modeling stalled flows in CFD. The second goal of this study was to corroborate the CFD results against experimental data. With strengths and weaknesses lying in different areas, both computational and experimental analyses of the tubercle problem provide a more complete picture of the flow phenomena surrounding the tubercles. The study's third goal was to utilize the CFD models to investigate the flow structures generated by the tubercles.

CHAPTER II

LITERATURE REVIEW

2.1. Biomimetics

Researchers have increasingly begun turning to nature for innovation ideas. The biomimetics field contains a plethora of animal-inspired designs. Particularly, many winged and sea creatures have been studied for the purpose of gleaning aerodynamics and hydrodynamics insights. Choi et al. (2012) showed the research's expansive nature: Choi et al. (2012) have provided a detailed literature review of bio-inspired flow control devices, including but not limited to leading edge devices on magpie and owl feathers, trailing edge devices on swallowtail butterfly and dragonfly wings, and surface devices on dragonfly wings and scallop shells. The alula, mentioned in Choi et al. (2012), refers to the set of inboard feathers on the leading edge of birds' wings. Lee et al. (2001) studied the effects of the alula on magpie wing aerodynamics in a wind tunnel and found that the alula generated streamwise vortices at the wing tips that increased the lifting force and delayed aerodynamic stall. Ito (2009) investigated the effects of leading edge serrations, inspired by serrations on owl feathers, and found that the serrations maintained lift at higher angles of attack than a clean wing. Both of these instances exemplify passive flow control devices as seen in nature.

2.2. Humpback Whale Tubercles

Within the study of bio-inspired flow control devices, the tubercles exhibited on the humpback whale's flippers remain one of the most deeply investigated phenomena. Bushnell and Moore first proposed that the humpback whale flipper could be a worthwhile research candidate, but Fish and Battle's iconic 1995 work was the first to compare the flipper to a high aspect ratio wing and to suggest that its tubercles improved its lift and stall characteristics, possibly through vortex generation. Although humpback whales operate at much higher Reynolds numbers (~100,000 or greater), the investigative methodologies employed to research their tubercles as well as fundamental insights into their benefits and operating flow mechanisms were considered relevant to the current work.

2.2.1. Experimental Work

Miklosovic et al. (2004) used a load balance to compare a clean whale flipper model to one with tubercles on its leading edge in a wind tunnel, finding that the tubercles delayed the flipper's stall and improved both its lift and drag characteristics at angles past the stall angle. In this work (Miklosovic et al., 2004), measurements were taken with a Reynolds number of approximately 500,000 and angles of attack ranging from -2° to 20°. Other experimental investigations of the humpback whale tubercles include the work of Custodio (2007) and Hansen et al. (2011). Instead of comparing tubercled and non-tubercled flipper models, both of these works compared a wing section with tubercles along its leading edge to a clean wing section. Custodio (2007) used load cell measurements and flow visualization to examine the effects of varying the tubercles' wavelength and amplitude. Custodio's (2007) results showed that tubercle amplitude significantly affected the wing's aerodynamic performance, while wavelength did not. This work (Custodio, 2007) also confirmed that aerodynamic improvements began after the stall angle had been reached. Hansen et al. (2011) investigated similar tubercle aspects, finding that at pre-stall angles, reduced

tubercle amplitude created better aerodynamics while at post-stall angles, increased amplitude generated better aerodynamics. In general, Hansen et al. (2011) discovered that smaller wavelengths improved most aerodynamic aspects. Two additional takeaways from this work (Hansen et al., 2011) were that airfoil selection affected the tubercle performance and that the tubercles were likely behaving as vortex generators.

2.2.2. Computational Work

Computation Fluid Dynamics (CFD) techniques have been used substantially to answer further questions regarding the humpback whale tubercles. Pedro and Kobayashi (2008) used a detached eddy simulation (DES) model in the CFD program Fluent to study the flow structures caused by the tubercles. They found that the flipper's outboard section experienced leading edge stall while its inboard section experienced trailing edge stall. The improved aerodynamic performance caused by the tubercles were due to the generation of streamwise vortices that delayed trailing edge separation and confined leading edge separation to the flipper's tip (Pedro and Kobayashi, 2008). Favier et al. (2014) were able to pinpoint maximum tubercle benefits at a tubercle wavelength equal to the chord length and an amplitude equaling seven percent of the chord length. Additionally, while further investigating the flow structures caused by the tubercles, they identified a Kelvin-Helmholtz instability generating the streamwise vortices (Favier et al., 2014). Pena et al. (2019) used the program Star CCM+ to study the tubercles' performance in fully turbulent (as opposed to transitional) flow. Their simulations confirmed that the humpback whale's sinusoidal tubercles generate aerodynamic improvement post-stall but cause aerodynamic losses pre-stall. They also saw streamwise vortices re-energizing the flow within the boundary layer and also saw that in turbulent conditions, the tubercles create a thinner boundary layer that stays attached longer than a thicker would (Pena et al., 2019).

CFD simulations have also been utilized to analyze humpback whale tubercles' effects on noise reduction. Clair et al. (2013) researched a wing section with a wavy leading edge and serrations extending into the wing surface (differing from the simple humpback whale tubercles) using both experimental and computational techniques. Gathered using an anechoic wing tunnel, the experimental results demonstrated significant noise reduction compared to a clean wing section over a large frequency range and for multiple freestream velocities. Their CFD model matched the experiments fairly well, with a few deviances at certain acoustic frequencies due in some cases to computational flaws and in others to experimental defects (Clair et al., 2013). Turner and Kim (2019) investigated the acoustic effects of wavy leading edges using CFD; their results demonstrated that the noise reduction was due to flow structures found downstream of the wing, likely due to the interaction of asymmetric vortices shedding off of the upper and lower wing surfaces.

2.3. Bat Ear Tubercles

Brazilian free-tailed bats, like humpback whales, exhibit tubercles on the leading edges of their ears. With the overwhelming amount of research concluding that humpback whale tubercles increase aerodynamic performance, it is reasonable to investigate whether bat ear tubercles serve the same purpose. Preliminary experimental research on bat ear tubercles was performed by Martin (2017) and Petrin et al. (2018). In these works, the first set of tests compared the drag of a bat ear model with tubercles on its leading edge to the drag of one without. The model was obtained from the scan of a preserved bat and was scaled to be four times the true bat ear size. Particle image velocimetry (PIV) was utilized to measure wake deficits to obtain drag data, and preliminary results showed lower drag values generated by the tubercled ear than the clean ear for angles of attack less than approximately 20°. The tubercled ear drag was higher at higher angles of attack (Martin, 2017; Petrin, 2018).

To obtain more straightforward results, they then generated two NACA 0012 wing sections, one with tubercles on its leading edge and one without. The chord of these wing sections measured 112 mm and the tubercle spacing matched a loose pattern obtained from the bat's ear. Again, they ran PIV to measure the wakes behind these wings. For these wing tests, freestream velocities of 0.05, 0.15, and 0.5 m/s were used, generating chord-based Reynolds numbers of 5,600, 16,800, and 56,000, respectively. These two Reynolds numbers correspond to those experienced by a bat in cruise and by a bat in a dive (Martin, 2017; Petrin, 2018). The angles of attack tested were -5°, 0°, 5°, 8°, 10°, and 15°. The PIV measurements of these two wings demonstrated drag reduction at angles of attack less than 10° for the lower two Reynolds numbers. At the highest Reynolds number, the tubercles slightly increased the drag for some of these angles (Martin, 2017; Petrin, 2018).

Finally, a flow visualization comparison between the two wings was performed to qualitatively analyze the tubercles' effects on aerodynamic stall. These flow visualization tests were performed with a freestream velocity of 0.05 m/s ($Re = 5{,}600$) and the clean and tubercled wing angles of attack were 11.6° and 12.2°, respectively. The flow visualization showed that on the clean wing, the flow had clearly separated from the surface. On the tubercled wing, though, the flow was still attached (Martin, 2017; Petrin, 2018).

As stated in Ch. 1, the present work sough to match the experimental tests of Martin (2017) and Petrin (2018) using CFD simulations. Particularly, CFD models of the $Re = 5{,}600$ and 16,800 and -5°, 0°, and 5° angles of attack cases were made to match the clean and tubercled wing experimental tests at the same conditions.

2.4. Low Reynolds Number Airfoil Performance

One other area of research pertinent to the current work is the characterization of low Reynolds number NACA 0012 airfoil aerodynamics. Along with other low Reynolds number tests,

Laitone (1996) performed wind tunnel tests on a NACA 0012 airfoil at a Reynolds number of 20,700. Lift and drag data was gathered using a beam balance and lift coefficient versus angle of attack and drag coefficient versus lift coefficient plots were generated (Laitone, 1996). Information from these plots was used as validation of this work's CFD clean wing simulations. Additionally, Zhou et al. (2010) performed water tunnel force sensor tests on a NACA 0012 wing section for Reynolds numbers ranging from 5,300 to 51,000 and angles of attack ranging from 0° to 90°. The lift data from these measurements showed an increase in lift coefficient through 45° angle of attack and then a decrease in lift coefficient through $\alpha = 90°$. The drag data increased continuously for all angles of attack but increased less rapidly after $\alpha = 45°$. The lift coefficients increased and the drag coefficients decreased as the Reynolds number was increased from $Re = 5{,}300$ to $Re = 10{,}500$ but varied little from $Re = 10{,}500$ to $Re = 51{,}000$. This lack of variation was due to a stabilization of the flow separation point at these Reynolds numbers (Zhou et al., 2010).

CHAPTER III

SIMULATION OF PAST WORK

3.1. Introduction

The goal of this work's first phase was to produce CFD models of clean and tubercled wing sections and to compare the drag results of those CFD models to prior experimental drag results, particularly those of Martin (2017) and Petrin et al. (2018). In order to investigate the tubercles' effects on drag, Martin (2017) and Petrin (2018) first used a water tunnel to run particle image velocimetry (PIV) tests on a 3D printed version of the bat's ear. After obtaining promising drag reduction results, they simplified their method and experimentally compared water flow across a clean wing (NACA 0012 airfoil) section to a wing with tubercles on its leading edge. Again, they used PIV to perform wake analysis and calculate the drag generated by their two models. Angles of attack ranging from -5° to 15°were tested at freestream speeds ranging from 50 mm/s to 500 mm/s. These results indicated that drag on the airfoil decreased with tubercles on the leading edge for small angles of attack (less than 10 degrees) but increased at higher angles of attack. Additionally, flow visualization (dye injection) demonstrated evidence that the tubercles delayed the wing's stall (Martin, 2017; Petrin et al., 2018).

In this chapter, CFD models of the clean and tubercled airfoil tests were created, with test models and simulation conditions created to match the experimental work of Martin (2017). Particularly, this phase examined the difference between computational and experimental results

regarding drag reduction for angles of attack ranging from -5° to 5° at Reynolds numbers of 5,600 and 16,800. Much of the discussion on the CFD analysis in this chapter was included in a recent conference paper (Fisher et al., 2020).

3.2. Methods

3.2.1. Test Models

For the CFD simulations, two test models were generated in SolidWorks software (Dassault Systémes SolidWorks Corporation, Waltham, MA, USA), both matching the physical models used in Martin (2017). The first was a clean wing with a NACA 0012 airfoil cross-section, a chord of 112 mm, and a span of 300 mm. To allow for proper meshing, the tip of the airfoil's trailing edge was rounded, a slight difference from the clean wing in Martin (2017). The second test model used was based on the same clean wing but had 32 tubercles placed along its leading edge. These tubercles were conical in shape with a base diameter of 3 mm and a height of 3 mm, similar to the tubercles used in Martin (2017). The only modifications relative to the tubercled wing in Martin (2017) were that the wing's trailing edge was again rounded and the simulated tubercles were blunted at the tip, again to allow for proper meshing. Realistically, these blunted tips better matched the test model used in Martin (2017), since no physical model could achieve perfectly pointed tips. To imitate the tubercle pattern on an actual bat ear, Martin (2017) used a repeating pattern of irregularly spaced tubercles. These same locations were used in the current work. Each tubercle location is summarized in Table 1 as a percentage of the test wing's span. Both the clean and tubercled wings, schematically shown in Figure 1, were simulated in a flow-field that extended 25 chord lengths upstream of the wing, 50 chord lengths downstream of the wing, and 10 chord lengths above and below the wing. The flow-field width was 300 mm, matching the wing span. The flow domain is shown in Figure 2.

Table 1: Tubercle locations as a percentage of wing span. The same tubercle spacing is repeated every 8 tubercles following the model used in Martin (2017).

	Wing Span Percentage for Location of Each Tubercle							
Tubercles 1-8	1.0	3.5	5.5	7.8	11.3	21.0	22.0	24.0
Tubercles 9-16	26.0	28.5	30.5	32.8	36.3	46.0	47.0	49.0
Tubercles 17-24	51.0	53.5	55.5	57.8	61.3	71.0	72.0	74.0
Tubercles 25-32	76.0	78.5	80.5	82.8	86.3	96.0	97.0	99.0

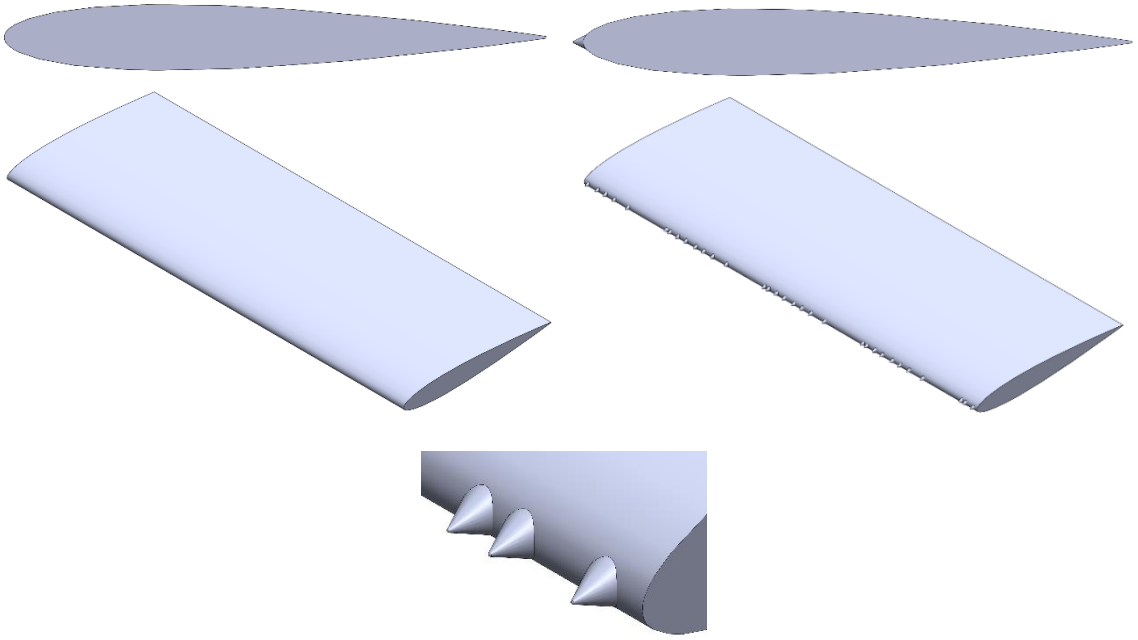

Figure 1: Airfoil cross-section (NACA 0012) and isometric view of the (left column) clean wing and (right column) tubercled wing configurations. The airfoils had a chord length of 112 mm and a span of 300 mm. Also shown is a zoomed-in view of three tubercles, each with a height and base diameter of 3 mm.

3.2.2: Simulation Conditions

The CFD program used in this study was Star CCM+ (Siemens Industry Software Incorporated, Plano, TX, United States). Both the clean and tubercled cases were investigated at two chord-length-based Reynolds numbers, Re = 5,600 and 16,800. The Reynolds number was defined as follows in Eq. (1):

$$Re = \frac{c\, U_\infty}{\nu}. \quad \textbf{(1)}$$

In Eq. (1), the chord length (c) was fixed at 112 mm and the kinematic viscosity (ν) was set to 1.00×10^{-6} m^2/s (water). Thus the two Reynolds numbers of 5,600 and 16,800 were achieved by adjusting the freestream velocity (U_∞) to 50 mm/s and 150 mm/s, respectively. These were the same Reynolds numbers that Martin (2017) tested, which were originally selected because they corresponded to the Reynolds numbers over a bat's ear at its cruise speed and maximum diving speed, respectively. While six angles of attack (−5°, 0°, 5°, 8°, 10°, and 15°) were investigated in Martin (2017), the current study focused only on small angles of attack (−5°, 0°, and 5°) to mitigate the complications associated with modelling separated flows.

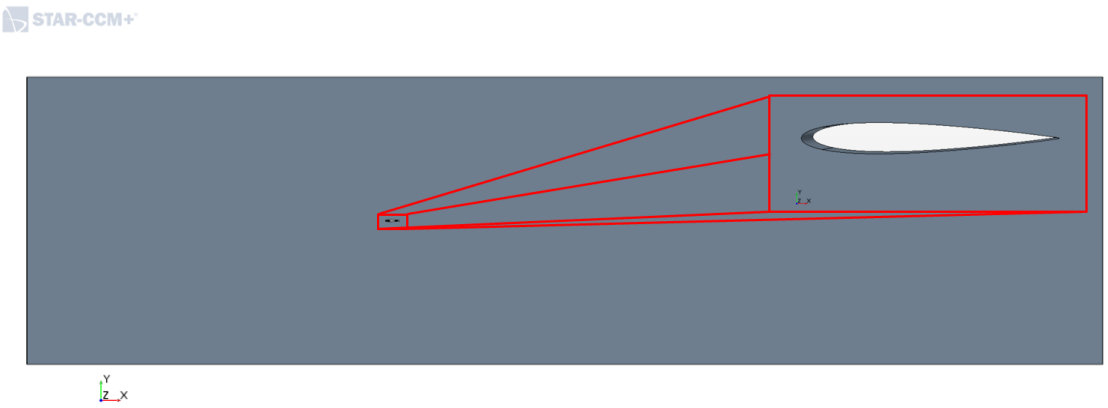

Figure 2: Flow-field surrounding the wing geometry. It extended 25 chord lengths upstream of the model, 50 chord lengths downstream of the model, 10 chord lengths above and below the model, and had a span of 300 mm.

Since the original experiments were performed in a water tunnel (Martin, 2017), the simulations used water as the working fluid and assumed steady, incompressible flow. A laminar, three-dimensional, segregated flow solver was used and cell quality remediation was applied. Finally, to allow for freestream conditions, a slip boundary condition was placed on the flow-field bottom, top, and side walls. In addition, a translational periodic boundary was applied at the side walls to create an infinite span wing.

To find the drag force (D) the pressure and shear force components in the negative x-direction were directly calculated within the simulation and then combined and recorded. Using the drag force D, the density of water ρ (997 kg/m^3), the freestream velocity U_∞, and the planform projected surface area S (0.0336 m^2); Eq. (2) was used to calculate the drag coefficient C_d:

$$C_d = \frac{D}{0.5\rho {U_\infty}^2 S}. \quad \textbf{(2)}$$

3.2.3: Mesh Conditions

A mesh refinement study was performed on the clean wing configuration at both Reynolds numbers (5,600 and 16,800) and all three angles of attack (−5°, 0°, and 5°). The basic mesh (see Figure 3), which was applied to all cases, utilized a polyhedral mesh with a base cell size of 50 mm. Also, prism layers were applied to the airfoil with a total prism layer thickness of 4 mm. The total prism layer was broken up into 20 individual layers and had an average surface size of 3.2 mm, although the surface sizes were decreased towards the leading and trailing edges. A single wake refinement was placed ahead of the airfoil, and both medium and coarse wake refinements were placed behind, above, and below the airfoil.

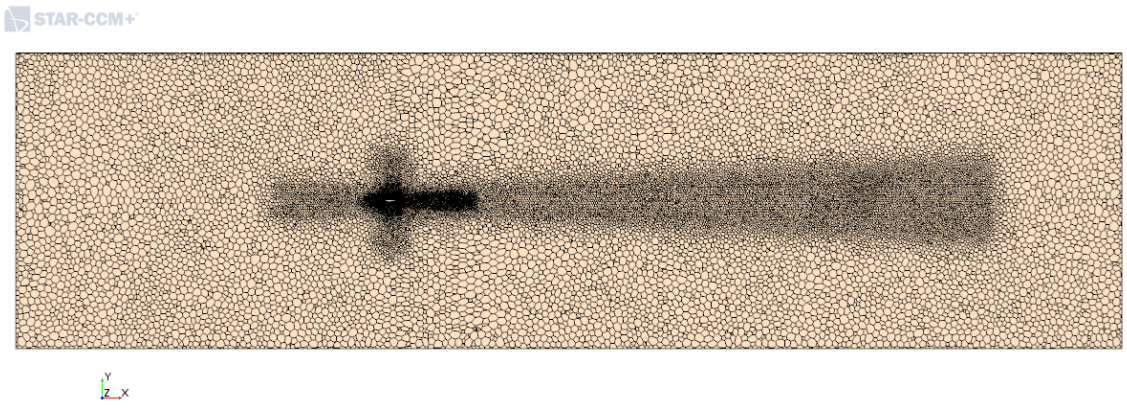

Figure 3: Global view of the meshed flow-field. The flow field totaled 8,400 mm in length, 2,240 mm in height, and 300 mm in width (into the page).

From this basic mesh, three mesh cases were created to perform the mesh refinement study. The first mesh case refined the cells right at the end of the airfoil, providing a basis for cases two and three. The second mesh case refined the medium aft wake cells, decreasing the target surface size by 20% to better capture flow information as the wake developed downstream of the airfoil. The third mesh case shortened the medium aft wake by 50% and refined it even further, decreasing mesh case two's target surface size by 75%. Mesh cases one through three are illustrated in Figure 4. After generating the three mesh cases on all the clean wing test conditions, each condition was run for 2,000 iterations using the simulation settings discussed above. As stated above, the drag coefficient was obtained from the drag force per unit span, directly calculated in each simulation. The drag coefficient percent differences between cases one and two and then between cases two and three were also found. The results of the mesh refinement study are recorded in Table 2 and are shown graphically in Figure 5.

All of the percent differences between the coarser and refined cases were within 10% of each other except for the Re = 16,800, $\alpha = 5°$ case. At this higher Reynolds number, the significant increase in drag for mesh case three was most likely due to the increased refinement capturing important drag data that the first two mesh cases were not. Since this case demonstrated improvement compared to the less refined cases, it was chosen to be compared against other experimental data.

Also, the $\alpha = -5°$ and 5° drag coefficients at Re = 16,800 were noticeably different, even though, with the NACA 0012 airfoil being symmetric, they should have been equivalent. The discrepancies between these cases were likely due to the difference in mesh sizes for these two cases. Star CCM+ generated a 9.43 million cell mesh for the $\alpha = -5°$ case (with mesh case three parameters) and a 10.8 million cell mesh for the $\alpha = 5°$ case (also with mesh case three parameters). The drag coefficients for these two angles at Re = 5,600 were nearly the same, even though the two meshes had the same cell counts as their corresponding meshes at the higher Reynolds number. At

the higher Reynolds number, the flow transports momentum at a higher rate than at the lower Reynolds number due to a higher freestream velocity. Thus, at the higher Reynolds number, a slight difference in mesh between the two angles would have produced a more noticeable difference in drag coefficients than at the lower Reynolds number.

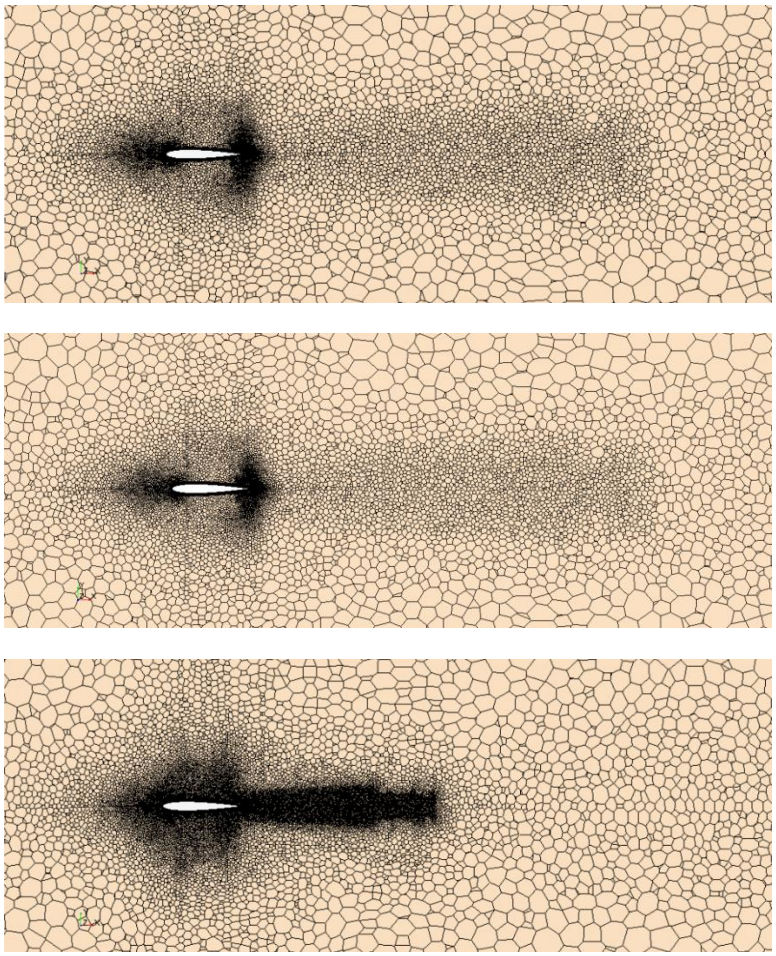

Figure 4: Mesh case (top) one, (middle) two, and (bottom) three performed for cell refinement at the trailing edge.

Table 2: Comparison of CFD drag coefficients.

Mesh Case	Re	α [deg]	Cell Count [million]	Drag Coefficient, C_d	% Difference with Preceding Mesh
1	5,600	-5	4.3	5.97E-02	--
2	5,600	-5	19.3	5.87E-02	1.66
3	5,600	-5	9.43	5.80E-02	1.35
1	5,600	0	18.3	4.82E-02	--
2	5,600	0	19.3	4.79E-02	0.59
3	5,600	0	17.1	4.73E-02	1.26
1	5,600	5	4.73	5.98E-02	--
2	5,600	5	3.82	5.99E-02	0.23
3	5,600	5	10.8	5.79E-02	3.37
1	16,800	-5	4.3	5.00E-02	--
2	16,800	-5	19.3	4.83E-02	3.61
3	16,800	-5	9.43	5.30E-02	9.37
1	16,800	0	18.3	3.01E-02	--
2	16,800	0	19.3	2.92E-02	3.17
3	16,800	0	17.1	2.85E-02	2.29
1	16,800	5	4.73	5.02E-02	--
2	16,800	5	3.82	4.63E-02	7.99
3	16,800	5	10.8	5.56E-02	18.2

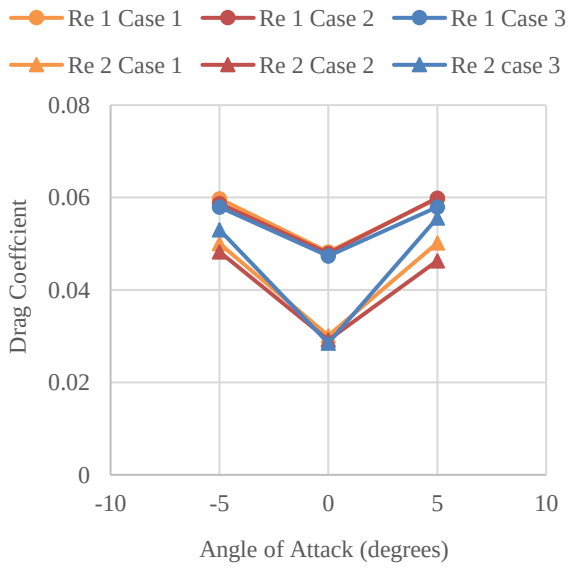

Figure 5: Drag coefficient comparison for the three mesh cases. The *Re* = 5,600 cases are the higher three data sets; the *Re* = 16,800 cases are the lower three data sets.

Table 3: Comparison of CFD drag coefficients (*Re* = 16,800) to Laitone (1996) experimental drag coefficients (*Re* = 20,700).

Mesh Case	α [deg]	Cell Count [million]	CFD C_d	Experimental (Laitone, 1996) C_d	Percent Difference
1	0	18.3	3.01E-02	3.04E-02	1.04
2	0	22.4	3.04E-02	3.04E-02	0.105
3	0	16.6	2.85E-02	3.04E-02	6.5
1	5	4.73	5.02E-02	6.14E-02	20.2
2	5	8.01	4.62E-02	6.14E-02	28.4
3	5	10.8	5.56E-02	6.14E-02	10

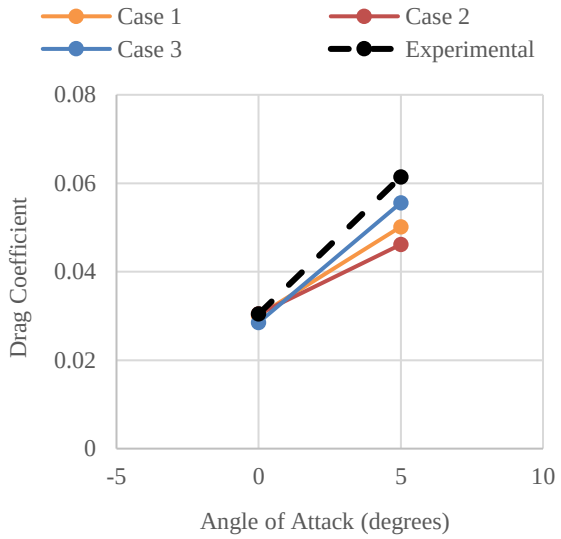

Figure 6: Drag coefficient comparison of three mesh cases (at *Re* = 16,800) to Laitone (1996) data (at *Re* = 20,700).

As a validation check, the CFD drag coefficients at *Re* = 16,800 were compared with the experimental results of Laitone (1996). Laitone (1996) reported drag coefficients at *Re* = 20,700 on a wing with an aspect ratio of 6 (as opposed to the current study's aspect ratio of approximately 2.68). The comparison between the current CFD with the various mesh refinements and the experimental results of Laitone (1996) are given in Table 3 and in Figure 6. While mesh cases one and two had values that differed significantly from the experimental results in Laitone (1996) at the 5-degree angle of attack, mesh case three produced a drag coefficient that was within 10% of the experimental result. Differences in Reynolds number could have been a major factor in the drag

coefficient variation. Because the mesh refinement was considered converged at mesh case three and mesh case three produced drag coefficients that were within 10% of Laitone (1996) at a comparable Reynolds number, mesh case three was chosen as the appropriate mesh for the current study. It was applied to all the tubercled wing scenarios as well as the clean wing scenarios. Additionally, on the tubercled cases, a refined prism layer was generated across the tubercles themselves. The total prism layer thickness was 200 μm and was broken into 15 individual layers; the target surface size was 75 μm. A view of the tubercled wing in mesh case three and a close-up of a single tubercle's mesh are provided in Figure 7. Simulations were then run for all six tubercle cases (*Re* = 5,600 and *Re* = 16,800; $\alpha = -5°$, 0°, and 5° for each Reynolds number) using the conditions mentioned previously.

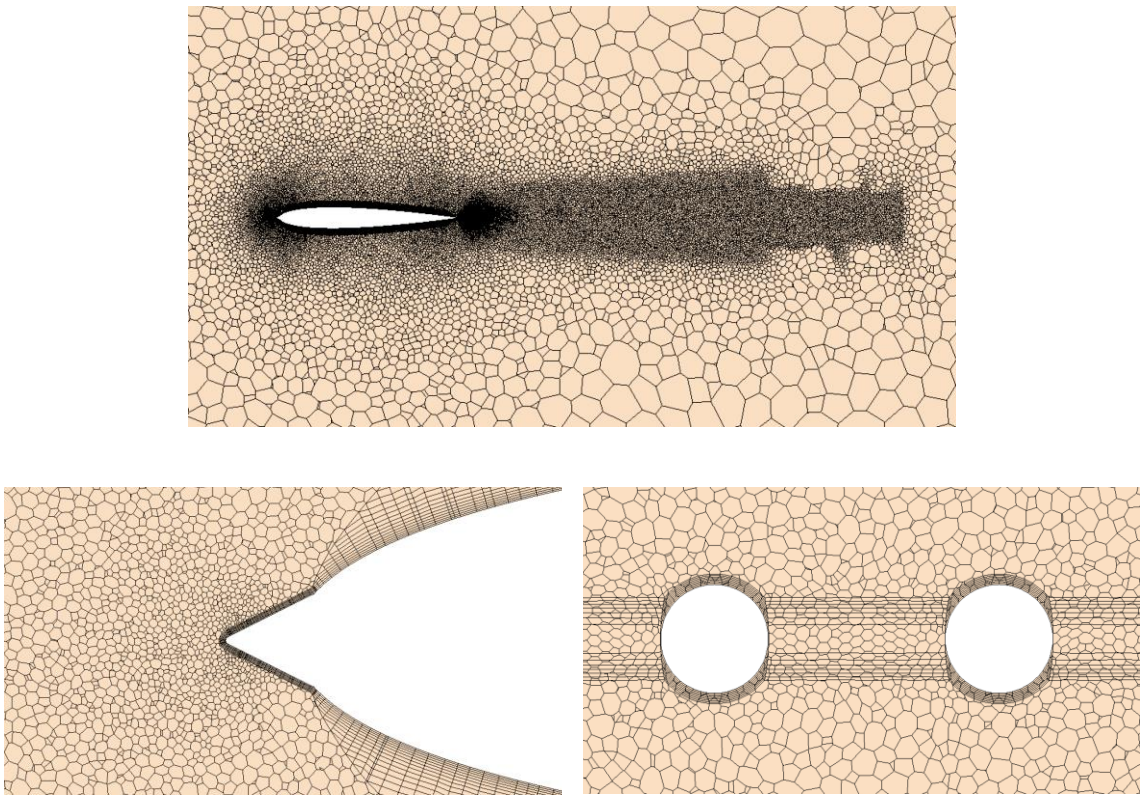

Figure 7: (top) Tubercled wing in mesh case 3 and zoomed in view of mesh surrounding an individual tubercle (bottom left) from the side and (bottom right) from the front.

3.2.4: Test Matrix

As stated previously, two principle Reynolds numbers were studied: Re = 5,600 and 16,800, matching the Reynolds numbers experienced by a bat in cruise and in a dive. These Reynolds numbers were used by Martin (2017) and corresponded to free stream velocities of 50 mm/s and 150 mm/s in water. Also, as stated above, this CFD study investigated -5, 0, and 5 degrees angle of attack, limiting the angle of attack sweep to avoid modeling separated flows. For each Reynolds number and angle of attack, both the clean and the tubercled wings were tested, and 2,000 iterations were run for each simulation. The test matrix is shown in Table 4.

Table 4: Summary of text matrix used for the CFD simulations performed to compare with Martin (2017).

Model	Re	U_∞ [m/s]	α [deg]	Iterations
Clean	5600	0.05	-5	2000
Clean	16800	0.15	-5	2000
Clean	5600	0.05	0	2000
Clean	16800	0.15	0	2000
Clean	5600	0.05	5	2000
Clean	16800	0.15	5	2000
Tubercled	5600	0.05	-5	2000
Tubercled	16800	0.15	-5	2000
Tubercled	5600	0.05	0	2000
Tubercled	16800	0.15	0	2000
Tubercled	5600	0.05	5	2000
Tubercled	16800	0.15	5	2000

3.3: Results

3.3.1: Clean Wing Results

The clean wing drag coefficients were first compared with Martin (2017). In Martin (2017), the drag coefficients were calculated from measured drag via integration of a 2D slice of the airfoil wake and then corrected for blockage effects. The current CFD simulation results were compared

against the blockage-corrected experimental values. This comparison is provided in Table 5. The comparison showed that at *Re* = 5,600, the CFD showed very poor agreement with that of Martin (2017), with percent differences reaching 40% for the non-zero angle of attacks. However, at Re = 16,800 the percent differences were significantly reduced with the differences approaching the measurement uncertainty (~10%). This suggests that the CFD simulation matched the higher Reynolds number condition of Martin (2017). A more detailed investigation is required to determine the cause for the deviation observed at the lower Reynolds number.

Table 5: Comparison of CFD and experimental (Martin, 2017) drag coefficients.

Re	α [deg]	CFD C_d	Experimental (Martin, 2017) C_d	Percent Difference
5,600	-5	5.80E-02	8.63E-02	39.3
5,600	0	4.73E-02	4.08E-02	14.7
5,600	5	5.79E-02	8.71E-02	40.3
16,800	-5	5.30E-02	5.50E-02	3.62
16,800	0	2.85E-02	2.74E-02	4.1
16,800	5	5.56E-02	6.40E-02	14.0

To assist with determining the source of the discrepancy with Martin (2017), the current CFD results with mesh case three were also compared with Xfoil drag coefficients at the corresponding Reynolds numbers. Xfoil, a widely used numerical solver for low Reynolds number aerodynamics, uses a combination of the panel method and the "dissipation integral method" to model viscous flow over an airfoil (Drela, 1989). Thus, it offered an analytically-based check for both the experimental and computational data. The comparison between the current CFD results and Xfoil is provided in Table 6. Between both Reynolds numbers and all angles of attack, the maximum difference between the current CFD results and Xfoil was 12.3%, which was consistent with the expected accuracy. The CFD simulations indicated some flow separation at the non-zero angles of attack, which was likely the cause for the observed deviations between Xfoil and the CFD

results. These differences were still relatively small, though, suggesting a reasonable match between CFD and Xfoil.

Table 6: Comparison of CFD and Xfoil drag coefficients.

Re	α [deg]	CFD C_d	Xfoil C_d	Percent Difference
5,600	-5	5.80E-02	6.56E-02	12.3
5,600	0	4.73E-02	5.14E-02	8.18
5,600	5	5.79E-02	6.56E-02	12.4
16,800	-5	5.30E-02	4.94E-02	7.02
16,800	0	2.85E-02	3.16E-02	10.1
16,800	5	5.56E-02	4.94E-02	11.8

The results from Martin (2017) were also compared with the Xfoil drag coefficients, seen in Table 7. The comparisons between Martin (2017) and Xfoil showed significant differences ranging between 11% and 28%. These differences were especially strong for all angles of attack at Re = 5,600 as well as the 5-degree angle of attack case at Re = 16,800. Although Xfoil provided an approximate solution, these differences were sufficiently large to warrant some concern about the accuracy of the data in Martin (2017). In addition, Figure 8 plots the results from the current CFD, the experiments (Martin, 2017), and Xfoil. These results showed that all three were in reasonable agreement at Re = 16,800 for all three angles of attack. Conversely, there were large deviations between Martin (2017) and the other results for Re = 5,600, especially at non-zero angles of attack. Given the reasonable comparison between the CFD and Xfoil, as well as other experiments (Laitone, 1996), the comparison suggested that there could have been an issue with the Re = 5,600 experiments of Martin (2017). Although Martin (2017) implemented a correction factor for tunnel blockage, it is possible that the blockage effects were greater than assumed. Also, since the highest percent differences were seen at non-zero angles of attack, the wake velocity measurements of Martin (2017), used in the drag calculations, could potentially have been influenced by wall effects. This was a possibility since the wake surveys were acquired far

downstream of the airfoil. Martin (2017) did not perform a spanwise assessment of the drag, which would have revealed this problem, if it existed. On the other hand, since Xfoil is an idealized

Table 7: Comparison of Martin (2017) and Xfoil drag coefficients.

Re	α [deg]	Experimental (Martin, 2017) C_d	Xfoil C_d	Percent Difference
5,600	-5	8.63E-02	6.56E-02	27.3
5,600	0	4.08E-02	5.14E-02	22.8
5,600	5	8.71E-02	6.56E-02	28.3
16,800	-5	5.50E-02	4.94E-02	10.6
16,800	0	2.74E-02	3.16E-02	14.1
16,800	5	6.40E-02	4.94E-02	25.7

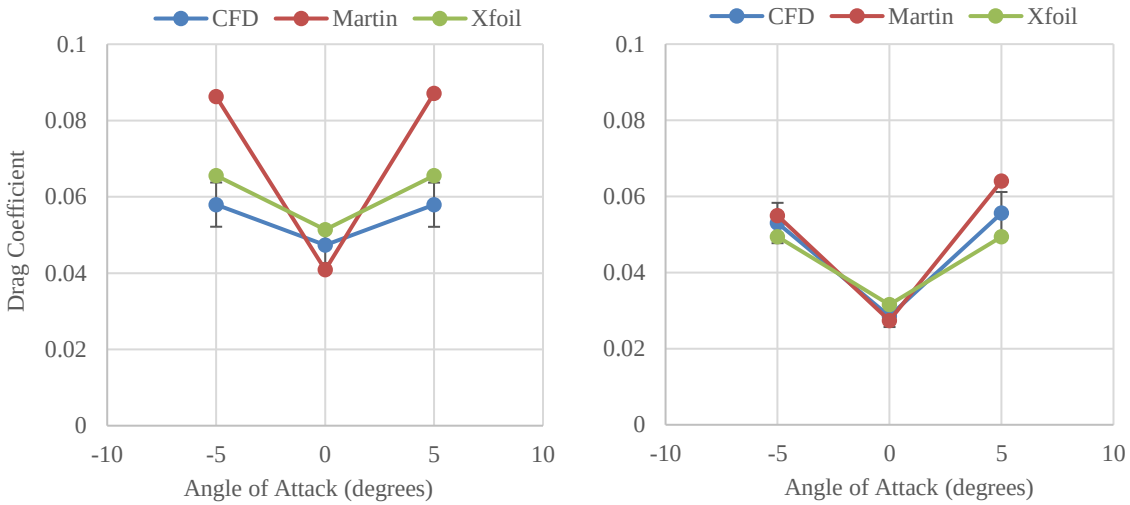

Figure 8: Comparison of CFD, experimental (Martin, 2017), and Xfoil drag coefficient results for (left) Re = 5,600 and (right) Re = 16,800.

solution, it may not have been accurately reflecting actual drag data at such a low Reynolds number, and thus the CFD models may have been missing flow information. Ultimately, the clean wing comparison between CFD, experiments (Martin, 2017), and Xfoil drag coefficient data demonstrated that new experimental data was needed to be acquired to determine if error lay within the CFD models, the experimental data, or both. At the higher Reynolds number, the relatively close comparisons between the CFD, Martin (2017), Xfoil, and Laitone (1996) data indicated that

the current CFD models provided a satisfactory starting point for the current work, but experimental investigation, especially at the lower Reynolds number, was required to better understand the differences.

3.3.2: Tubercled Wing Results

The drag force results were gathered from each tubercled wing scenario, and the drag coefficient calculated. The tubercled wing drag coefficients were then compared to the clean wing drag coefficients. The results are shown in Table 8, along with the drag coefficient percent decrease (or percent increase if a negative value). The drag coefficient results are also plotted in Figure 9. These results showed that the tubercles slightly reduced the drag across the wing at non-zero angles of attack for both Reynolds numbers. The drag increased slightly for both cases at the zero-degree angle of attack.

Table 8: Comparison of tubercled wing and clean wing drag coefficients from CFD simulations.

Re	α [deg]	Tubercled Wing C_d	Clean Wing C_d	Percent Reduction
5,600	-5	5.65E-02	5.80E-02	2.59
5,600	0	4.78E-02	4.73E-02	-1.06
5,600	5	5.68E-02	5.79E-02	1.90
16,800	-5	5.02E-02	5.30E-02	5.28
16,800	0	2.98E-02	2.85E-02	-4.56
16,800	5	5.53E-02	5.56E-02	0.54

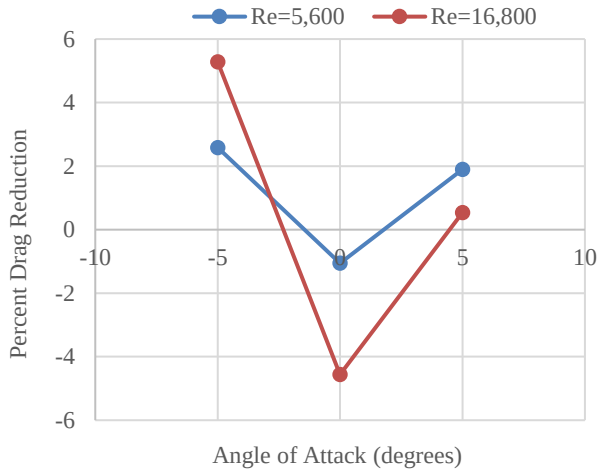

Figure 9: Percent drag reduction versus angle of attack for CFD data at Re = 5,600 and Re = 16,800.

Next, the current CFD data was compared with tubercled results from Martin (2017). The comparison is provided in Table 9 and the results are plotted in Figure 10. Similar to the data from Martin (2017), the simulations showed that the tubercles decreased the drag coefficients at non-zero degree angles of attack. Unlike Martin (2017), the simulations showed that the tubercles did not decrease drag at zero degree angle of attack. The percent differences between experimental tubercled results (Martin, 2017) and the current CFD results, though, were quite large. At Re = 5,600, similar to the clean wing case, this observation was expected and again possibly attributable to error introduced into the data (Martin, 2017) by water tunnel blockage or wall effects or to poor modeling in the CFD. At Re = 16,800, where Martin (2017) and the CFD simulations produced relatively comparable clean wing results, the cause of differences in tubercled wing results was less readily explained. Since the trends between Martin (2017) and the CFD were generally similar while the values differed, perhaps the location of wake velocity measurements in Martin (2017) (integrated to obtain drag values) was non ideal. Also, the CFD's mesh over the tubercles could have been too coarse or the simulations could not have been properly modeling the flow separation point on the airfoil. Again, a valid experiment was required to explore the deviations.

Table 9: Comparison of CFD and experimental (Martin, 2017) drag coefficients for the tubercled wings.

Re	α [deg]	CFD C_d	Experimental (Martin, 2017) C_d	Percent Difference
5,600	-5	5.65E-02	7.63E-02	29.8
5,600	0	4.78E-02	3.66E-02	26.6
5,600	5	5.68E-02	8.12E-02	35.4
16,800	-5	5.02E-02	3.99E-02	23
16,800	0	2.98E-02	1.75E-02	51.8
16,800	5	5.53E-02	4.41E-02	22.5

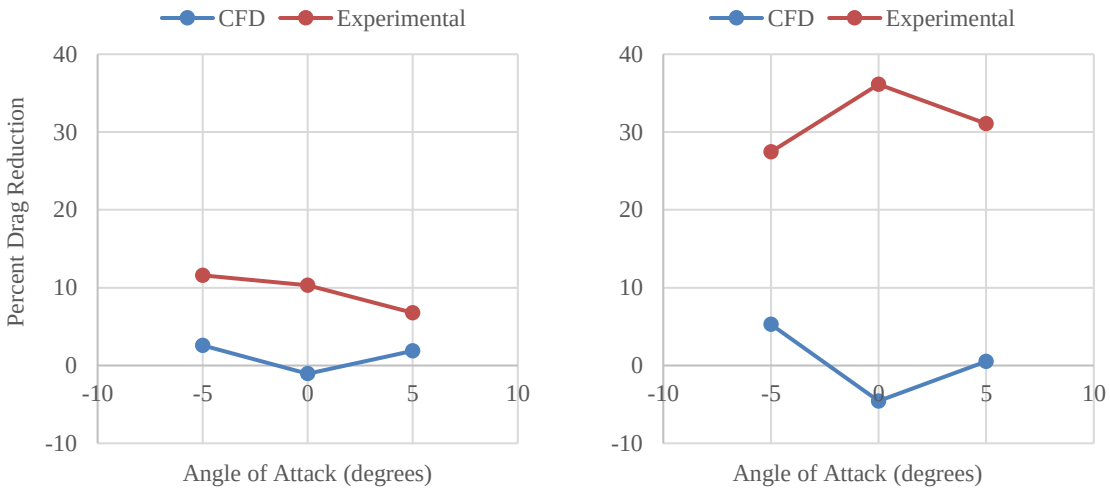

Figure 10: Comparison of percent drag reduction for both CFD and experimental (Martin, 2017) results at (left) Re = 5,600 and (right) Re = 16,800.

3.4: Simulation of Past Work Summary

The results of this portion of the study demonstrated that the CFD model used provided a starting point for examining the bat ear tubercle problem, especially at *Re* = 16,800. The clean wing mesh was refined to convergence and the resulting drag coefficients achieved satisfactory matching with Xfoil at both Reynolds numbers and with previous experiments (Laitone, 1996) at *Re* = 16,800. Conversely, Martin (2017), which also tested a tubercled airfoil, did not match either Xfoil or the current CFD data at *Re* = 5,600 in the clean wing configuration. However, there was

reasonably agreement between the clean wing studies at Re = 16,800. This led to the conclusion that new experimental data must be acquired to understand the differences between the CFD and experimental data at the lower Reynolds number.

Preliminary CFD results of the tubercled wings showed that the tubercles produced, on average, a 2.6% drag reduction at non-zero angles of attack with a standard deviation of 2.0%, a relatively small decrease. Additionally, the zero-degree angle of attack results showed a drag increase of 1.1% and 4.6% at Re = 5,600 and 16,800, respectively. Similar trends, but larger magnitudes, were observed in Martin (2017), although the experiments (Martin, 2017) also demonstrated a decrease in drag at the zero-degree angle of attack. These inconsistencies indicated that there could have been potential issues with the data from Martin (2017), but the inaccuracies within the CFD models also could have explained the different drag reduction trends. Independently repeated experiments would provide insight into either experimental limitations or computational model inaccuracies.

CHAPTER IV

EXPERIMENTAL INVESTIGATIONS

4.1: Introduction

Chapter 3's investigation showed significant differences between Xfoil and CFD model drag data and the drag coefficients in Martin (2017). It was concluded that new experimental data needed to be collected in order to investigate these differences. This chapter summarizes the experiments performed to obtain those new experimental values. A few key changes in the test models and conditions distinguished these experiments from the ones performed in Martin (2017), though. First, the tubercled wing test model was changed to have a regular tubercle spacing on the leading edge instead of an irregular spacing. This change was incorporated to remove any potential effects of irregular spacing on drag reduction. Second, a third Reynolds number, Re = 20,700, was added to the test matrix. This Reynolds number was investigated in Laitone (1996) on a clean, NACA 0012 wing section and thus provided additional comparison points for the clean wing experimental data. Third, the angle of attack sweep was changed from -5°, 0°, 5°, 8°, 10°, and 15° (Martin, 2017) to 0°, 2°, 4°, and 6°. Limiting the range to small angles of attack ensured that the wing did not reach stall conditions, preventing the need to model stalled flow in future CFD simulations. Additionally, investigating these four angles provided more data points than the small angle cases (-5°, 0°, and 5°) investigated in Martin (2017), and thus more thorough insight, into the tubercles' behavior at small angles of attack.

For these experiments, particle image velocimetry (PIV) was performed on the wing sections to investigate the tubercles' potential drag reduction characteristic. PIV was used to obtain average, two-dimensional wake profiles behind the wing test pieces (or more specifically, behind the airfoil cross section of the wings). From these wake profiles, the momentum deficit was determined and used to calculate the drag coefficient of each clean and tubercled airfoil for the different test conditions.

4.2: Methods

4.2.1: Test Models

Two test models were used in the experiments: a clean wing and a tubercled wing. Both utilized a NACA 0012 airfoil, had a chord of 112 mm, had a span of 300 mm, and had a maximum thickness of 13.4 mm. The tubercled wing had evenly-spaced tubercles along its leading edge, differing from the non-uniform spacing used in Martin (2017). Figure 11 shows the SolidWorks models used to manufacture the parts. The tubercles, conical in shape, had a base of 3 mm and a height of 3 mm. They were inset 0.67 mm into the wing from the leading edge, as shown in Figure 12. With a 6 mm spacing from apex to apex, the gap between each tubercle measured 3 mm, or one tubercled diameter. A total of 50 tubercles lined the leading edge.

The test pieces themselves were 3D printed using an FDM printer and ABS plastic. The parts were sanded and coated in 3-D epoxy (XTC, Smooth-On Incorporated, Macungie, PA, United States) to achieve a smooth surface and to prevent warping at the trailing edge.

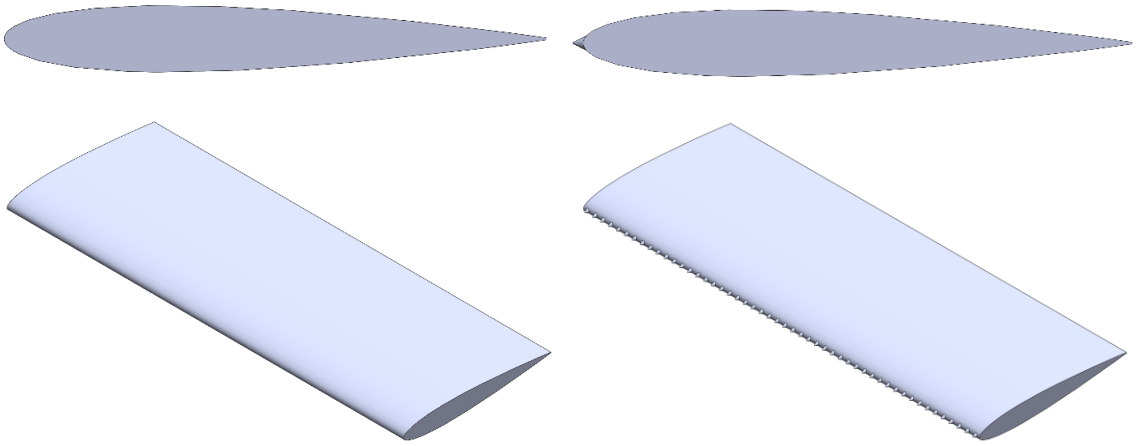

Figure 11: Cross sectional view and isometric view of the (left) clean wing and (right) tubercled wing.

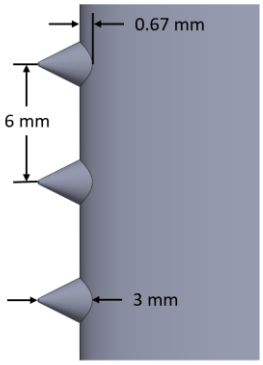

Figure 12: Detailed view of the tubercles.

4.2.2: Test Facilities and Instrumentation

The physical experiments took place in the Advanced Technology Research Center at Oklahoma State University's Stillwater Campus. They were performed using a water tunnel (model 503, Engineering Laboratory Design, Lake City, MN, United States). This closed circuit water tunnel contained a 300 by 300 by 1,140 mm test section and had a contraction ratio of six to one. The flow was driven by two pumps, each powered by a 7.5 horsepower alternating current motor. Free stream empty tunnel speeds ranged from approximately 0.01 m/s to 1 m/s.

The water was seeded with hollow glass bubbles (iM30K, 3M Company, St. Paul, MN, USA). These glass bubbles averaged 18 microns in diameter. Also, LaVision hollow glass spheres (LaVision Incorporated, Ypsilanti, MI, USA) with an average diameter of 10 microns were added during the course of the experiment. While performing experiments, one of the tunnel's two pumps was brought to full speed for a few seconds every two to three tests to ensure that the particles remained mixed.

To perform PIV analysis, a high speed camera (MotionPro X3, Integrated Design Tools, Incorporated, Pasadena, CA, USA) was utilized. This camera had a maximum resolution of 1,280 by 1,024 pixels at a rate of 1,040 frames per second. For these experiments, the initial frames within image pairs were taken at a rate of 10 frames per second; the second frame in each pair was taken after the first frame at the delay time that was set for each test (see Table 10 for delay times). The lens used for the experiments (Fujinon-TV Zoom, Fujifilm Corporation, Tokyo, Japan) had a minimum aperture of F/1.2 and a focal length ranging from 12.5 to 75 mm.

The lasers were Nd:YAG, Class IV, 532 nm lasers (Big Sky, now Quantel by Lumibird, Lannion, France). They were set to repetition rates of 10 Hertz, had a pulse duration of 8 nanoseconds, and had an energy of 30 millijoules. Additionally, a delay time (dt), was set between the two laser pulses for each freestream velocity as seen in Table 10. These delay times were set such that a given particle travelled 10 to 15 pixels in the x-direction between each image in an image pair.

Table 10: Delay times corresponding to each freestream velocity.

U_∞ [m/s]	dt [µs]
0.05	16,500 ~ 35,000
0.15	6,000 ~ 12,000
0.185	5,000 ~ 10,000

To form a laser sheet, a series of mirrors and optics pieces (Newport Corporation, Irvine, CA, USA; Thorlabs, Inc., Newton, NJ, USA; and TSI, Inc., Shoreview, MN, USA) redirected the laser and split the beam into a sheet. The lasers were controlled by two pulse generators. The first (model 4001, Global Specialties, Yorba Linda, CA, USA) controlled the width and spacing of each individual laser. The second (Plus Model 9518, Quantum Composers Incorporated, Bozeman, MT, USA) was connected in series to the first and determined the delay between the two lasers.

The wing sections were placed approximately 70 mm from the water tunnel test section inlet. Two laser sheet configurations were used because the setup had to be redone in the middle of taking data. For the $\alpha = 4°$, 5°, and 6° clean wing tests and $\alpha = 6°$ tubercled wing tests (the first setup), the laser sheet was placed 162 mm above the base of the test section. For the $\alpha = 0°$ and 2° clean wing tests and the $\alpha = 0°$, 2°, and 4° tubercled wing tests (the second setup), the laser sheet was placed 142 mm above the test section base, inadvertently shifted from the first setup. For both laser sheet configurations, the camera's field of view was centered approximately two chord lengths, or 224 mm, downstream of the wing's trailing edge. In the first laser sheet configuration, the examined field of view extended 22 mm in the x-direction and 78 mm in the y-direction. For the second laser sheet configuration, the examined field of view extended 32 mm in the x-direction and 58 mm in the y-direction. Top and side views of the experimental setup are shown in Figure 13.

The imaging was performed using MotionStudio software (version 2.12.20, Integrated Design Tools, Incorporated, Pasadena, CA, USA). At each data point, two hundred images were taken, creating one hundred image pairs. Once the images were taken, they were processed using LaVision's DaVis software (version 8.4.0, LaVision Incorporated, Ypsilanti, MI, USA). The image pairs were analyzed in a 1-2, 3-4, etc. sequence. For preprocessing, a sliding background was subtracted with a scale length of 2 pixels. A geometric mask was defined that was approximately 320 pixels in the x-direction and 900 pixels in the y-direction; for the second laser sheet setup, the

mask extended approximately 80 mm in the x-direction and approximately 130 mm in the y-direction. For vector calculation, cross-correlation was applied and two passes of 128 by 128 pixels and 16 by 16 pixels were also applied. A B-spline-6 reconstruction was applied to the final pass. For postprocessing, vectors were removed and replaced if greater than two standard deviations from the average, and groups with less than five vectors were removed. Three by three smoothing was also applied. The average and standard deviation vector fields for each test were created from each set of 100 image pairs. Figure 14 shows a sample averaged velocity vector field for a single test.

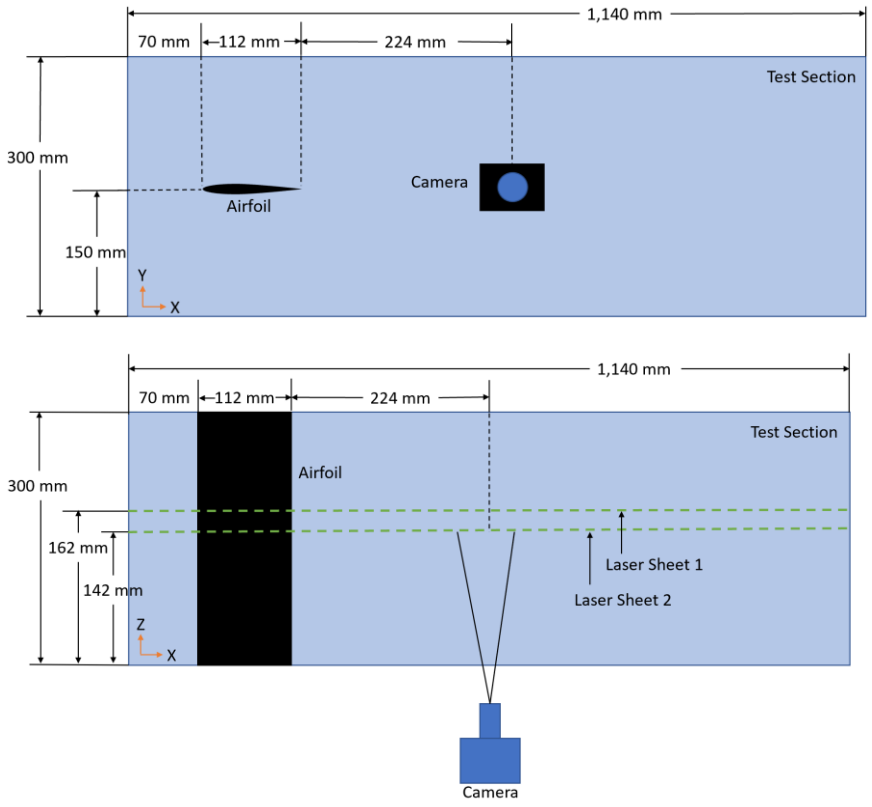

Figure 13: Experimental setup (top) top view and (bottom) side view.

To analyze the PIV averaged vector field data, a Matlab code was used. This code took the average velocity vector field (generated in DaVis from the 100 image pairs) and used it to obtain an average wake velocity profile. Figure 14 shows a sample averaged wake profile as generated by the Matlab code. From this profile, the freestream velocity U_∞ was calculated. From the freestream velocity, the Reynolds number of the flow was found using (1. A kinematic viscosity value of

1.00×10^{-6} m^2/s (water) was used, along with a chord length of 112 mm. The wake region was isolated from the freestream flow region by limiting it to a region between two y values, y_1 and y_2. Using the airfoil chord length c, the local velocity values U, the freestream velocity value U_∞, and the local height y, the drag coefficient C_d was then calculated using Eq. (3):

$$C_d = \frac{2}{c}\int_{y_1}^{y_2} \frac{U}{U_\infty}\left(1 - \frac{U}{U_\infty}\right) dy\,. \tag{3}$$

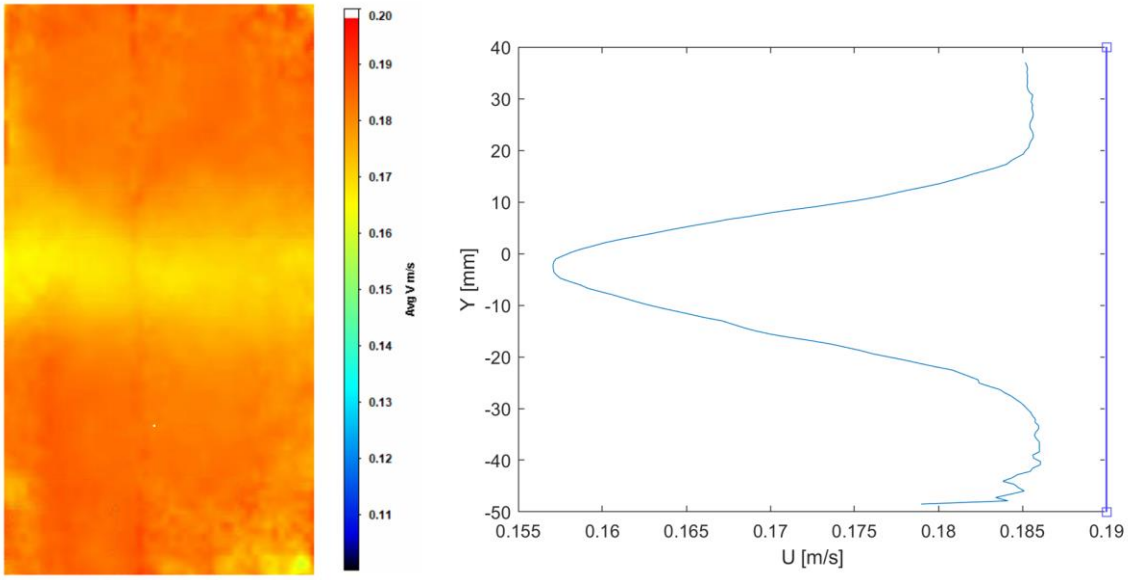

Figure 14: (Left) a sample averaged velocity vector field from DaVis from an individual test at Re = 20,700 and (right) a sample average wake profile from Matlab from an individual test at α = 6°, Re = 20,700.

In the Matlab code, the integral was calculated using the trapezoidal method. This method of calculating the drag coefficient was applied to each individual PIV test. At a given Reynolds number and angle of attack, 2-5 individual tests were performed. The resulting drag coefficients from these individual tests were averaged to find the nominal drag coefficient for the given test condition.

4.2.3: Test Matrices

The physical experiments were broken into two phases. The first phase's goal was to collect clean wing drag coefficient data in order to validate it against Xfoil and Laitone (1996) values. The second phase's goal was to compare clean wing drag coefficients to tubercled wing drag coefficients.

For the first phase, data was taken at Reynolds numbers of 5,600, 16,800, and 20,700. The corresponding freestream velocities for these Reynolds numbers were 50, 150, and 185 mm/s, respectively. The angles of attack investigated were 0°, 2°, 4°, 5°, and 6°. The even angles tested in this first phase were utilized in the second phase, and the 5° angle of attack was included as an extra point of comparison. Drag coefficients at all these angles could be compared to both Xfoil values (for all three Reynolds numbers) and Laitone (1996) values (for Re = 20,700), and the α = 0° and 5° drag coefficients could additionally be compared to the initial CFD values (for Re = 5,600 and 16,800).

For Phase 2, the Reynolds numbers of 5,600, 16,800, and 20,700 were also investigated, again corresponding to freestream velocities of 50, 150, and 185 mm/s, respectively. The angles of attack examined in this phase were 0°, 2°, 4°, and 6°. These angles were chosen to provide a thorough sweep of small angles of attack.

In both Phase 1 and 2, for each Reynolds number and angle of attack, the camera exposure was adjusted until a particle traveled between 10 and 15 pixels between images within an image pair. This camera exposure corresponded to the delay time between images within an image pair. Additionally, the camera's z-axis location was adjusted until the field of view was centered on the airfoil's wake. The camera's x-axis location was kept constant at 224 mm, or two chord lengths, behind the airfoil's trailing edge. For both phases, 200 images were taken at each run, creating 100 image pairs, and images were taken at a rate of 10 Hertz. A minimum of three repeated runs for

Table 11: Test matrix including both Phase 1 and Phase 2.

Model	Target Re	Target U [m/s]	Alpha [deg]	Rate [Hz]	Total # Frames	Phase	Target # of Runs
Clean	5,600	0.05	0	10	200	1	3
Clean	16,800	0.15	0	10	200	1	3
Clean	20,700	0.185	0	10	200	1	3
Clean	5,600	0.05	2	10	200	1	3
Clean	16,800	0.15	2	10	200	1	3
Clean	20,700	0.185	2	10	200	1	3
Clean	5,600	0.05	4	10	200	1	3
Clean	16,800	0.15	4	10	200	1	3
Clean	20,700	0.185	4	10	200	1	3
Clean	5,600	0.05	5	10	200	1	3
Clean	16,800	0.15	5	10	200	1	3
Clean	20,700	0.185	5	10	200	1	3
Clean	5,600	0.05	6	10	200	1	3
Clean	16,800	0.15	6	10	200	1	3
Clean	20,700	0.185	6	10	200	1	3
Clean	5,600	0.05	0	10	200	2	3
Clean	16,800	0.15	0	10	200	2	3
Clean	20,700	0.185	0	10	200	2	3
Clean	5,600	0.05	2	10	200	2	3
Clean	16,800	0.15	2	10	200	2	3
Clean	20,700	0.185	2	10	200	2	3
Clean	5,600	0.05	4	10	200	2	3
Clean	16,800	0.15	4	10	200	2	3
Clean	20,700	0.185	4	10	200	2	3
Clean	5,600	0.05	6	10	200	2	3
Clean	16,800	0.15	6	10	200	2	3
Clean	20,700	0.185	6	10	200	2	3
Tubercled	5,600	0.05	0	10	200	2	3
Tubercled	16,800	0.15	0	10	200	2	3
Tubercled	20,700	0.185	0	10	200	2	3
Tubercled	5,600	0.05	2	10	200	2	3
Tubercled	16,800	0.15	2	10	200	2	3
Tubercled	20,700	0.185	2	10	200	2	3
Tubercled	5,600	0.05	4	10	200	2	3
Tubercled	16,800	0.15	4	10	200	2	3
Tubercled	20,700	0.185	4	10	200	2	3
Tubercled	5,600	0.05	6	10	200	2	3
Tubercled	16,800	0.15	6	10	200	2	3
Tubercled	20,700	0.185	6	10	200	2	3

each given condition were to be taken. The test matrix including both Phase 1 and Phase 2 is shown in Table 11.

4.3: Results

4.3.1: Clean Wing Results

For phase 1, the clean wing experimental results were compared to Xfoil and Laitone (1996). The clean wing experimental drag coefficients are compared to Xfoil drag coefficients in Table 12 and, for the Re = 20,700 case, are compared to Laitone (1996) data in Table 13. Figure 15 plots these comparisons for the three Reynolds number cases.

The uncertainty designated to the experimental drag coefficients was equated to each drag coefficient's standard deviation value. Since each drag coefficient listed for each test condition was the average measurement of 2 to 5 repeated tests, a standard deviation value was obtainable for each averaged drag coefficient. The standard deviation quantified the average's lack of precision at a given test condition and was thus chosen as an accurate describer of the data's uncertainty. In the following figures, the error bars reflect each drag coefficient's standard deviation.

As Table 12 demonstrates, all of the experimental values at 4° and 6° angle of attack produced percent differences of less than 10 percent with the Xfoil values. Percent differences greater than 10 percent were seen at 0° angle of attack for Re = 16,800 and 20,700, α = 2° for all three Reynolds numbers, and α = 5° for Re = 5,600 and 16,800. All experimental drag coefficient values with less than a 10 percent difference from the Xfoil values contained the Xfoil values within their standard deviations, as illustrated in Figure 15. As seen in Table 13, the percent differences between the experimental drag coefficient values and the Laitone drag coefficient values were between 20 and 30 percent for all angles of attack except for α = 6°, displaying only a 3% difference.

Generally, except for 5° angle of attack at Re = 5,600 and 4° angle of attack at Re = 16,800, the experimental drag coefficients followed the Xfoil values' trend of increasing with angle of attack.

Table 12: Comparison of clean wing experimental and Xfoil drag coefficients.

Re	α [deg]	Experimental C_d	Xfoil C_d	Percent Difference
5,600	0	4.68E-02	5.14E-02	9.4
5,600	2	4.76E-02	5.33E-02	11.4
5,600	4	5.56E-02	6.00E-02	7.5
5,600	5	7.58E-02	6.56E-02	14.5
5,600	6	6.69E-02	7.29E-02	8.5
16,800	0	2.52E-02	3.16E-02	22.4
16,800	2	2.92E-02	3.41E-02	15.4
16,800	4	4.41E-02	4.25E-02	3.8
16,800	5	4.36E-02	4.94E-02	12.4
16,800	6	6.15E-02	6.49E-02	5.3
20,700	0	2.30E-02	2.89E-02	22.6
20,700	2	2.67E-02	3.16E-02	16.8
20,700	4	4.00E-02	4.05E-02	1.2
20,700	5	4.72E-02	4.64E-02	1.8
20,700	6	6.50E-02	6.50E-02	0.0

Table 13: Comparison of experimental and Laitone (1996) drag coefficients.

Re	α [deg]	Experimental C_d	Laitone (1996) C_d	Percent Difference
20,700	0	2.30E-02	3.04E-02	27.7
20,700	2	2.67E-02	3.55E-02	28.3
20,700	4	4.00E-02	4.89E-02	20.1
20,700	5	4.72E-02	6.14E-02	26.1
20,700	6	6.50E-02	6.31E-02	3.0

To better understand the data, the uncertainties as percentages of the drag coefficients were compared for each angle of attack at all three Reynolds numbers (see Figure 16). Almost ubiquitously (excepting α = 5° at Re = 20,700), the non-dimensionalized uncertainty decreased with increasing Reynolds number. This decreasing trend indicated that the higher Reynolds number

cases had less variance between the individual tests at each data point, whereas the lower Reynolds number cases had more variance.

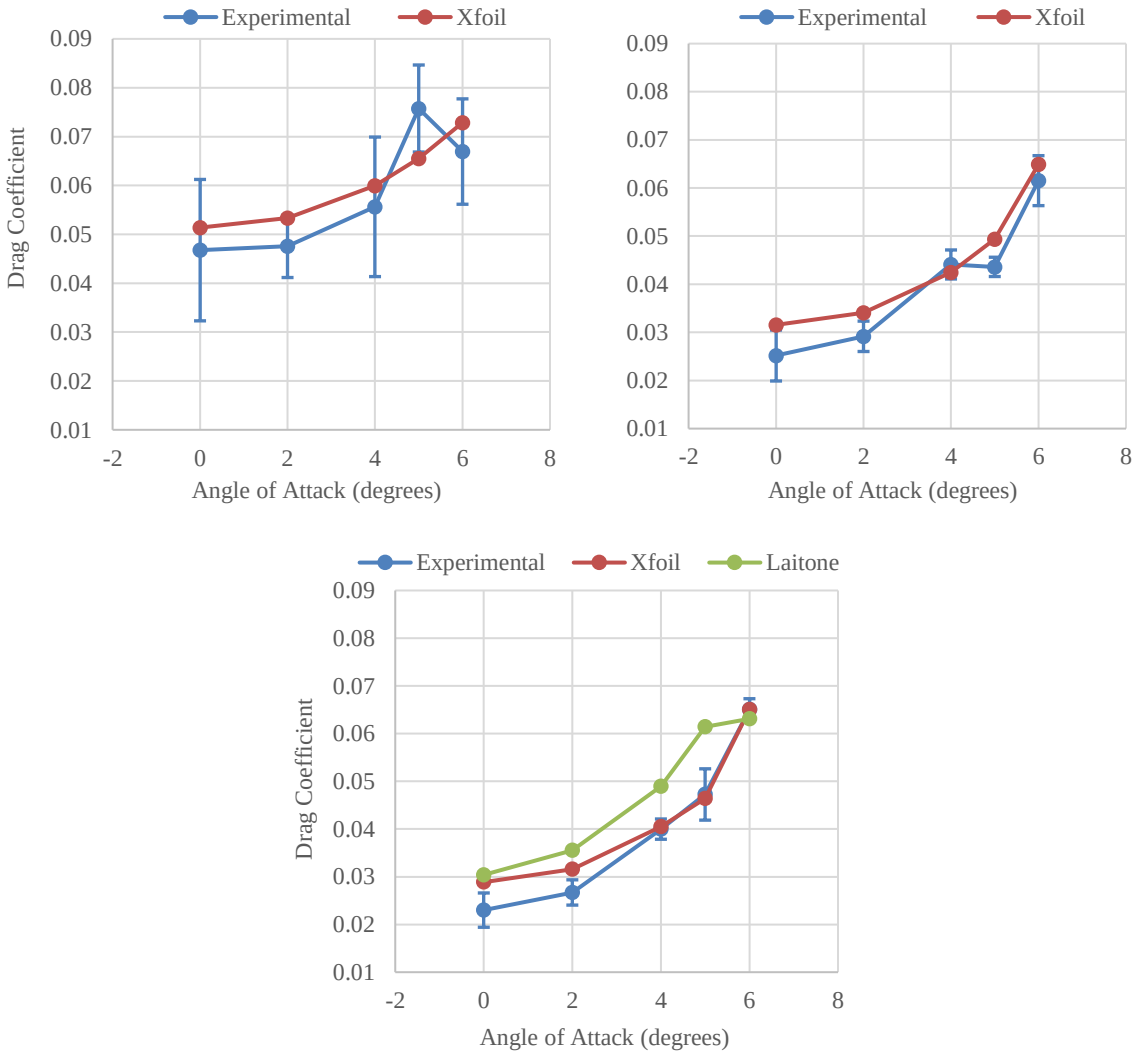

Figure 15: Comparison of experimental and Xfoil clean wing drag coefficients for (top left) Re = 5,600 and (top right) Re = 16,800; comparison of experimental, Xfoil, and Laitone (1996) clean wing for (bottom) Re = 20,700.

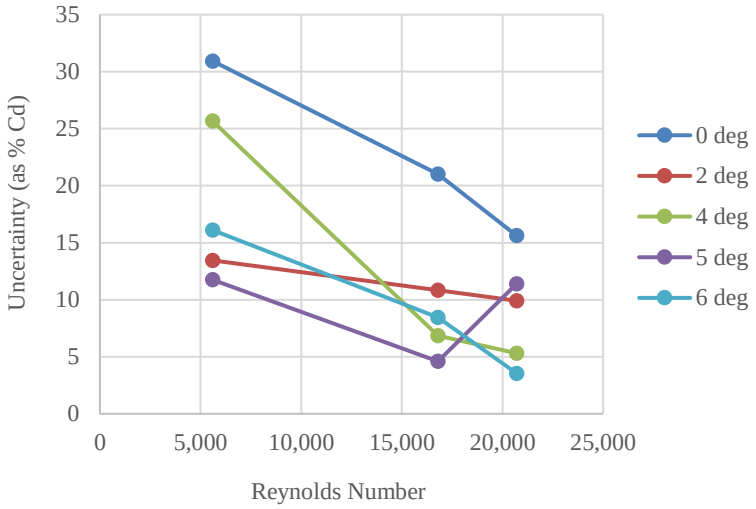

Figure 16: Comparison of uncertainties as percentages of clean wing drag coefficient at angles of attack ranging from 0° to 6°.

To further investigate the high uncertainty at the low Reynolds number cases, individual tests at the 0° angle of attack Re = 5,600 and 0° angle of attack Re = 20,700 cases were analyzed. Specifically, for a single test, the local velocity at the wake's midpoint (approximately) within each image pair was found and plotted against the test's time span. Each test, which ran for 20 seconds at a rate of 10 Hertz, produced 100 local velocity data points. Figure 17 shows the local velocity time-varying results for four tests at α = 0°, Re = 5,600 and Figure 18 shows the results for four tests at α = 0°, Re = 20,700.

These time-dependent graphs produced interesting results. First of all, it can be noted that the data for the Re = 5,600 tests were time-resolved while the data at Re = 20,700 were not. This fact was indicated by the tight, distinct oscillation patterns seen within the Re = 5,600 cases, compared to the scattered, indistinct patterns within the Re = 20,700 cases. Next, the Re = 5,600 data exhibited clear oscillations within each individual test. A potential explanation for these oscillations was that the data were time-resolved enough to capture unsteady vortex shedding within the wake. Experimental work performed by Lee and Huang (1998) tracked unsteady vortex shedding behind a NACA 0012 wing section and compared the flow's Reynolds number to the

shedding's Strouhal number. For a Reynolds number of 672 (calculated using the airfoil thickness, 13.4 mm, instead of chord), Lee and Huang (1998) obtained a thickness-based Strouhal number of approximately 0.1. Fast Fourier Transforms (FFTs) of the data shown in Figure 17 were calculated and are graphed in Figure 19. From these FFTs, the data's oscillation frequency was determined to be approximately 0.2 Hz. Using this frequency, the calculated thickness-based Strouhal number for the data was 0.054. If calculated using the chord, the Strouhal number from the data was approximately 0.45, whereas the Strouhal number from Lee and Huang (1998) corresponding to Re = 5,600 (the chord-based Reynolds number) was approximately 0.55. Using a frequency uncertainty of 0.04 Hz and a freestream velocity uncertainty of 0.002 m/s, the uncertainty for the data's chord-based Strouhal number was calculated to be approximately 0.09 by using the uncertainty propagation method explained in the following section. With this value, the chord-based Strouhal number from Lee and Huang (1998) almost lies within the uncertainty of the

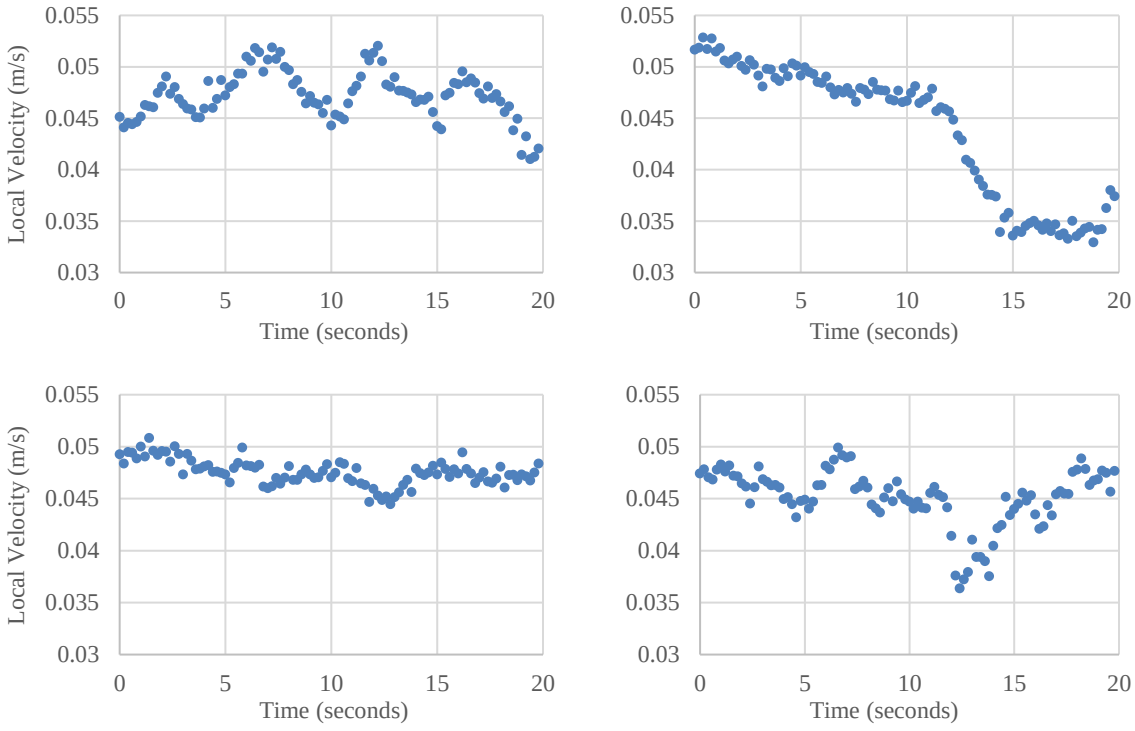

Figure 17: Time-varying local velocities at a point approximately halfway through the wake for four individual tests at Re = 5,600, 0° angle of attack.

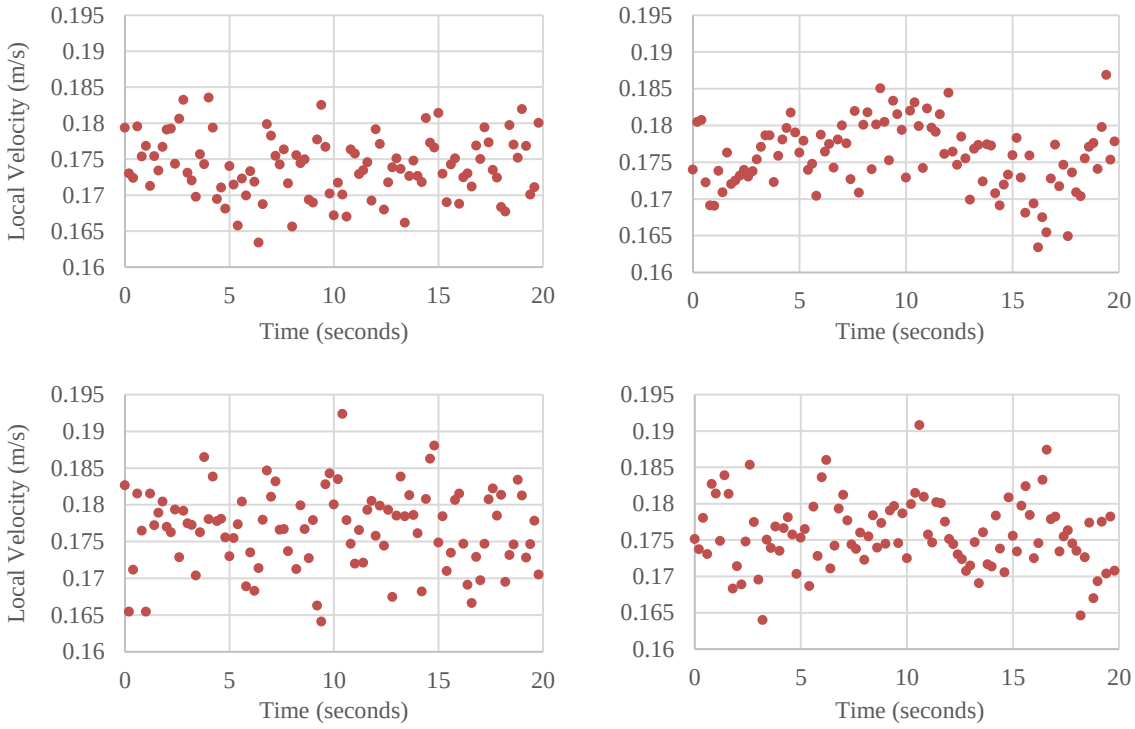

Figure 18: Time-varying local velocities at a point approximately halfway through the wake for four individual tests at Re = 20,700, 0° angle of attack.

experimental data's Strouhal number. The uncertainty for the experimental thickness-based Strouhal number, calculated using the same method, was approximately 0.011. This uncertainty did not include the thickness-based Strouhal number from Lee and Huang (1998). If looking at the chord-based Strouhal numbers, the rough comparisons between the two reasonably indicated that this work's oscillation frequency described an unsteady vortex shedding similar to that seen by Lee and Huang (1998). As further confirmation of this hypothesis, the wake velocity profile as seen in the CFD model for 0° angle of attack, Re = 20,700 case also showed distinct oscillations, potentially indicating unsteady vortex shedding.

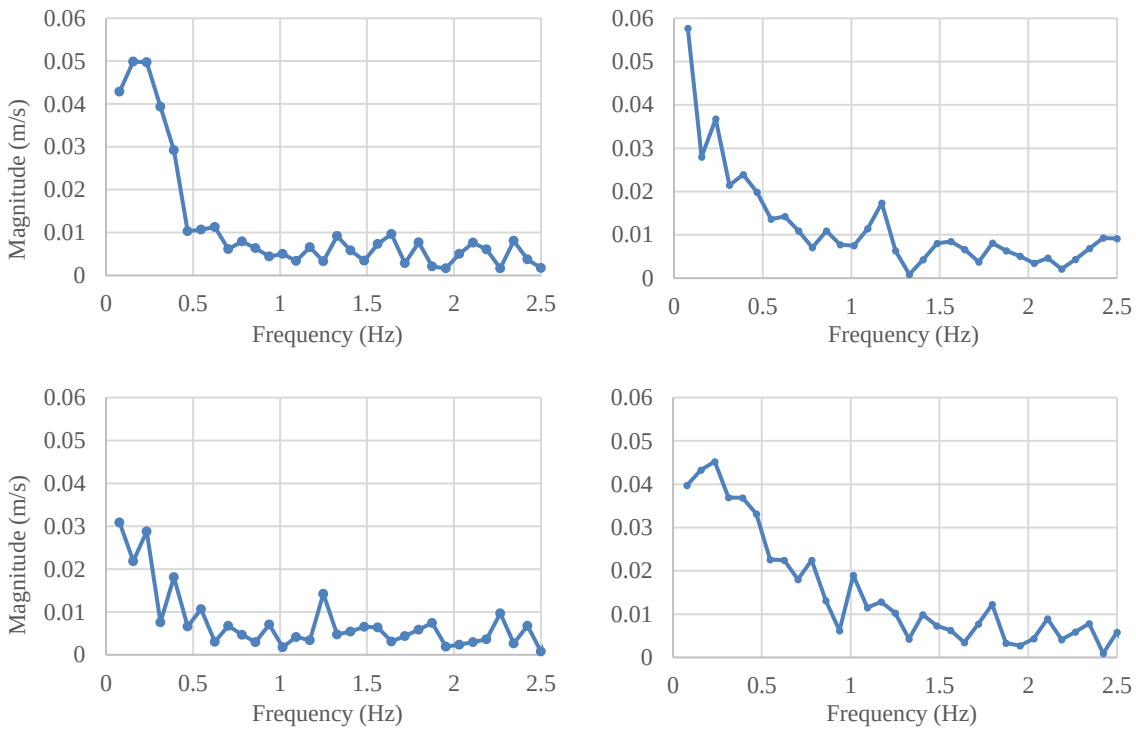

Figure 19: FFT plots of time-varying local velocities lying at a point approximately halfway through the wake for four individual tests (corresponding to those in Figure 17) at Re = 5,600, 0° angle of attack.

In terms of the drag coefficient data discussed previously, the unsteady vortex shedding provided a realistic explanation for the high uncertainties. Since the collected data was time resolved, it clearly depicted the flow's details, but not enough data was taken to obtain a trustworthy statistical average. As the four graphs in Figure 17 demonstrate, the velocity oscillations varied both in amplitude and frequency from test to test within the investigated time window. Analysis done on time-varying drag coefficients showed that it reflected the velocity oscillations. Thus, to obtain an accurate drag coefficient statistical average, longer test periods are needed. At the higher Reynolds number, though, since the data was not time resolved and displayed a more scattered pattern, a statistical average more accurately described the data with relatively low uncertainty.

This hypothesis regarding the α = 0°, Re = 5,600 case's uncertainty also explained the uncertainty of the other angle of attack cases at Re = 5,600: for all Re = 5,600 cases, the data was time-resolved enough to capture unsteady vortex shedding, and not enough data was taken to obtain

an accurate statistical average. Another potential cause of uncertainty at this Reynolds number was that the drag coefficients were reflecting unsteady behavior in the freestream velocity caused by imperfections in the water tunnel. Time-resolved velocities outside of the averaged wake region (and thus presumably freestream velocities) were plotted against time, again from individual tests at Re = 5,600, 0° angle of attack, and showed slight oscillations ranging up to approximately 0.002 m/s above and below the nominal freestream velocity of 0.05 m/s. As shown in Figure 20, the FFTs of these velocity plots indicated that the oscillation frequency was approximately 0.3 Hz, differing from the 0.2 Hz oscillations within the wake. At this low of a Reynolds number, these slight changes in velocity had large impacts on the drag coefficient values, thus adding to their uncertainties in the given time window. At higher Reynolds numbers, potential water tunnel unsteadiness would generate less of an impact on drag coefficients. With unsteady vortex shedding, one would expect to primarily see oscillations within the wake as opposed to the freestream, so these freestream oscillations may have been due to other factors, such as unsteadiness inherent to the water tunnel flow. This hypothesis's credibility was also increased by the fact that the peak oscillations differed between the FFT of the wake velocity and the FFT of the freestream velocity. Alternatively, unsteady vortex shedding extending beyond the wake region may either have been the cause of or contributed to these freestream oscillations, but this proposition does not explain the oscillation frequency differences between the wake and the freestream. An empty water tunnel test would provide further insight: steady flow results would verify that the oscillation was only due to unsteady vortex shedding while unsteady results would suggest that water tunnel characteristics at least affected the freestream.

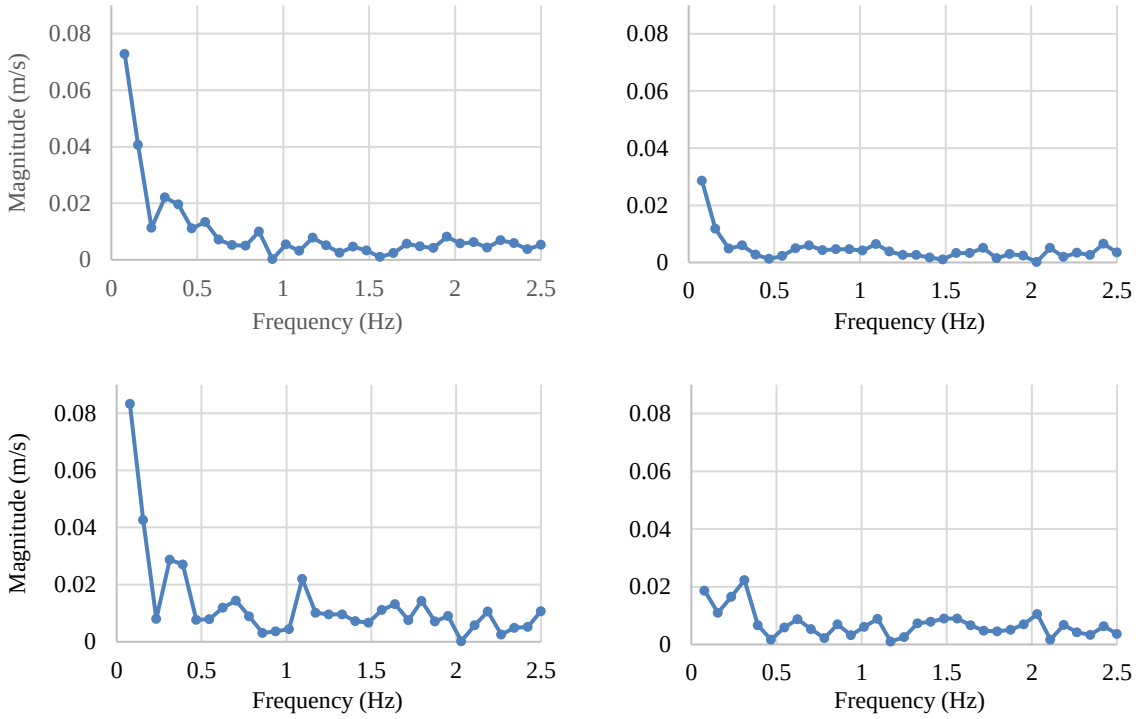

Figure 20: FFT plots of time-varying local velocities lying at a point in the freestream region for four individual tests (corresponding to those in Figure 17) at *Re* = 5,600, 0° angle of attack.

Next, the uncertainties at the low angles of attack (0° and 2°) were considered. These higher uncertainties could possibly have been explained by their small magnitude. From the individual tests at these angles, any variation between drag coefficients, even if small in magnitude, consisted of a high percentage of the average, thus generating higher uncertainty. Using the same rationale, small deviations between drag coefficients would also generate high percent differences, like those between the Xfoil and experimental values. These percent differences between Xfoil's theoretical values and the experimental values were likely highly sensitive to a lack of accuracy in the experiment's angle of attack, a lack of accuracy in freestream velocity, or wing surface defects.

Finally, the true nature of the deviance between the experimental and Laitone (1996) values could not confidently be qualified since Laitone (1996) provided no clear uncertainty analysis. Although Laitone (1996) included details on instrument accuracy, including a beam balance sensitivity of 9.8E-5 Newtons and a micromanometer accuracy of 0.01 mm of water, no further

insights were given. With Xfoil values generally falling between the two sets of experimental data, Laitone (1996) and this work's experimental values were considered reasonable bounds of the clean wing data at Re = 20,700.

4.3.2: Tubercled Wing Results

In the second phase of the experimental work, the tubercled wing drag coefficients were compared to the clean wing drag coefficients. Table 14 lists the clean and tubercled wing drag coefficients along with the percent drag reduction (or increase if a negative number). Figure 21 displays the clean and tubercled wing drag coefficients for all three Reynolds numbers and Figure 22 graphs the percent drag reduction.

The error bars shown in Figure 22 describe the uncertainty associated with the percent drag reduction at each test point. This uncertainty, based on the propagation of the uncertainty (or standard deviation) of the measurements was calculated as follows. The percent drag reduction, p, was calculated using the clean and tubercled drag coefficients, $C_{d,clean}$ and $C_{d,tub}$, in Eq. (4):

$$p = 100\left(1 - \frac{C_{d,tub}}{C_{d,clean}}\right). \quad \textbf{(4)}$$

The drag coefficient ratio's uncertainty, $\sigma_{tub/clean}$, was calculated by propagation the clean and tubercled drag coefficients' uncertainty, σ_{tub} and σ_{clean}, as seen in Eq. (5):

$$\sigma_{tub/clean} = \left|\frac{C_{d,tub}}{C_{d,clean}}\right| \sqrt{\left(\frac{\sigma_{tub}}{C_{d,tub}}\right)^2 + \left(\frac{\sigma_{clean}}{C_{d,clean}}\right)^2}. \quad \textbf{(5)}$$

The percent drag reduction's uncertainty, σ_p, was then calculated by Eq. (6):

$$\sigma_p = 100\left(\sigma_{tub/clean}\right). \quad \textbf{(6)}$$

Table 14: Comparison of experimental clean wing and tubercled wing drag coefficients.

Re	α [deg]	Clean C_d	Tubercled C_d	Percent Reduction
5,600	0	4.68E-02	3.95E-02	15.6
5,600	2	4.76E-02	4.56E-02	4.1
5,600	4	5.56E-02	3.58E-02	35.7
5,600	6	6.69E-02	3.96E-02	40.8
16,800	0	2.52E-02	3.14E-02	-24.7
16,800	2	2.92E-02	3.12E-02	-6.9
16,800	4	4.41E-02	3.79E-02	14.1
16,800	6	6.15E-02	5.59E-02	9.1
20,700	0	2.30E-02	2.34E-02	-1.8
20,700	2	2.67E-02	3.04E-02	-13.9
20,700	4	4.00E-02	3.62E-02	9.6
20,700	6	6.50E-02	5.58E-02	14.2

The data in Figure 22 displays that the tubercled wing decreased the drag coefficients at all angles of attack for Re = 5,600 and for 4° and 6° angle of attack for Re = 16,800 and 20,700. For the Re = 5,600 cases, the percent drag reductions ranged from 4 to 41 percent decreased drag and the drag coefficients themselves did not follow an increasing or decreasing trend with angle of attack. For the Re = 16,800 case, the drag was maximally increased by 25 percent at 0° angle of attack and maximally decreased by 14 percent at 4° angle of attack. For this Reynolds number, the tubercled wing drag coefficients increased with angle of attack, except for the α = 2° case. For the Re = 20,700 case, the drag saw a maximum percent increase of 14 percent at α = 2° and a maximum percent decrease of 14 percent at α = 6°. Also, at this Reynolds number, the tubercled wing drag coefficients increased with increasing angle of attack.

The data's uncertainties, especially as visualized by the error bars in Figure 22, provided key insight into the data's interpretation. These error bars showed that the propagated uncertainties from the clean and tubercled drag coefficients to the percent drag reduction were fairly high. Specifically, the Re = 5,600 uncertainties generally spanned higher than the other Reynolds

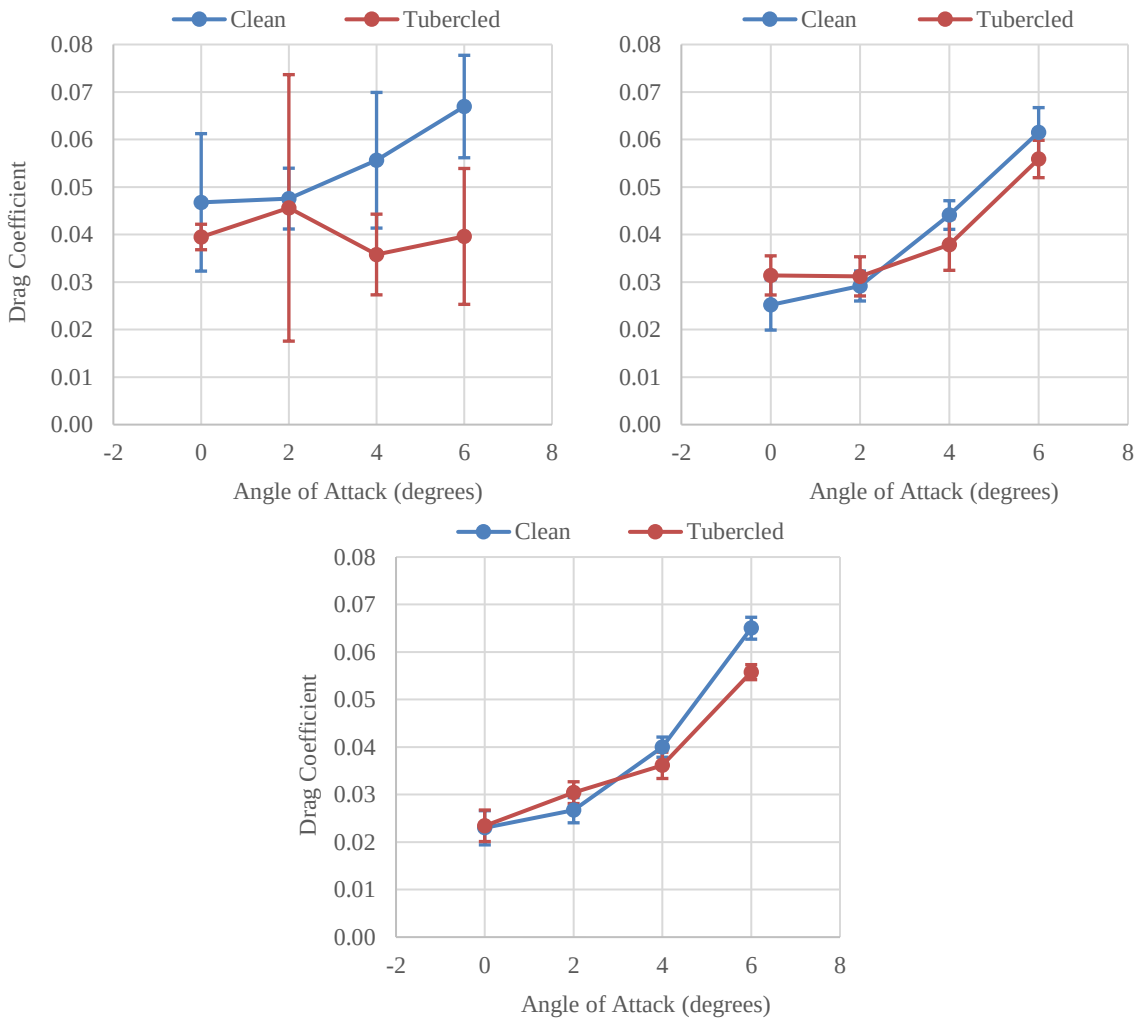

Figure 21: Comparison of clean and tubercled drag coefficient values for (top left) Re = 5,600, (top right) Re = 16,800, and (bottom) Re = 20,700.

numbers' uncertainties, and within each Reynolds number case, the α = 0° and 2° cases exhibited higher uncertainties than the larger angles of attack. The same rationale for the higher uncertainties for these cases with the clean wing applied to these cases with the tubercled wing. For the Re = 5,600 cases, the drag coefficients' high sensitivity to the undulating freestream velocities negated the possibility of acquiring trustworthy average drag coefficients. For the α = 0° and 2° cases, the standard deviation's high sensitivity to small drag coefficient differences greatly increased the uncertainty. One can conclude that higher the Reynolds number and the higher the angle of attack, the more certain the results were. Thus, the results at 4° and 6° angles of attack at Re-16,800 and

Re = 20,700, all showing percent drag reductions of 9 to 15 percent, demonstrated that at these Reynolds numbers and angles of attack, the tubercles did indeed improve the drag characteristics of the wing. It is likely that the tubercles did not improve the drag characteristics at 0° and 2° angle of attack for these two Reynolds numbers, but that conclusion in less certain.

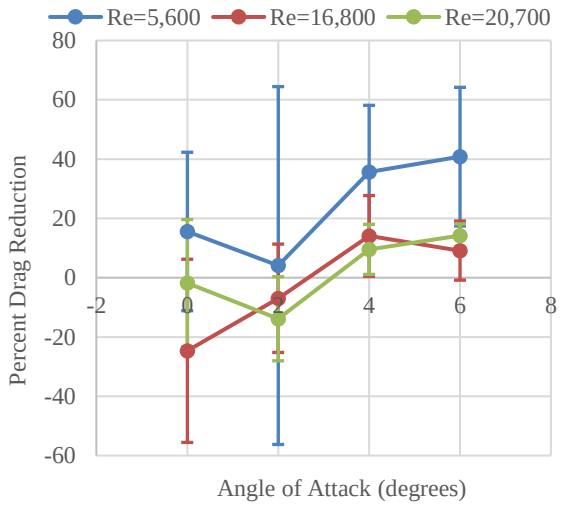

Figure 22: Percent drag reduction versus angle of attack for experimental data at Re = 5,600, Re = 16,800, and Re =20,700.

4.4: Experimental Investigations Summary

The initial clean wing analysis showed that the Re = 5,600 cases generated high uncertainties. Analysis of the 0° angle of attack, time-variant local velocities for the individual tests at this Reynolds number showed that these values were distinctly oscillating within the test window. These results, clearly time-resolved, suggested that either the wing was shedding vortices in an unsteady manner, or inherent unsteadiness in the water tunnel flow affected the freestream, or a combination of the two hypotheses. Rough Strouhal number comparisons to experimental investigation of unsteady vortex shedding off of a NACA 0012 wing section (Lee and Huang, 1998) seemed to validate the vortex shedding theory. Oscillations in the freestream velocities at least validate the possibility that the wake was affected by an unsteady water tunnel characteristic. In

either case, the large drag coefficient uncertainties for this Reynolds number were due to insufficient time samples- frequency and amplitude variance within individual tests and also between individual tests demonstrated that longer time samples were needed to obtain accurate statistical averages. Furthermore, an empty-tunnel test would either confirm or deny the existence of inherent unsteadiness in the water tunnel flow at such a low Reynolds number.

Additionally, clean data at low angles of attack (0° and 2°) produced relatively uncertainties and percent differences with the Xfoil data. These were likely due to the drag coefficients' small magnitude, increasing the weight of differences between individual values and heightening the sensitivity to test conditions such as angle accuracy, freestream velocity accuracy, and wing surface defects.

Taking the clean wing uncertainties into account, the tubercled wing data confirmed that no certain conclusions could be drawn about the tubercles' effects on drag performance for the Re = 5,600 cases and the 0° and 2° angle of attack cases. With more certainty, though, the experiments indicated that the tubercles did indeed decrease the wing's drag at 4° and 6° angle of attack for Reynolds numbers of 16,800 and 20,700.

Another observation to be drawn from these experimental results was that, potentially, the test conditions did not comprise the tubercles' optimal operating environment. For instance, the experimental results indicated the highest drag reduction at the higher angles of attack (4° and 6°) for a given Reynolds number. This trend suggests the possibility that these tubercles most enhance bat flight at even higher angles of attack. Also in these experiments, the tubercle geometry and spacing compared to the wing geometry could have limited drag reduction; perhaps on a bat the performance enhancement is highly dependent on the geometry of the bat's ear and the specific size and placement of the tubercles.

CHAPTER V

REVISED SIMULATION

5.1: Introduction

Three major changes were made from the first CFD models as described in Ch. 3 to the experimental tests as described in Ch. 4. First, the initial CFD tubercled wing model, matched the one used in Martin (2017), had an irregularly-spaced tubercle pattern while the experimental tubercled wing test model had a regularly spaced tubercle pattern. Second, in the experiments, the Re = 20,700 case had been added to the Re = 5,600 and 16,800 cases used in the previous CFD models. Third, the angle of attack range was changed from -5°, 0°, and 5° in the CFD models to 0°, 2°, 4°, and 6° in the experiments. These changes meant that the former CFD drag coefficient values could not be compared to the experimental values, thus necessitating new CFD simulations with updated test models and conditions to be run. This chapter describes the updated CFD models, their resulting drag coefficient values, and the comparison of these values to the experimental data. It also discusses the preliminary CFD investigation of the tubercle-caused flow mechanisms.

5.2: Methods

5.2.1: Test Models

For the second set of CFD simulations, the test models matched exactly those used in the experimental portion of this work. As with both the first set of CFD simulations and the

experiments, the test models consisted of a clean wing and a tubercled wing. Both had a NACA 0012 cross section, a chord of 112 mm and a span of 300 mm. Unlike the test models used for the first set of CFD simulations, though, the tubercles were evenly spaced along the leading edge. A total of fifty tubercles were spaced six millimeters between each apex and each tubercle was inset 0.67 millimeters from the edge. Again, this configuration matched the models used in the experimental part of this work. See Figure 11 and Figure 12 for reference.

The second set of CFD simulations had the same flow field as that used in the first set. The flow field reached 25 chord lengths upstream of the wing, 50 chord lengths downstream of the wing, and 10 chord lengths above and below the wing. The total flow field length was 8.4 meters, its height 2.24 meters, and its width 0.3 meters (the wing's span). See Figure 2 for reference.

5.2.2: Simulation Conditions

Generally, the simulation conditions matched those used in the experimental section of this work, with modeling similar to that used in the first CFD section. Chord-based Reynolds numbers (Eq. (1)) of 5,600, 16,800, and 20,700 were investigated, along with 0°, 2°, 4°, and 6° angles of attack. The models simulated steady, incompressible water flow and used a laminar, three-dimensional, segregated flow solver with cell quality remediation. These solvers were the same as those used in the preliminary CFD models, as mentioned in Ch. 3. Drag was again directly calculated within the simulations, and drag coefficient was calculated using (2).

5.2.3: Mesh Conditions

The mesh conditions applied to the models in this section were derived from the mesh refinement study's resulting mesh as described in Ch. 3. Again, a polyhedral mesh was applied to the flow field and prism layers were applied to the wing surface. The base cell size was 50 millimeters, the total prism layer thickness was 4 millimeters, and the total prism layer was broken into 20 individual layers. The prism layer cells had an average surface size of 3.2 millimeters.

Medium and coarse wake refinements were again placed behind, above, and below the wing, and a single wake refinement was placed in front of the wing. The wake refinement specifications matched those of mesh case three (described in Ch. 3), producing model cell counts ranging from 13.5 to 33.1 million cells. Table 15 provides a complete list of the cell counts.

Table 15: Cell counts from the revised simulations.

Model	Re	U_∞ [m/s]	α [deg]	Cell Count [million]
Clean	5,600	0.05	0	13,943,620
Clean	16,800	0.15	0	13,943,620
Clean	20,700	0.185	0	13,943,620
Clean	5,600	0.05	2	30,751,820
Clean	16,800	0.15	2	30,751,820
Clean	20,700	0.185	2	30,751,820
Clean	5,600	0.05	4	13,461,760
Clean	16,800	0.15	4	13,461,760
Clean	20,700	0.185	4	13,461,760
Clean	5,600	0.05	6	27,911,300
Clean	16,800	0.15	6	27,911,300
Clean	20,700	0.185	6	27,911,300
Tubercled	5,600	0.05	0	30,447,140
Tubercled	16,800	0.15	0	30,447,140
Tubercled	20,700	0.185	0	30,447,140
Tubercled	5,600	0.05	2	32,965,660
Tubercled	16,800	0.15	2	32,965,660
Tubercled	20,700	0.185	2	32,965,660
Tubercled	5,600	0.05	4	28,894,280
Tubercled	16,800	0.15	4	28,894,280
Tubercled	20,700	0.185	4	28,894,280
Tubercled	5,600	0.05	6	33,088,140
Tubercled	16,800	0.15	6	33,088,140
Tubercled	20,700	0.185	6	33,088,140

5.2.4: Test Matrix

The test matrix for this section closely followed the Phase 2 test matrix from the experimental section. For both the clean and tubercled wings, each Reynolds number (5,600,

16,800, and 20,700) was run at each of the four angles of attack (0°, 2°, 4°, and 6°). Each simulation was run for 2,000 iterations. The test matrix is shown in Table 16.

Table 16: Revised CFD simulations test matrix. Simulation run times ranged from approximately 6 hours to 8+ hours.

Model	Re	U_∞ [m/s]	α [deg]	Iterations
Clean	5,600	0.05	0	2,000
Clean	16,800	0.15	0	2,000
Clean	20,700	0.185	0	2,000
Clean	5,600	0.05	2	2,000
Clean	16,800	0.15	2	2,000
Clean	20,700	0.185	2	2,000
Clean	5,600	0.05	4	2,000
Clean	16,800	0.15	4	2,000
Clean	20,700	0.185	4	2,000
Clean	5,600	0.05	6	2,000
Clean	16,800	0.15	6	2,000
Clean	20,700	0.185	6	2,000
Tubercled	5,600	0.05	0	2,000
Tubercled	16,800	0.15	0	2,000
Tubercled	20,700	0.185	0	2,000
Tubercled	5,600	0.05	2	2,000
Tubercled	16,800	0.15	2	2,000
Tubercled	20,700	0.185	2	2,000
Tubercled	5,600	0.05	4	2,000
Tubercled	16,800	0.15	4	2,000
Tubercled	20,700	0.185	4	2,000
Tubercled	5,600	0.05	6	2,000
Tubercled	16,800	0.15	6	2,000
Tubercled	20,700	0.185	6	2,000

5.3: Results

5.3.1: Clean and Tubercled Wing CFD Results

After each clean and tubercled simulation was run, the resulting drag coefficients were compared and the drag reduction (or increase) due to the tubercles was calculated. The drag

coefficient results are tabulated in Table 17 and are graphed in Figure 23. Figure 24 shows the percent drag reduction or increase.

Table 17: Comparison of CFD clean and tubercled drag coefficients.

Re	α [deg]	Clean Wing C_d	Tubercled Wing C_d	Percent Reduction
5,600	0	4.74E-02	4.71E-02	0.46
5,600	2	4.85E-02	4.83E-02	0.24
5,600	4	5.28E-02	5.24E-02	0.69
5,600	6	6.18E-02	6.22E-02	-0.68
16,800	0	2.93E-02	2.85E-02	2.75
16,800	2	3.11E-02	3.07E-02	1.37
16,800	4	4.13E-02	4.12E-02	0.30
16,800	6	5.65E-02	5.75E-02	-1.80
20,700	0	2.75E-02	2.64E-02	4.25
20,700	2	2.90E-02	2.89E-02	0.32
20,700	4	4.09E-02	4.01E-02	1.95
20,700	6	5.23E-02	4.11E-02	21.3

As shown (Table 17, Figure 23, and Figure 24), generally, the tubercled wing drag coefficients followed the clean wing drag coefficient trends of increasing drag coefficients with increasing angle of attack. In all cases except for α = 6° at Re = 5,600 and 16,800, the tubercles decreased the drag. Also, generally, the tubercles did not significantly affect the drag values; all percent increases and decreases were within 5 percent, except for the Re = 20,700, α = 6° case. For the Re = 5,600 cases, the percent drag reduction reached no higher than 0.69 percent (at 4° angle of attack) and the percent increase no higher than 0.68 percent (at 6° angle of attack). For the Re = 16,800 cases, the drag was maximally reduced by 2.75 percent at α = 0° and maximally increased by 1.8 percent at α = 6°. Finally, for the Re = 20,700 cases, the drag was maximally reduced by 21.3 percent at α = 6°.

Interestingly, for all three Reynolds numbers at 0° angle of attack, the irregularly spaced tubercles (as discussed in Ch. 3) increased the drag as compared to the corresponding clean wing

values. Conversely, the evenly spaced tubercles, as described in the current chapter, decreased drag for the same conditions. This switch to drag reduction could be attributed to the introduction of more tubercles (50 tubercles in the current models compared to 32 tubercles in the former models). The change could also be caused by a difference in the flow structures attributable to regular spacing as opposed to irregular spacing. The causation requires investigation into the tubercles' three-dimensional effects, though, and thus is not covered in this work.

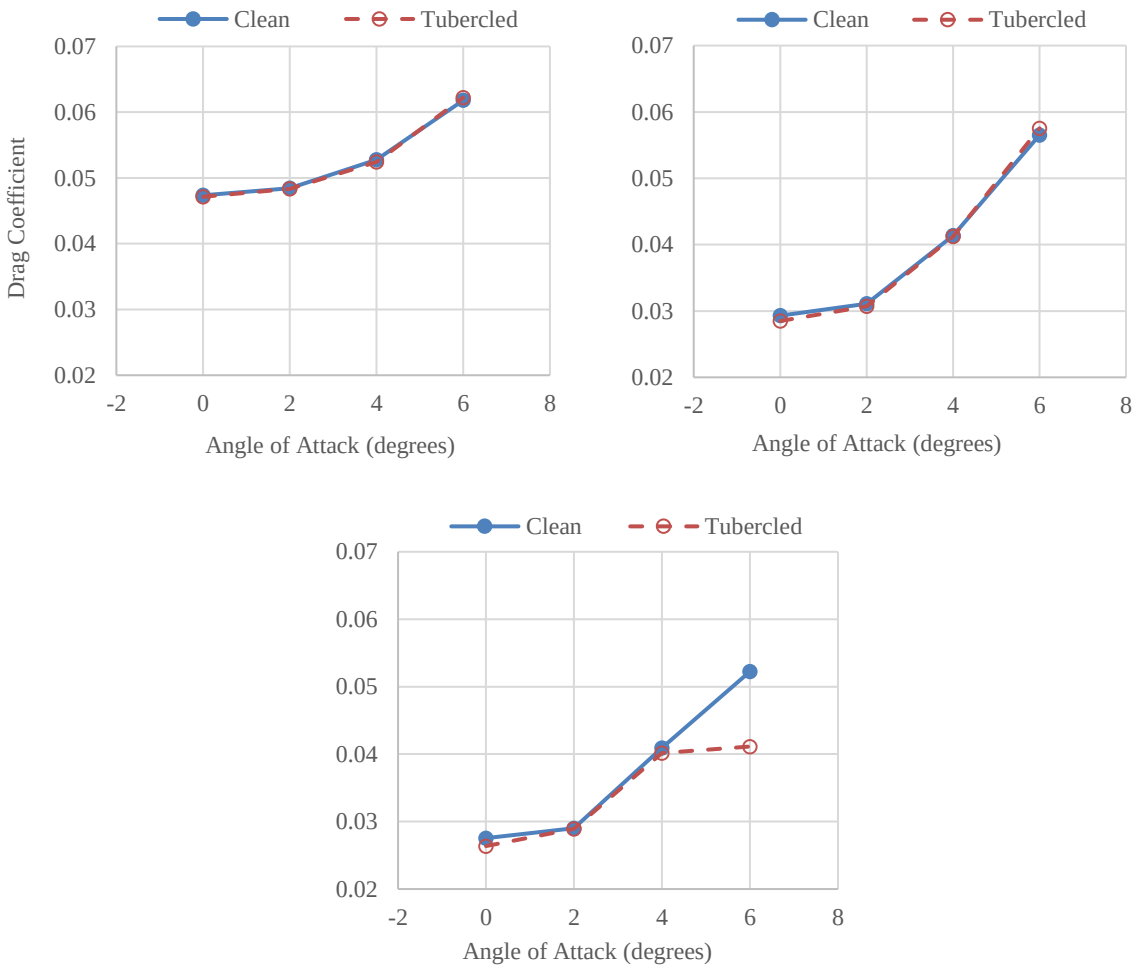

Figure 23: Comparison of CFD clean and tubercled drag coefficient values for (top left) *Re* = 5,600, (top right) *Re* = 16,800, and (bottom) *Re* = 20,700.

Overall, the CFD results indicated that the lower the Reynolds number, the less impact the tubercles have on the drag. For the Re = 5,600 cases, the tubercles improved the drag by a maximum of 0.7 percent; for the Re = 16,800 cases, the tubercles improved the drag by a maximum of 2.75 percent, and for the Re = 20,700 cases, excepting the α = 6° case, the tubercles improved the drag by a maximum of 4.25 percent. The Re = 20,700, α = 6° case saw a drag reduction of 21.3 percent. Finally, the CFD results did not indicate any distinct trends in drag reduction with angle of attack.

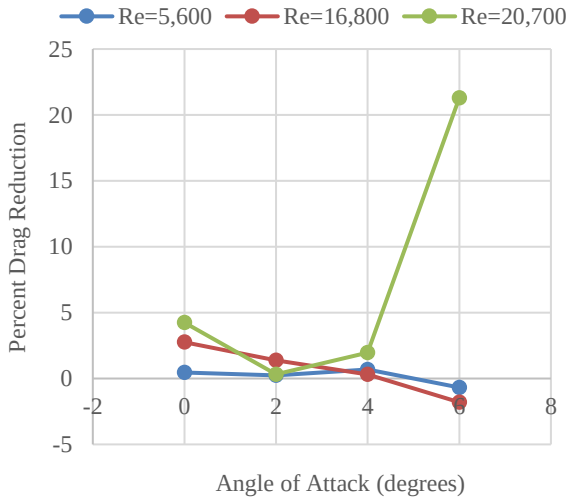

Figure 24: Percent drag reduction versus angle of attack for CFD data at Re = 5,600, Re = 16,800, and Re = 20,700.

In addition to calculating clean and tubercled wing drag data, the simulations also were set to calculate lift data. The lift force was found by taking the pressure component of the force on the wing section in the positive y-direction. Using the lift force L, the density of water ρ (997 kg/m^3), the freestream velocity U_∞, and the planform projected surface area S (0.0336 m^2), Eq. (7) was used to calculate the lift coefficient C_l:

$$C_l = \frac{L}{0.5\rho {U_\infty}^2 S}. \quad \textbf{(7)}$$

The lift coefficient results, along with percent increase from the clean to the tubercled cases, are shown in Table 18 and Figure 25.

These lift results were not analyzed to any extent; they are only included to demonstrate the preliminary CFD results. More investigation should be done especially on the α = 2° cases where the lift coefficients are negative.

Table 18: Comparison of CFD clean and tubercled wing lift coefficients.

Re	α [deg]	Clean Wing C_l	Tubercled Wing C_l	Percent Increase
5,600	0	4.35E-04	-2.57E-04	-159.15
5,600	2	6.69E-02	6.80E-02	1.65
5,600	4	1.15E-01	1.08E-01	-6.18
5,600	6	1.53E-01	1.58E-01	3.89
16,800	0	2.66E-04	-3.19E-04	-219.81
16,800	2	2.65E-03	-1.91E-03	-172.17
16,800	4	1.57E-01	1.38E-01	-12.44
16,800	6	4.79E-01	5.43E-01	13.23
20,700	0	1.62E-03	1.11E-04	-93.14
20,700	2	-4.90E-03	-4.05E-03	-17.24
20,700	4	2.29E-01	2.74E-01	19.46
20,700	6	5.90E-01	5.98E-01	1.42

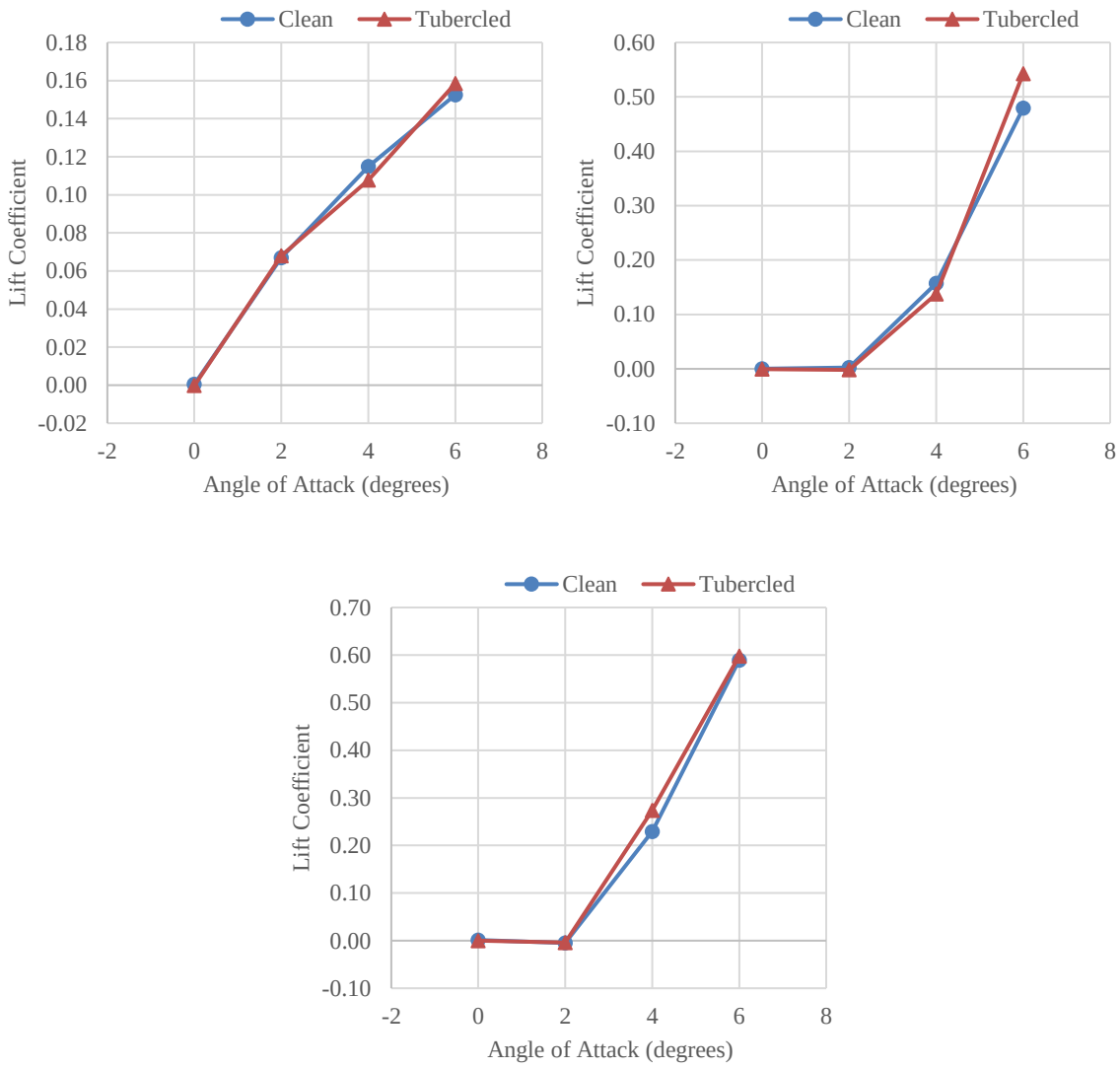

Figure 25: Comparison of CFD clean and tubercled wing lift coefficients for (top left) Re = 5,600, (top right) Re = 16,800, and (bottom) Re = 20,700.

5.3.2: Comparison of CFD Results to Experimental Results

The CFD clean and tubercled results were then compared to the experimental clean and tubercled results. Table 19 summarizes the comparison between experimental and CFD clean wing drag coefficients; Figure 26 graphs this comparison and includes Xfoil and Laitone (1996) data. Table 20 and Figure 27 exhibit the comparison of CFD and experimental tubercled wing data. Finally, Table 21 and Figure 28 display the comparison of CFD and experimental drag reduction results with percent drag reduction.

As is evident in Table 19 and Figure 26, the CFD clean wing drag coefficients are within 10 percent of the experimental values for all cases except 0° angle of attack at Re = 16,800 and 20,700 and 6° angle of attack at Re = 16,800. For Re = 5,600 and 16,800, all CFD drag coefficients lie within or at the very edge of the experimental error bars. At Re = 20,700, the 2° and 4° angles of attack values lie within the experimental error bars; the 0° and 6° angle of attack cases do not. The CFD values follow the experimental values' trend of increasing with increasing angle of attack.

Table 19: Comparison of CFD and experimental clean wing drag coefficients.

Re	α [deg]	Clean CFD C_d	Clean Experimental C_d	Percent Difference
5,600	0	4.74E-02	4.68E-02	1.25
5,600	2	4.85E-02	4.76E-02	1.87
5,600	4	5.28E-02	5.56E-02	5.28
5,600	6	6.18E-02	6.69E-02	8.00
16,800	0	2.93E-02	2.52E-02	15.1
16,800	2	3.11E-02	2.92E-02	6.42
16,800	4	4.13E-02	4.41E-02	6.46
16,800	6	5.65E-02	6.15E-02	8.48
20,700	0	2.75E-02	2.30E-02	17.9
20,700	2	2.90E-02	2.67E-02	8.28
20,700	4	4.09E-02	4.00E-02	2.37
20,700	6	5.23E-02	6.50E-02	21.8

Since the CFD drag coefficient values lay within or at the edge of the experimental values' error bars for Re = 5,600 and 16,800, the CFD clean wing simulations at these Reynolds numbers were within the uncertainty of the experimental values and thus satisfactorily matched the experiments. Also, all percent differences between the experimental and CFD values for these two Reynolds numbers were less than 10 percent, excepting the α = 0°, Re = 16,800 case. These generally small differences also pointed to accurate modeling of the experiments in CFD. The outlier CFD value lay between the experimental and Xfoil values for that test case. Since the low

Reynolds number, low angle of attack experimental values had high uncertainty, this outlier CFD value might possibly be more accurate that the experimental value.

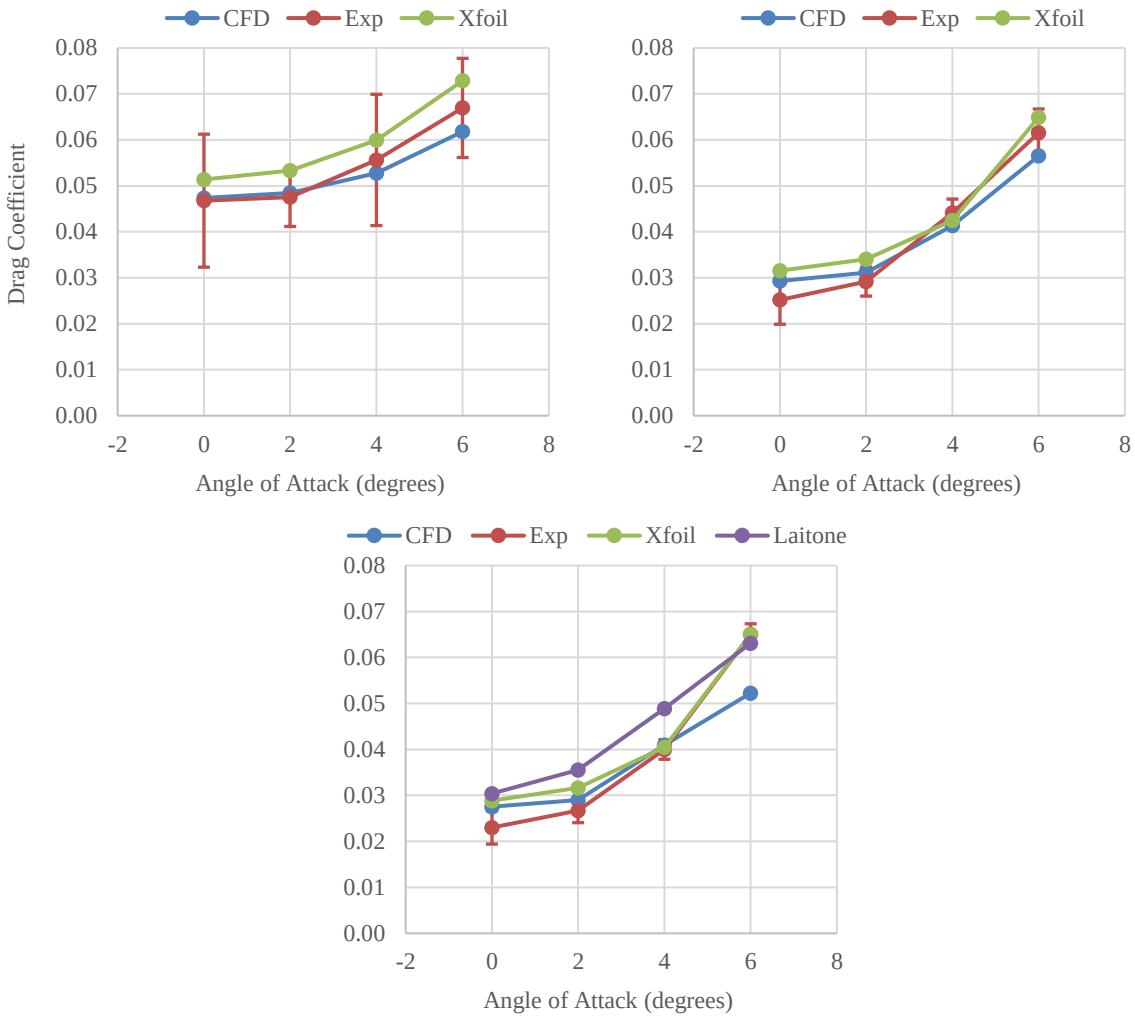

Figure 26: Comparison of CFD, experimental, and Xfoil clean wing drag coefficients for (top left) Re = 5,600 and (top right) Re = 16,800; comparison of CFD, experimental, Xfoil, and Laitone (1996) clean wing for (bottom) Re = 20,700.

For the Re = 20,700 test points, excepting the α = 6° case, the CFD drag coefficients lay between this work's experimental values and the Laitone (1996) experimental values. Additionally, these CFD values were within 10 percent of the Xfoil values. Thus, if the experimental and Laitone (1996) values are assumed to span a reasonable drag coefficient range, the CFD models for the α = 0° to 4° cases likely accurately portrayed the flow in these scenarios. At α = 6°, the CFD model

deviated somewhat significantly from the experimental, Xfoil, and Laitone (1996) values. Since all three of these values seemed to converge, the CFD model must be further investigated and likely refined to produce a drag coefficient matching the others.

Table 20 and Figure 27 highlight that, in general, the CFD tubercled wing drag coefficients deviate more strongly from the experimental values than the clean wing values. The highest percent differences lie within the Re = 5,600 cases (38 and 44 percent differences at α = 4° and 6°, respectively) and at the α = 6°, Re = 20,700 case. The CFD tubercled drag coefficients lie within the experimental error bars at the 2°, Re = 5,600 case, at all Re = 16,800 cases, and at the α = 0° and 2°, Re = 20,700 cases. The smaller two Reynolds numbers exhibit an increasing trend with increasing angle of attack, but the Re = 20,700 case breaks the trend with a relatively small increase in drag coefficient between the α = 4° and 6° angles of attack.

Table 20: Comparison of CFD and experimental tubercled wing drag coefficients.

Re	α [deg]	Tubercled CFD C_d	Tubercled Experimental C_d	Percent Difference
5,600	0	4.71E-02	3.95E-02	17.7
5,600	2	4.83E-02	4.56E-02	5.81
5,600	4	5.24E-02	3.58E-02	37.7
5,600	6	6.22E-02	3.96E-02	44.4
16,800	0	2.85E-02	3.14E-02	9.71
16,800	2	3.07E-02	3.12E-02	1.68
16,800	4	4.12E-02	3.79E-02	8.42
16,800	6	5.75E-02	5.59E-02	2.88
20,700	0	2.64E-02	2.34E-02	11.8
20,700	2	2.89E-02	3.04E-02	5.01
20,700	4	4.01E-02	3.62E-02	10.4
20,700	6	4.11E-02	5.58E-02	30.2

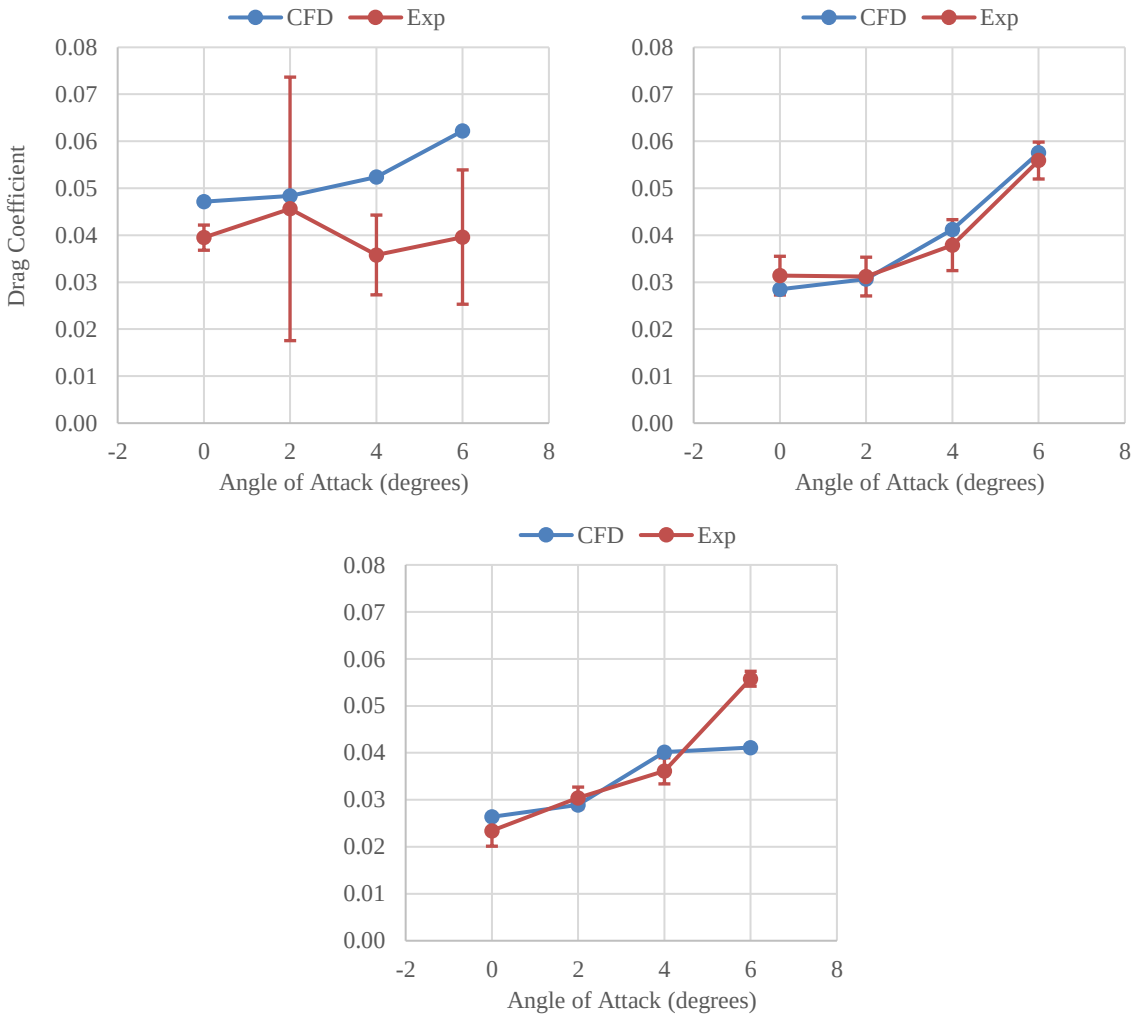

Figure 27: Comparison of CFD and experimental tubercled wing drag coefficients for (top left) Re = 5,600, (top right) Re = 16,800, and (bottom) Re = 20,700.

Table 20 and Figure 28 demonstrate that generally, the tubercles affected the CFD simulated drag significantly less than they did the experimentally measured drag. For the Re = 5,600 cases, the tubercles affected the CFD drag values by less than 1 percent for every angle of attack while in the experiments the tubercles reduced the drag anywhere from 4 percent to 44 percent. For the Re = 16,800 cases, the maximum CFD percent drag reduction was 2.75 percent, while the maximum experimental percent drag reduction was 14.1 percent. For the Re = 20,700 cases, though, at 6° angle of attack, the CFD model predicted a 21 percent drag reduction while the experimental α = 6° tests indicated a 14 percent drag reduction. For the lower two Reynolds

numbers, the CFD trends in percent drag reduction with increasing angle of attack did not match the experimental trends, but for the Re = 20,700 cases, the CFD trend did match the experimental trend. The percent reduction decreased from α = 0° to 2° and then increased from α = 2° to 4° and from α = 4° to 6°.

The differences between the CFD and experimental percent drag reductions were due to one of three possibilities: either the experimental values overpredicted the drag reduction, the CFD simulations underpredicted the reduction, or the differences were due to both experimental overprediction and CFD underprediction. In Ch. 4, the average drag coefficients at each angle of attack in the Re = 5,600 case were shown to be highly uncertain due to freestream oscillations. Drag coefficients at 0° and 2° angle of attack were considered relatively uncertain due to high sensitivity to small changes in freestream velocity, angle of attack accuracy, etc. With greater uncertainty, the experimental values at Re = 5,600 and 0° and 2° angles of attack certainly could have overpredicted the drag reduction.

Table 21: Comparison of CFD and experimental percent drag reduction.

Re	α [deg]	CFD Percent Reduction	Experimental Percent Reduction
5,600	0	0.462	15.6
5,600	2	0.243	4.11
5,600	4	0.685	35.7
5,600	6	-0.679	40.8
16,800	0	2.75	-24.7
16,800	2	1.37	-6.94
16,800	4	0.303	14.1
16,800	6	-1.80	9.14
20,700	0	4.25	-1.83
20,700	2	0.322	-13.9
20,700	4	1.95	9.56
20,700	6	21.3	14.2

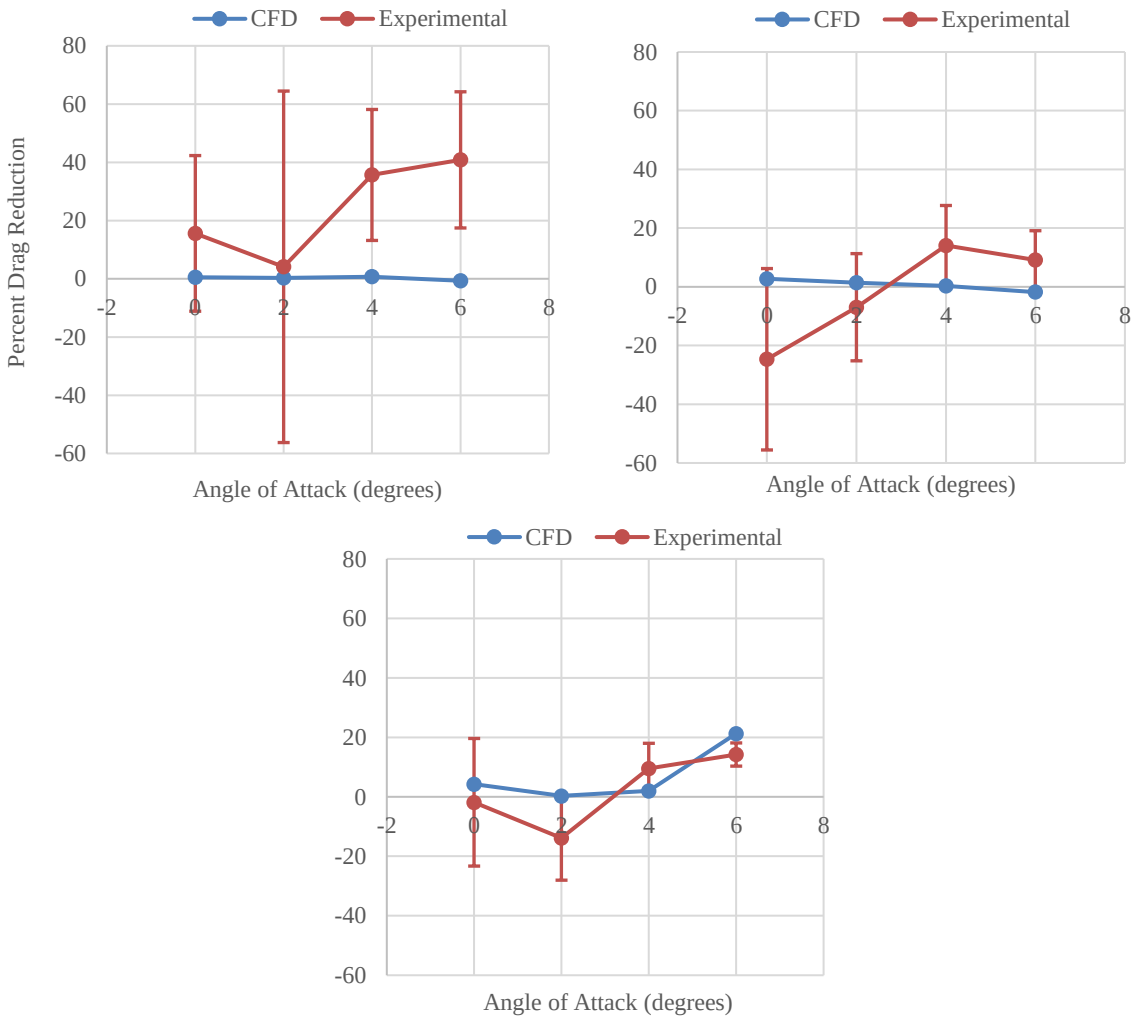

Figure 28: Comparison of percent drag reduction for both CFD and experimental results for (top left) Re = 5,600, (top right) Re = 16,800, and (bottom) Re = 20,700.

It was also possible that the CFD underpredicted the drag reduction. For most of the clean wing cases, the percent differences between the CFD and experimental drag coefficients were less than 10 percent, indicating that the clean wing simulations fairly accurately modeled the flow. That indicated that the differences in experimental and CFD drag reduction lay with the tubercled cases as opposed to the clean. At Re = 5,600, the CFD tubercled drag coefficients at 4° and 6° angle of attack did not lie within the experimental values' error bars. Thus, even though the experimental values contained large uncertainty, the CFD values potentially were not capturing a drag-reducing flow structure at this Reynolds number. Also, at the Re = 16,800, 4° and 6° angle of attack cases,

the CFD tubercled wing drag coefficients lay at the edge of the experimental values' error bars. These experimental values contained less uncertainty than the Re = 5,600 cases or Re = 16,800, 0° and 2° angles of attack cases, so again the CFD models might not have been capturing enough flow information.

Especially at the lower Reynolds numbers, the mesh generated around the tubercles was possibly not resolved enough to capture the drag-reducing flow structures. This hypothesis was supported by the fact that, at Re = 20,700, the CFD drag reduction trend with increasing angle of attack matched the trend displayed in the experimental data. Since the clean CFD data generally followed the clean experimental drag coefficient trend with increasing angle of attack, the CFD tubercled wing data must also have generally followed the experimental tubercled trend to produce the same drag reduction trend. This indicated that the CFD tubercled wing simulations must have modeled somewhat accurate flow structures over the tubercles, even if their magnitude was not the same as those experienced by the tubercles in the experiments. Further resolving the tubercle mesh would likely correct the drag reduction magnitude differences for the Re = 20,700 cases. At lower Reynolds numbers and lower angles of attack, these flow structures were possibly smaller than the Re = 20,700 cases and thus the meshes surrounding the tubercles were not resolved enough to capture them.

Without more certain experimental data for the low Reynolds, low angle of attack cases, though, the CFD drag reduction could not be ruled inaccurate. Perhaps the tubercles affected the drag very little in these cases and only began to generate substantial flow structures at higher angles of attack and higher Reynolds numbers. Further resolving the mesh around the tubercles at Re = 5,600 cases and at the 0° and 2° angles of attack cases would provide insight into this hypothesis's legitimacy.

5.3.3: Drag Reduction Flow Mechanism Investigation

To investigate what flow mechanisms were causing the drag reduction seen in the Re = 20,700 cases, the vorticity magnitudes and the velocity magnitude profiles surrounding each clean and tubercled wing were examined. The maximum vorticity magnitudes achieved in each of the clean and tubercled simulations at every angle of attack, along with the percent increases, are displayed in Table 22. The velocity profiles for each angle of attack are shown in Figure 30.

Table 22: Maximum vorticity magnitude comparison for the CFD Re = 20,700 clean and tubercled wing models.

α [deg]	Clean Wing Maximum Vorticity [/s]	Tubercled Wing Maximum Vorticity [/s]	Vorticity Percent Increase
0	1,190	1,370	15.2
2	1,360	1,770	30.3
4	1,760	2,850	62.0
6	2,410	5,770	139

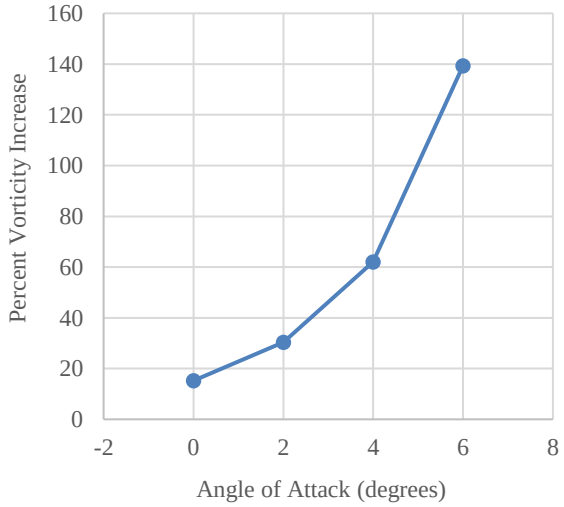

Figure 29: Percent vorticity increase between the clean and tubercled CFD models varied with angle of attack for the Re = 20,700 CFD cases.

In each of the models, the maximum vorticity was seen within the wing's leading edge boundary layer. Vorticity magnitude was chosen as an appropriate parameter to use in the drag reduction investigation because a boundary layer with higher vorticity levels would tend to stay attached to the wing longer than one with lower vorticity levels. This delay in stall, due to the higher vorticity, would correspond to drag reduction. As Table 22 shows, the maximum vorticity values all increased from the clean to the tubercled models. The percent increases increased with angle of attack. This trend in percent vorticity increase did not align with the percent drag reduction trend,

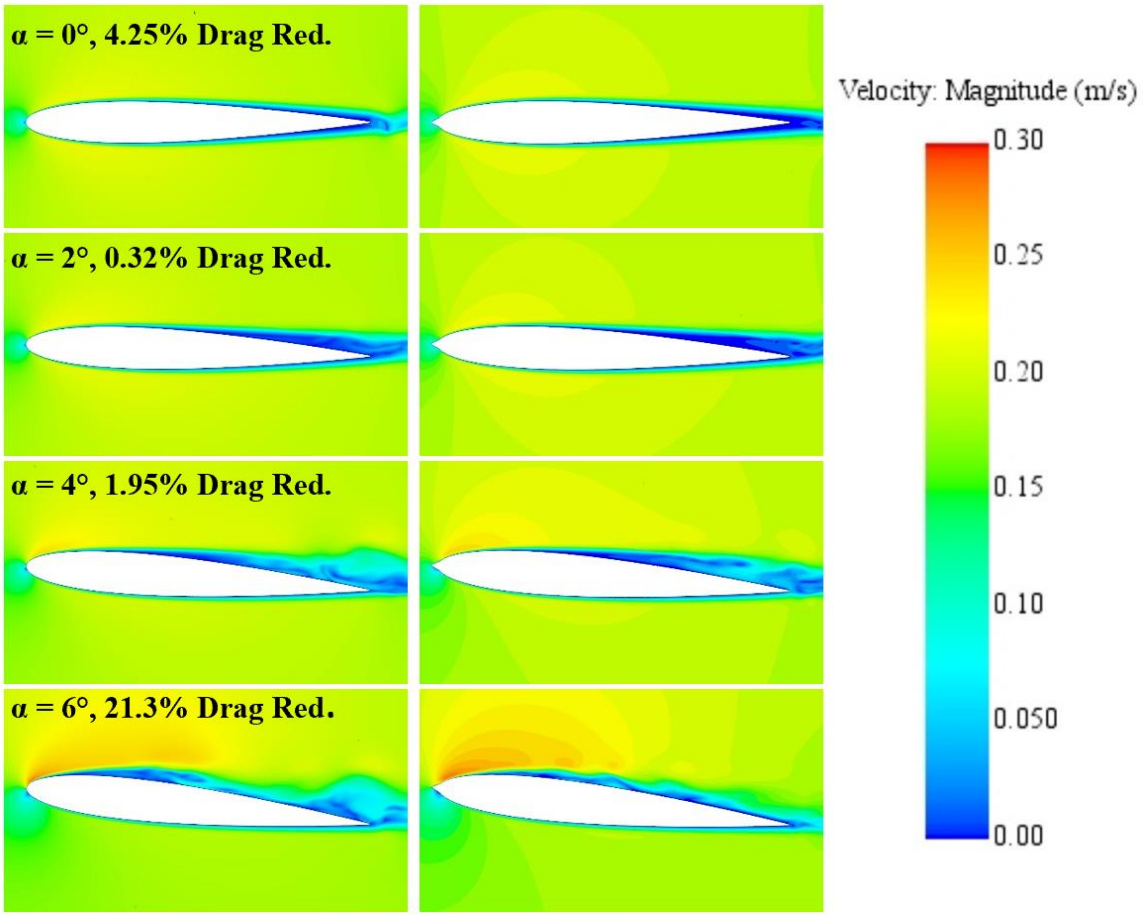

Figure 30: CFD visualization of (left) clean wing and (right) tubercled wing velocity magnitude fields for 0°, 2°, 4°, and 6° angles of attack. These views show a plane through z = 150 mm (halfway through the flow domain) for the clean wing and 153 mm (through the center of a tubercle) for the tubercled wing.

as would be expected. To further investigate the flow's behavior, the velocity profiles were examined next.

From the previous section, the CFD tubercled wing models all generated less drag than the corresponding clean wing models. The 0° and 6° angles of attack models produced the largest drag percent reductions of 4.25 and 21.3 percent, respectively. Looking at the velocity profiles as seen in Figure 30, one would expect to see significant separation delay from the clean to the tubercled models at the angles with high drag reduction. This separation delay was clearly evident between the $\alpha = 6°$ clean and tubercled models, but none of the other tubercled models appeared to delay the flow separation. Since the flow separation on top of each wing did not provide clear insights into the drag reduction mechanism, the velocity profiles as seen in the wing wakes were then examined. The wakes are shown in Figure 31.

As a further note, Martin (2017) witnessed clean wing stall at approximately 11° angle of attack at Re = 5,600. In these simulations, the clean wing showed separation at $\alpha = 6°$ for a Reynolds number of 20,700. This CFD result corroborated a drop in lift coefficient (presumably due to separation) at $\alpha = 6°$ for Re = 20,700 as described in Laitone (1996). Also, the CFD velocity profiles for both the clean and tubercled wings at Re = 5,600, $\alpha = 6°$ showed flow separation. With the CFD models showing negligible impact of the tubercles on drag reduction for the Re = 5,600 cases, it was not surprising that the CFD tubercled wing model did not show much change in flow separation from the clean case, either. What these Re = 5,600, $\alpha = 6°$ CFD models plus the agreement between Laitone (1996) and the clean wing CFD model at Re = 20,700, $\alpha = 6°$ demonstrated, though, was that flow over a NACA 0012 airfoil is likely stalled at $\alpha = 6°$, even at Re = 5,600, and that Martin could have used a 6° angle of attack to experimentally investigate the tubercles' effect on flow separation.

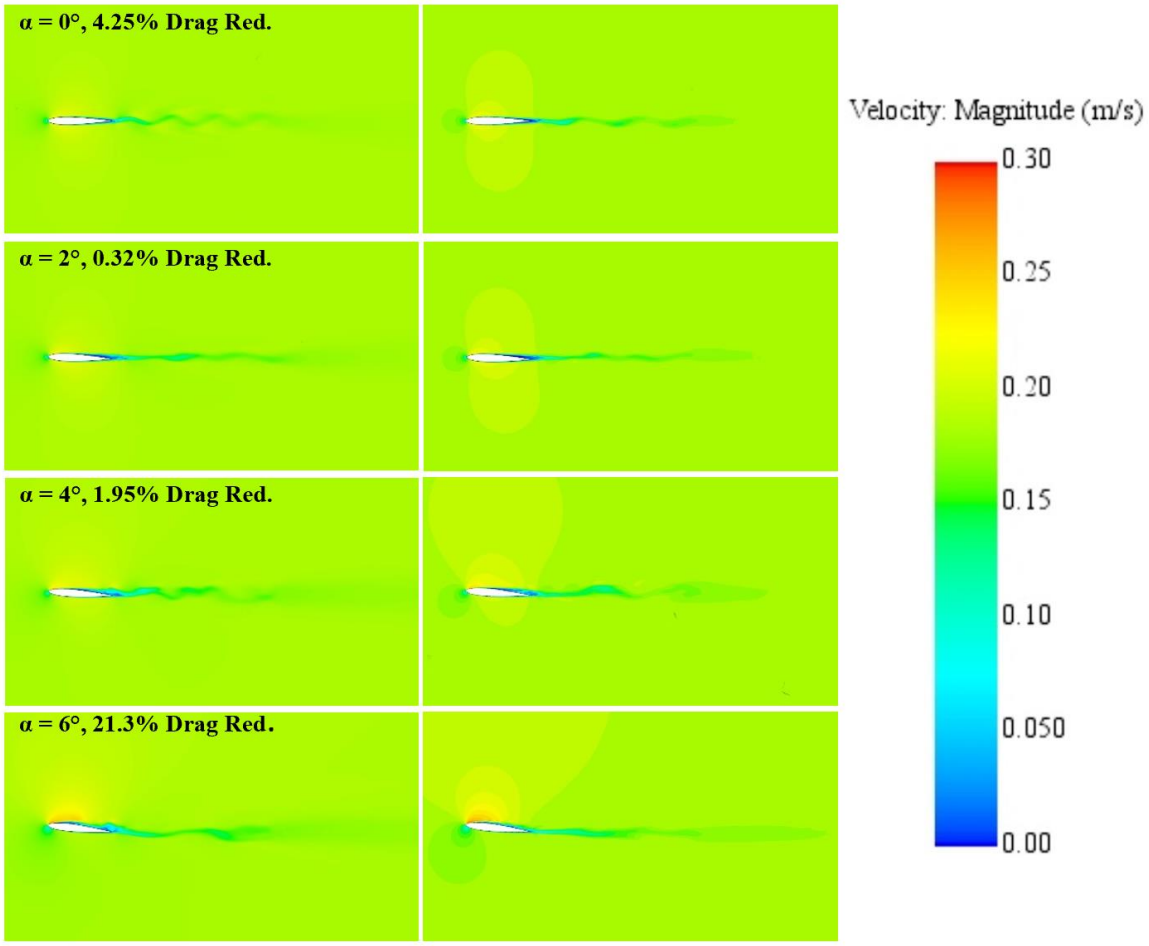

Figure 31: CFD visualization of (top) clean wing vorticity and (bottom) tubercled wing vorticity coming off of the leading edge. These views show a plane through z = 150 mm (halfway through the flow domain) for the clean wing and 153 mm (through the center of a tubercle) for the tubercled wing.

Figure 31 provided a clear visualization of the drag reduction. In general, these wakes showed varying degrees of oscillation, perhaps indicating unsteady vortex shedding. These oscillations matched what the experimental data at Re = 5,600 showed, suggesting that even the highest Reynolds number cases were possibly experiencing unsteady vortex shedding. From the clean wing to the tubercled wing case at each angle of attack, though, the wake's oscillation became more streamlined, decreasing in amplitude and frequency. These more streamlined wakes were a visual indication that the tubercled wings generated smaller momentum deficits, and thus lower drag, than the clean wings. Also, at 0° and 6° angles of attack, the wake improvements seemed to

be somewhat stronger than those at α = 2° and 4°. These visual impacts aligned with the larger percent drag reductions seen at those two angles. Finally, the tubercles' effect on the wake were likely due to the increase in boundary layer vorticity, although the difference between the vorticity trend (steadily increasing with angle of attack) and the drag reduction trend (decreasing from α = 0° to 2° and then increasing with the higher angles) needs to be investigated further.

Interestingly, the CFD simulation at 0° angle of attack, Re = 5,600 did not show any velocity oscillation within the wake. This lack of oscillation did not match the unsteady, oscillating wake velocity profiles seen in the experimental data. The deviances likely suggest that perhaps a different solver needs to be used in the models to pick up the wake's unsteady characteristics, especially at the lowest Reynolds number. The fact that the simulations at the lowest Reynolds number did not capture any unsteady vortex shedding could also explain why these models did not predict any noteworthy tubercle impacts on the drag. Perhaps the use of an unsteady solver at the lower two Reynolds numbers, combined with a mesh refinement on the tubercles, would provide more interesting drag reduction results than the current models.

5.4: Revised Simulation Summary

A new set of CFD simulations were made to match the experimental models and conditions described in Ch. 4. The addition of tubercles to the wing decreased the drag for all cases except the 6° angle of attack cases at Re = 5,600 and 16,800. For all cases excepting the α = 6°, Re = 20,700 case, the percent drag reductions (or increases) were less than 5 percent. The α = 6°, Re = 20,700 case showed a drag reduction of 21.3 percent.

When compared to the experimental data, the CFD clean wing drag coefficients were generally within 10 percent of the experimental values and within the experimental error bars, with a few exceptions. For the Re = 20,700 case, where the experimental data had the strongest

certainty, all the CFD drag coefficients lay in between the Laitone (1996) and experimental values except for the $\alpha = 6°$ case. Thus, the clean wing models were generally considered accurate to the experimental data.

The CFD percent drag reductions varied significantly from the experimental percent drag reductions. For all cases, the CFD drag reduction magnitudes were substantially smaller than the experimental magnitudes, and for the Re = 5,600 and 16,800 cases, the CFD drag reduction trends did not match the experimental trends. For the Re = 20,700 case, the drag reduction trend did match the experimental trend. Because, for this case, the clean wing drag coefficients generally fell between the experimental and Laitone (1996) values and because its drag reduction trend matched the experimental trend, the CFD models were considered fairly accurate. Differences in drag reduction magnitude could possibly be resolved with mesh refinement around the tubercles.

Due to the large experimental uncertainties discussed in Ch. 4, the large deviances between the CFD and experimental drag reductions at Re = 5,600 cases and 0° and 2° angle of attack cases could in part have been due to experimental overprediction of drag reduction. Perhaps, as the CFD indicated, the tubercles did not affect the drag significantly in these cases. Another possible explanation for the differences was that the CFD underpredicted the drag reduction by not resolving the mesh surrounding the tubercles enough, and thus not capturing the drag-reducing flow mechanisms. To validate this hypothesis, a mesh refinement study on the area surrounding the tubercles would need to be performed to see if a refined mesh changed the drag coefficients at all.

As in the experimental tests, the CFD results left open the hypothesis that tubercles are most effective within other geometric and flow conditions. In fact, with the CFD data showing little to no effect at the lower two Reynolds numbers, the tubercles might be tuned to generate optimal results at a Reynolds number not investigated within this study. A mesh refinement study on the tubercled wing simulations at the current Reynolds numbers could further validate or disprove this

hypothesis. Even more so, additional research into the specifics of bat flight (including more specific flight speeds), bats' use of their ears in flight (including the ear's angle of attack), and the ratios of ear and tubercle characteristic lengths of would help further research to focus on appropriate tests and test models.

Finally, the flow structures generating the drag reduction for the Re = 20,700 cases were investigated. The maximum vorticity as seen in the boundary layer on each model's leading edge increased from the clean case to the corresponding tubercled case. Additionally, the wakes behind the wings became more streamlined with the addition of tubercles. This streamlining of the wakes, likely caused by the increased boundary layer vorticity, provided a helpful visualization of the drag reduction. Also, a lack of wake oscillations seen in the Re = 5,600, 0° angle of attack simulation indicated that the solvers were not capturing the unsteady vortex shedding suggested by the experimental data at that flow condition. This discrepancy with the experimental data could also explain why the models at the lower two Reynolds numbers showed almost no tubercle impact on the drag.

CHAPTER VI

CONCLUSIONS

This work investigated the potential drag reduction caused by Brazilian Free Tailed bat ear tubercles by placing them on a wing's leading edge and comparing the tubercled wing's performance to that of a clean wing. It also performed preliminary analysis on the flow structures generated by the tubercles. The investigation was performed using two methods: computational models and particle image velocimetry (PIV) experimentation. In the first part of the work, initial CFD models of clean and tubercled wings at -5°, 0°, and 5° angles of attack for Reynolds numbers of 5,600 and 16,800 were created, and the models' resulting drag coefficients were compared to prior experimental data (Martin, 2017; Petrin, 2018). When the CFD and experimental drag coefficient results did not match, it was determined that new experimental data was needed to further examine the differences. In the second part of the work, water tunnel PIV was utilized to obtain two-dimensional wake profiles behind clean and tubercled wing sections and drag coefficients were calculated from these profiles. In these experiments, the wing sections were tested at 0°, 2°, 4°, and 6° angles of attack for Re = 5,600, 16,800, and 20,700. In the third part of the work, revised CFD simulations were created to match the experimental test conditions and the flow mechanisms caused by the tubercles were investigated using these new simulations.

The results of this work produced three primary conclusions. The first conclusion was that at $\alpha = 4°$ and 6° for Re = 20,700, these bat ear tubercles, placed on the leading edge of a wing

section, decreased the wing's drag when compared to a clean wing section's drag. This conclusion was made definitively because, for these flow scenarios, both the computational models and the experimental data obtained in this work agreed on the drag reduction trend, although they differed in magnitude. At the other flow cases investigated in this work, no such agreement in drag reduction trends existed between the CFD and experimental data. In these other cases, the lack of agreement was likely due to high uncertainties either in the experimental data (at Re = 5,600 and at $\alpha = 0°$ and 2° for the other Reynolds numbers) or the computational models (at Re = 5,600 and 16,800).

Further investigation into the experimental data at Re = 5,600 showed that both the freestream and wake velocities exhibited clear oscillation patterns. These oscillations were likely due to unsteady vortex shedding off of the wing, but also could have been affected by a slight unsteadiness inherent to the water tunnel flow. Regardless of the cause, not enough data was taken within the experimental tests to obtain an accurate average of the wake's behavior, and thus the resulting drag coefficients exhibited extremely high uncertainties. For the experimental 0° and 2° angle of attack cases, it was concluded that the drag coefficient values' standard deviations were highly sensitive to small differences between measurements, thus resulting in large uncertainties.

For the CFD tubercled wing simulations at Re = 5,600 and 16,800, the resulting drag coefficients changed very little from the corresponding clean wing drag coefficients. These almost negligible tubercle effects, especially when compared to the larger tubercle effects seen in the experimental data, indicated that potentially the CFD models were not resolved enough to capture the drag reduction mechanism. Also, at Re = 5,600, the CFD did not predict any unsteady vortex shedding within the wake. If the low Reynolds number conditions were generating unsteady vortices, as the experimental data seemed to suggest, the fact that the CFD models did not simulate them could also have contributed to the low tubercle impacts on drag.

The second major conclusion of this work was that the CFD models at the Re = 20,700 cases were capturing the drag reduction mechanisms caused by the tubercles. Generally, the clean wing drag coefficients of these models lay within the bounds of the experimental values obtained from this work and the experimental values obtained by Laitone (1996). The experimental bounds were viewed as a reasonable range of drag coefficient values, and thus the clean wing CFD models were considered to be accurately simulating the flow conditions. Additionally, the CFD drag reduction trends at this Reynolds number matched the experimental drag reduction trends. These two facts seemed to indicate that, with accurate baseline clean wing drag data and then with appropriate trends in drag reduction, the tubercled wing models were correctly describing the drag reducing flow structures caused by the tubercles, though perhaps not to the correct magnitude.

This work's third major conclusion was that the tubercles reduced drag by introducing vorticity into the wing's boundary layer. With trustworthy CFD models at Re = 20,700, the flow structures generated by the tubercles could be investigated. Comparisons between the clean and tubercled wing cases at this Reynolds number for all angles of attack showed that the tubercled wing boundary layers saw a higher vorticity magnitude, and thus were more energized, than the clean wing boundary layers. At the $\alpha = 6°$ case, the tubercles also delayed flow separation, resulting from the re-energized boundary layer. Finally, the tubercled wing wakes were more streamlined than the clean wings' wakes, a visualization of the decreased momentum deficit in the tubercled wing cases, likely caused by the increase in vorticity on the wing surface.

Regarding this work's experiments and CFD models, the author suggests two primary recommendations. The first recommendation is to improve the experimental data collection techniques at the Re = 5,600 case. After linking the data's uncertainty at this Reynolds number to wake velocity oscillations, three specific suggestions can be made. First, an empty water tunnel test must be performed to see if the water tunnel flow exhibits any inherent unsteadiness. Results of such a test would either confirm this hypothesis, or if no empty tunnel velocity fluctuations were

detected, verify that the low Reynolds number velocity oscillations were solely due to unsteady vortex shedding. Second, if the tunnel did contain natural unsteadiness, a wing with a smaller chord could be used to allow an increase in freestream velocity while maintaining Re = 5,600. A higher freestream velocity, and thus the drag coefficients, would be less sensitive to fluctuations in the tunnel flow, mitigating some of the large drag coefficient uncertainties. Third, regardless of the velocity fluctuations' source, longer time samples of data must be taken in order to achieve better statistical averages of the flow and thus decrease the drag coefficient uncertainties.

The second recommendation is to perform a mesh refinement study on the tubercled wing CFD cases and to run the lower Reynolds number simulations with unsteady flow solvers. Regarding the mesh refinement study, the cells specifically on and around the tubercles should be refined to see if the current mesh is or is not resolved enough capture the drag-reducing flow mechanisms at the Re=5,600 and 16,800 cases. Unsteady flow solvers should be tried on the models in an attempt to capture the unsteady wake witnessed in the physical experiments. Experimenting with both mesh refinement and different solvers at the lower two Reynolds numbers could either confirm or invalidate the current models' prediction of small tubercle effects on drag.

Outside of this current work, the author recommends investigating the three-dimensional effects of the tubercles. The three dimensional effects could provide insight into discrepancies between the CFD and experimental drag results. Also, a three-dimensional study, either computational or experimental, would provide further insight into the flow structures generated by the tubercles. Finally, the author recommends expanding the scope of investigated Reynolds numbers and angles of attack. The results of this work seem to indicate that the higher the Reynolds number and the higher the angle of attack, the more these tubercles impact drag reduction. A better understanding of the Brazilian free-tailed bat's operating conditions would direct future work towards an optimal flow environment for these tubercles' maximum effectiveness, bringing the research one step closer to realizing tubercles as an applicable passive flow control device.

REFERENCES

Bushnell, D. M., & Moore, K. J. (1991). Drag Reduction in Nature. *Annual Review of Fluid Mechanics*, *23*(1), 65–79. doi: 10.1146/annurev.fl.23.010191.000433

Choi, H., Park, H., Sagong, W., & Lee, S.-I. (2012). Biomimetic flow control based on morphological features of living creatures. *Physics of Fluids*, *24*(12), 121302. doi: 10.1063/1.4772063

Clair, V., Polacsek, C., Garrec, T. L., Reboul, G., Gruber, M., & Joseph, P. (2013). Experimental and Numerical Investigation of Turbulence-Airfoil Noise Reduction Using Wavy Edges. *AIAA Journal*, *51*(11), 2695–2713. doi: 10.2514/1.j052394

Custodio, D. S. (2007). *The Effect of Humpback Whale-like Protuberances on Hydrofoil Performance* (etd-121307-115034) [Master's thesis, Worcester Polytechnic Institute]. Digital WPI. Retrieved from https://digitalcommons.wpi.edu/etd-theses/1111

Davis, R. B., Herreid, C. F., & Short, H. L. (1962). Mexican Free-Tailed Bats in Texas. *Ecological Monographs*, *32*(4), 311–346. doi: 10.2307/1942378

Favier, J., Pinelli, A., & Piomelli, U. (2012). Control of the separated flow around an airfoil using a wavy leading edge inspired by humpback whale flippers. *Comptes Rendus Mécanique*, *340*(1-2), 107–114. doi: 10.1016/j.crme.2011.11.004

Fish, F. E., & Battle, J. M. (1995). Hydrodynamic design of the humpback whale flipper. *Journal of Morphology*, *225*(1), 51–60. doi: 10.1002/jmor.1052250105

Fisher, S. J. F., Alexander, A. S., & Elbing, B. R. (2020). Computational Model of Flow Surrounding Brazilian Free-Tailed Bat Ear Tubercles. *AIAA Scitech 2020 Forum*. doi: 10.2514/6.2020-2021

Hansen, K. L., Kelso, R. M., & Dally, B. B. (2011). Performance Variations of Leading-Edge Tubercles for Distinct Airfoil Profiles. *AIAA Journal*, *49*(1), 185–194. doi: 10.2514/1.J050631

Ito, S. (2009). Aerodynamic Influence of Leading-Edge Serrations on an Airfoil in a Low Reynolds Number. *Journal of Biomechanical Science and Engineering*, *4*(1), 117–123. doi: 10.1299/jbse.4.117

Laitone, E. V. (1996). Aerodynamic lift at Reynolds numbers below 7 x 10 exp 4. *AIAA Journal*, *34*(9), 1941–1942. doi: 10.2514/3.13329

Lee, H. W., & Huang, R. F. (1998). Frequency selection of wake flow behind a NACA 0012 wing. *Journal of Marine Science and Technology*, *6*(1), 29-37.

Lee, S.-I., Kim, J., Park, H., Jabłoński, P. G., & Choi, H. (2015). The Function of the Alula in Avian Flight. *Scientific Reports*, *5*(1). doi: 10.1038/srep09914

Martin, T. (2017). *Flow Modification by Tubercles in Brazilian Free-Tailed Bats* [Master's thesis, Oklahoma State University]. SHAREOK/Oklahoma State University/OSU – Electronic Theses and Dissertations/OSU Theses.

Miklosovic, D. S., Murray, M. M., Howle, L. E., & Fish, F. E. (2004). Leading-edge tubercles delay stall on humpback whale (Megaptera novaeangliae) flippers. *Physics of Fluids*, *16*(5). doi: 10.1063/1.1688341

Pedro, H. C., & Kobayashi, M. (2008). Numerical Study of Stall Delay on Humpback Whale Flippers. *46th AIAA Aerospace Sciences Meeting and Exhibit*. doi: 10.2514/6.2008-584

Pena, B., Muk-Pavic, E., Thomas, G., & Fitzsimmons, P. (2019). Numerical analysis of a leading edge tubercle hydrofoil in turbulent regime. *Journal of Fluid Mechanics*, *878*, 292–305. doi: 10.1017/jfm.2019.611

Petrin, C. E., Caire, W., Thies, M., Elbing, B. R., & Martin, T. (2018). Modification of Drag on the Ear of Brazilian Free-Tailed Bats (Tadarida brasiliensis) via Leading-Edge Tubercles. *2018 Fluid Dynamics Conference*. doi: 10.2514/6.2018-2917

Turner, J. M., & Kim, J. W. (2019). On the universal trends in the noise reduction due to wavy leading edges in aerofoil-vortex interaction. *Journal of Fluid Mechanics*, *871*, 186–211. doi: 10.1017/jfm.2019.314

Williams, T. C., Ireland, L. C., & Williams, J. M. (1973). High Altitude Flights of the Free-Tailed Bat, Tadarida brasiliensis, Observed with Radar. *Journal of Mammalogy*, *54*(4), 807–821. Retrieved from http://www.jstor.org/stable/1379076

Zhou, Y., Alam, M. M., Yang, H., Guo, H., & Wood, D. (2011). Fluid forces on a very low Reynolds number airfoil and their prediction. *International Journal of Heat and Fluid Flow*, *32*(1), 329–339. doi: 10.1016/j.ijheatfluidflow.2010.07.008

APPENDICES

APPENDIX A

The following table describes the individual tests run for each experimental data point. Cells with dashes in them indicate that the value was not able to be calculated. Average and standard deviations were calculated from the bold values, which indicate repeated tests.

Filename	Model	Pump 1 (Hz)	Exposure (µs)	α (deg)	# Total Frames	U (m/s)	Cd	Re_c
Test19_001	Clean	27.8	10000	0	20	--	--	--
Test19_002	Clean	27.8	10000	0	200	**0.183**	**1.88E-02**	**20,500**
Test19_003	Clean	27.8	10000	0	200	**0.184**	**2.35E-02**	**20,600**
Test19_004	Clean	27.8	10000	0	200	**0.184**	**2.11E-02**	**20,600**
Test19_005	Clean	27.8	10000	0	200	**0.184**	**2.95E-02**	**20,600**
Test19_006	Clean	27.8	10000	0	200	**0.183**	**2.21E-02**	**20,500**
					AVG:	0.184	2.30E-02	20,560
					STD:	4.90E-04	3.59E-03	49
Test19_007	Clean	22.6	12000	0	200	**0.149**	**1.83E-02**	**16,700**
Test19_008	Clean	22.6	12000	0	200	**0.151**	**3.23E-02**	**17,000**
Test19_009	Clean	22.6	12000	0	200	**0.149**	**2.41E-02**	**16,700**
Test19_010	Clean	22.6	12000	0	200	**0.149**	**2.11E-02**	**16,700**
Test19_011	Clean	22.6	12000	0	200	**0.149**	**3.02E-02**	**16,700**
					AVG:	0.149	2.52E-02	16,760
					STD:	8.00E-04	5.30E-03	120
Test19_012	Clean	7.6	35000	0	**200**	0.051	3.50E-02	5,770
Test19_013	Clean	7.6	35000	0	**200**	0.051	6.56E-02	5,760
Test19_014	Clean	7.6	35000	0	**200**	0.051	3.07E-02	5,760
Test19_015	Clean	7.6	35000	0	**200**	--	--	--
Test19_016	Clean	7.6	35000	0	**200**	0.051	5.59E-02	5,760
					AVG:	0.051	4.68E-02	5,763
					STD:	0.00E+00	1.45E-02	4

Filename	Model	Pump 1 (Hz)	Exposure (µs)	α (deg)	# Total Frames	U (m/s)	Cd	Re_c
Test20_001	Clean	27.8	10000	2	200	--	--	--
Test20_002	Clean	27.8	10000	2	200	**0.181**	**2.93E-02**	**20,200**
Test20_003	Clean	27.8	10000	2	200	**0.179**	**2.91E-02**	**20,100**
Test20_004	Clean	27.8	10000	2	200	**0.182**	**2.55E-02**	**20,400**
Test20_005	Clean	27.8	10000	2	200	**0.182**	**2.30E-02**	**20,400**
					AVG:	0.181	2.67E-02	20,275
					STD:	1.22E-03	2.65E-03	130
Test20_006	Clean	22.6	12000	2	200	--	--	--
Test20_007	Clean	22.6	12000	2	200	**0.149**	**3.44E-02**	**16,700**
Test20_008	Clean	22.6	12000	2	200	**0.151**	**2.85E-02**	**16,900**
Test20_009	Clean	22.6	12000	2	200	**0.149**	**2.79E-02**	**16,700**
Test20_010	Clean	22.6	12000	2	200	**0.149**	**2.59E-02**	**16,700**
					AVG:	0.150	2.92E-02	16,750
					STD:	8.66E-04	3.16E-03	87
Test20_011	Clean	7.6	35000	2	200	**0.051**	**5.35E-02**	**5,680**
Test20_012	Clean	7.6	35000	2	200	**0.052**	**3.75E-02**	**5,800**
Test20_013	Clean	7.6	35000	2	200	--	--	--
Test20_014	Clean	7.6	35000	2	200	**0.050**	**5.27E-02**	**5,640**
Test20_015	Clean	7.6	35000	2	200	**0.052**	**4.65E-02**	**5,790**
					AVG:	0.051	4.76E-02	5,728
					STD:	8.29E-04	6.40E-03	69
Test9_001	Clean	28	5000	4	20	--	--	--
Test9_002	Clean	28	5000	4	200	0.184	3.49E-02	20,600
Test9_003	Clean	28.2	5000	4	200	**0.186**	**4.13E-02**	**20,800**
Test9_004	Clean	28.1	5000	4	200	**0.185**	**3.70E-02**	**20,700**
Test9_015	Clean	28.1	5000	4	200	**0.186**	**4.17E-02**	**20,900**
					AVG:	0.186	4.00E-02	20,800
					STD:	0.000	2.12E-03	82
Test9_005	Clean	22.8	6000	4	20	--	--	--
Test9_006	Clean	22.8	6000	4	200	**0.151**	**4.42E-02**	**16,900**
Test9_007	Clean	22.8	6000	4	200	**0.155**	**4.57E-02**	**17,300**
Test9_008	Clean	22.8	6000	4	200	**0.153**	**4.75E-02**	**17,200**
Test9_016	Clean	22.8	6000	4	200	**0.151**	**3.85E-02**	**16,900**
Test9_017	Clean	22.8	6000	4	200	**0.151**	**4.46E-02**	**16,900**
					AVG:	0.152	4.41E-02	17,040
					STD:	0.002	3.01E-03	174
Test9_009	Clean	7.4	16,500	4	20	0.051	3.31E-02	5,670

Test9_010	Clean	7.4	16,500	4	200	--	--	--
Test9_011	Clean	7.4	16,500	4	200	0.051	7.76E-02	5,710
Test9_012	Clean	7.4	16,500	4	200	0.050	4.40E-02	5,620
Test9_013	Clean	7.4	16,500	4	200	**0.050**	**5.51E-02**	**5,610**
Test9_014	Clean	7.4	16,500	4	200	**0.050**	**4.17E-02**	**5,650**
Test9_018	Clean	7.4	16,500	4	200	**0.050**	**5.14E-02**	**5,610**
Test9_019	Clean	7.4	16,500	4	200	**0.050**	**3.88E-02**	**5,640**
Test9_020	Clean	7.4	16,500	4	200	**0.050**	**6.06E-02**	**5,600**
Test9_022	Clean	7.4	16,500	4	200	**0.051**	**3.85E-02**	**5,660**
Test9_023	Clean	7.4	16,500	4	200	**0.050**	**6.65E-02**	**5,600**
Test9_024	Clean	7.4	16,500	4	200	**0.050**	**6.36E-02**	**5,560**
Test9_025	Clean	7.4	16,500	4	200	**0.049**	**8.46E-02**	**5,540**
Test9_021	Clean	7.4	16,500	4	200	--	--	--
					AVG:	0.050	5.56E-02	5,608
					STD:	0.000	1.43E-02	37
Test6_001	Clean	25.5	5000	5	20	0.169	3.93E-02	18,900
Test6_002	Clean	26.5	5000	5	20	0.174	4.60E-02	19,500
Test6_003	Clean	28	5000	5	20	0.181	5.48E-02	20,300
Test6_004	Clean	29	5000	5	20	0.190	5.32E-02	21,200
Test6_005	Clean	28.5	5000	5	20	0.190	5.69E-02	21,200
Test6_006	Clean	28.5	5000	5	20	0.188	5.50E-02	21,000
Test6_007	Clean	28.2	5000	5	20	0.187	5.96E-02	21,000
Test6_008	Clean	27.8	5000	5	20	0.186	5.49E-02	20,800
Test6_009	Clean	27.6	5000	5	200	0.183	4.91E-02	20,500
Test6_010	Clean	27.8	5000	5	200	0.184	4.69E-02	20,600
Test6_011	Clean	28	5000	5	200	**0.185**	**5.47E-02**	**20,700**
Test6_012	Clean	28	5000	5	1000	**0.184**	**4.49E-02**	**20,700**
Test6_022	Clean	28	5000	5	200	**0.187**	**4.22E-02**	**20,900**
					AVG:	0.185	4.72E-02	20,767
					STD:	0.001	5.38E-03	94
Test6_13	Clean	23	6000	5	20	0.151	4.13E-02	16,800
Test6_14	Clean	23	6000	5	200	0.151	5.34E-02	17,000
Test6_15	Clean	22.8	6000	5	200	**0.150**	**4.16E-02**	**16,800**
Test6_16	Clean	22.8	6000	5	1000	**0.151**	**4.56E-02**	**16,900**
					AVG:	0.151	4.36E-02	16,850
					STD:	5.00E-04	2.01E-03	50
Test6_17	Clean	7	16500	5	20	0.048	1.02E-01	5,360
Test6_18	Clean	7.5	16500	5	20	0.051	6.00E-02	5,730
Test6_19	Clean	7.3	16500	5	20	0.050	4.22E-02	5,640
Test6_20	Clean	7.3	16500	5	200	0.048	5.28E-02	5,420
Test6_21	Clean	7.5	16500	5	200	0.051	6.50E-02	5,750
Test6_23	Clean	7.4	16500	5	200	**0.050**	**7.24E-02**	**5,620**

Test6_24	Clean	7.4	16500	5	200	**0.050**	**6.70E-02**	**5,580**
Test6_25	Clean	7.4	16500	5	200	**0.050**	**8.80E-02**	**5,560**
					AVG:	0.050	7.58E-02	5,587
					STD:	0.000	8.90E-03	25
Test7_001	Clean	28	5000	6	20	0.185	5.60E-02	20,700
Test7_003	Clean	27.5	5000	6	200	0.181	5.75E-02	20,300
Test7_002	Clean	28	5000	6	200	**0.186**	**6.39E-02**	**20,900**
Test7_004	Clean	28	5000	6	200	**0.186**	**6.29E-02**	**20,800**
Test7_014	Clean	28	5000	6	200	**0.186**	**6.82E-02**	**20,800**
					AVG:	0.186	6.50E-02	20,833
					STD:	0.000	2.31E-03	47
Test7_005	Clean	22.8	6000	6	20	0.151	4.45E-02	16,900
Test7_006	Clean	22.8	6000	6	200	0.151	6.95E-02	16,900
Test7_007	Clean	22.7	6000	6	200	**0.150**	**6.84E-02**	**16,800**
Test7_013	Clean	22.7	6000	6	200	**0.150**	**6.04E-02**	**16,800**
Test7_016	Clean	22.7	6000	6	200	**0.149**	**5.58E-02**	**16,600**
					AVG:	0.150	6.15E-02	16,733
					STD:	0.000	5.19E-03	94
Test7_008	Clean	7.4	16,500	6	20	0.050	5.67E-02	5,630
Test7_009	Clean	7.4	16,500	6	200	0.051	6.58E-02	5,680
Test7_010	Clean	7.3	16,500	6	200	0.049	4.77E-02	5,470
Test7_011	Clean	7.4	16,500	6	200	0.050	5.80E-02	5,600
Test7_012	Clean	7.4	16,500	6	200	**0.049**	**7.56E-02**	**5,500**
Test7_015	Clean	7.4	16,500	6	200	**0.050**	**7.35E-02**	**5,650**
Test7_018	Clean	7.4	16,500	6	200	**0.050**	**5.18E-02**	**5,600**
Test7_017	Clean	7.4	16,500	6	200	--	--	--
					AVG:	0.050	6.69E-02	5,583
					STD:	0.000	1.08E-02	62
Test18_001	Tub	27.7	10000	0	20	--	--	--
Test18_002	Tub	27.8	10000	0	200	**0.184**	**1.88E-02**	**20,600**
Test18_003	Tub	27.8	10000	0	200	**0.184**	**2.85E-02**	**20,700**
Test18_004	Tub	27.8	10000	0	200	**0.184**	**2.28E-02**	**20,600**
Test18_005	Tub	27.8	10000	0	200	**0.184**	**2.15E-02**	**20,600**
Test18_006	Tub	27.8	10000	0	200	**0.185**	**2.55E-02**	**20,700**
					AVG:	0.184	2.34E-02	20,640
					STD:	4.00E-04	3.31E-03	49
Test18_007	Tub	22.6	12000	0	20	--	--	--
Test18_008	Tub	22.6	12000	0	200	**0.151**	**3.77E-02**	**16,900**
Test18_009	Tub	22.6	12000	0	200	**0.150**	**3.23E-02**	**16,800**

Test18_010	Tub	22.6	12000	0	200	**0.150**	**2.77E-02**	**16,800**
Test18_011	Tub	22.6	12000	0	200	**0.150**	**2.61E-02**	**16,800**
Test18_012	Tub	22.6	12000	0	200	**0.151**	**3.32E-02**	**16,900**
					AVG:	0.150	3.14E-02	16,840
					STD:	4.90E-04	4.12E-03	49
Test18_013	Tub	7.6	35000	0	20	--	--	--
Test18_014	Tub	7.6	35000	0	200	**0.051**	**3.57E-02**	**5,710**
Test18_015	Tub	7.6	35000	0	200	**0.051**	**4.17E-02**	**5,760**
Test18_016	Tub	7.6	35000	0	200	--	--	--
Test18_017	Tub	7.6	35000	0	200	--	--	--
Test18_018	Tub	7.6	35000	0	200	**0.052**	**4.11E-02**	**5,770**
					AVG:	0.051	3.95E-02	5,747
					STD:	4.71E-04	2.68E-03	26
Test17_001	Tub	27	10000	2	20	--	--	--
Test17_002	Tub	27.5	10000	2	20	--	--	--
Test17_003	Tub	28	10000	2	20	--	--	--
Test17_004	Tub	27.7	10000	2	200	**0.182**	**2.74E-02**	**20,400**
Test17_005	Tub	27.7	10000	2	200	**0.183**	**3.22E-02**	**20,500**
Test17_006	Tub	27.7	10000	2	200	**0.183**	**2.88E-02**	**20,500**
Test17_007	Tub	27.7	10000	2	200	**0.184**	**3.38E-02**	**20,600**
Test17_008	Tub	27.7	10000	2	200	**0.182**	**2.99E-02**	**20,500**
					AVG:	0.183	3.04E-02	20,500
					STD:	7.48E-04	2.29E-03	63
Test17_009	Tub	22.4	12000	2	20	--	--	--
Test17_010	Tub	22.6	12000	2	20	--	--	--
Test17_011	Tub	22.6	12000	2	200	**0.150**	**3.47E-02**	**16,800**
Test17_012	Tub	22.6	12000	2	200	**0.149**	**2.55E-02**	**16,700**
Test17_013	Tub	22.6	12000	2	200	**0.149**	**2.71E-02**	**16,700**
Test17_014	Tub	22.6	12000	2	200	**0.150**	**3.31E-02**	**16,800**
Test17_015	Tub	22.6	12000	2	200	**0.150**	**3.57E-02**	**16,800**
					AVG:	0.150	3.12E-02	16,760
					STD:	4.90E-04	4.12E-03	49
Test17_016	Tub	7.6	35000	2	20	--	--	--
Test17_017	Tub	7.6	35000	2	200	**0.051**	**1.26E-02**	**5,690**
Test17_018	Tub	7.6	35000	2	200	**0.044**	**8.95E-02**	**4,980**
Test17_019	Tub	7.6	35000	2	200	--	--	--
Test17_020	Tub	7.6	35000	2	200	**0.049**	**4.63E-02**	**5,450**
Test17_021	Tub	7.6	35000	2	200	**0.047**	**3.41E-02**	**5,250**
					AVG:	0.048	4.56E-02	5,343
					STD:	2.59E-03	2.80E-02	261

Test16_001	Tub	27.8	10000	4	20	--	--	--
Test16_002	Tub	27.8	10000	4	200	**0.185**	**3.23E-02**	**20,700**
Test16_003	Tub	27.8	10000	4	200	**0.185**	**3.55E-02**	**20,700**
Test16_004	Tub	27.8	10000	4	200	**0.184**	**3.67E-02**	**20,600**
Test16_005	Tub	27.8	10000	4	200	**0.184**	**3.54E-02**	**20,600**
Test16_006	Tub	27.8	10000	4	200	**0.184**	**4.09E-02**	**20,600**
					AVG:	0.184	3.62E-02	20,640
					STD:	4.90E-04	2.78E-03	49
Test16_007	Tub	22.6	12000	4	200	**0.150**	**3.92E-02**	**16,800**
Test16_008	Tub	22.6	12000	4	200	**0.151**	**4.25E-02**	**17,000**
Test16_009	Tub	22.6	12000	4	200	**0.150**	**3.22E-02**	**16,800**
Test16_010	Tub	22.6	12000	4	200	**0.150**	**3.11E-02**	**16,800**
Test16_011	Tub	22.6	12000	4	200	**0.150**	**4.46E-02**	**16,800**
					AVG:	0.150	3.79E-02	16,840
					STD:	4.00E-04	5.42E-03	80
Test16_012	Tub	7.6	35000	4	200	**0.052**	**3.81E-02**	**5,820**
Test16_013	Tub	7.6	35000	4	200	**0.051**	**1.91E-02**	**5,750**
Test16_014	Tub	7.6	35000	4	200	**0.052**	**3.89E-02**	**5,850**
Test16_015	Tub	7.6	35000	4	200	**0.051**	**4.01E-02**	**5,680**
Test16_016	Tub	7.6	35000	4	200	**0.051**	**4.28E-02**	**5,700**
					AVG:	0.051	3.58E-02	5,760
					STD:	4.90E-04	8.49E-03	66
Test11_001	Tub	28	5000	6	20	0.187	0.0509	21,000
Test11_002	Tub	28	5000	6	200	0.188	0.05892	21,100
Test11_003	Tub	27.5	5000	6	200	0.181	0.04641	20,200
Test11_004	Tub	27.8	5000	6	200	0.186	0.04859	20,800
Test11_005	Tub	27.7	5000	6	200	**0.187**	**0.05825**	**21,000**
Test11_006	Tub	27.7	5000	6	200	**0.186**	**0.05407**	**20,800**
Test11_007	Tub	27.7	5000	6	200	**0.186**	**0.05597**	**20,800**
Test11_008	Tub	27.7	5000	6	200	**0.186**	**0.05479**	**20,900**
					AVG:	0.186	5.58E-02	20,875
					STD:	4.33E-04	1.58E-03	83
Test11_009	Tub	22.7	6000	6	20	0.154	0.05481	17,200
Test11_010	Tub	22	6000	6	20	0.147	0.05809	16,500
Test11_011	Tub	22.3	6000	6	200	0.149	0.06023	16,700
Test11_012	Tub	22.4	6000	6	200	**0.149**	**0.06235**	**16,700**
Test11_013	Tub	22.4	6000	6	200	**0.149**	**0.05579**	**16,700**
Test11_014	Tub	22.4	6000	6	200	**0.149**	**0.05295**	**16,700**
Test11_015	Tub	22.4	6000	6	200	**0.149**	**0.05251**	**16,600**
					AVG:	0.149	5.59E-02	16,675
					STD:	0.00E+00	3.93E-03	43

Test11_016	Tub	7.4	16,500	6	20	--	--	--
Test11_017	Tub	7.4	16,500	6	20	0.05	0.09871	5,630
Test11_018	Tub	7.4	16,500	6	200	**0.05**	**0.04692**	**5,590**
Test11_019	Tub	7.4	16,500	6	200	**0.05**	**0.05893**	**5,550**
Test11_020	Tub	7.4	16,500	6	200	**0.051**	**0.03057**	**5,670**
Test11_021	Tub	7.4	16,500	6	200	**0.05**	**0.02202**	**5,600**
					AVG:	0.050	3.96E-02	5,603
					STD:	4.33E-04	1.43E-02	43

APPENDIX B

The following instructions pertain to the Matlab files titled “import_PIV.m”, “PIV_Wake_Survey.m”, and “PIV_Wake_Survey_TR_Vel.m”. The “import_PIV.m” file is not run directly but is called by the other two files. It opens and formats the data from the text files obtained from DaVis. “PIV_Wake_Survey.m” reads a single DaVis text file, calculates and plots the average wake profile from the text file, uses user inputs to calculate the freestream velocity, and calculates the flow’s Reynolds number and drag coefficient. It also plots 3D vector fields and performs a wake profile and drag coefficient comparison to those obtained from idealized wake theory.

1. Open “import_PIV.m” and “PIV_Wake_Survey.m”. Ensure that the chord (line 9) and the kinetic viscosity value (line 256) are correct.
2. Follow the prompts to choose a single DaVis text file (this file needs to be obtained from the average velocity vector field obtained from DaVis).
3. Once the text file is chosen, follow the prompts to draw a box around the area of interest in the shown velocity color field. Double click inside the box to select the area.

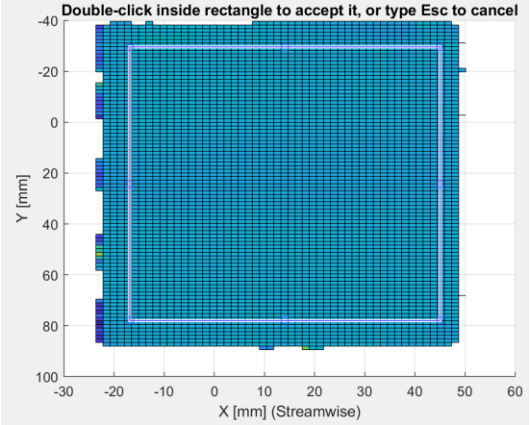

4. The averaged wake profile plot will now display. Use the data tips tool to locate the top and bottom y-values of the wake region (to exclude the freestream regions outside the wake).

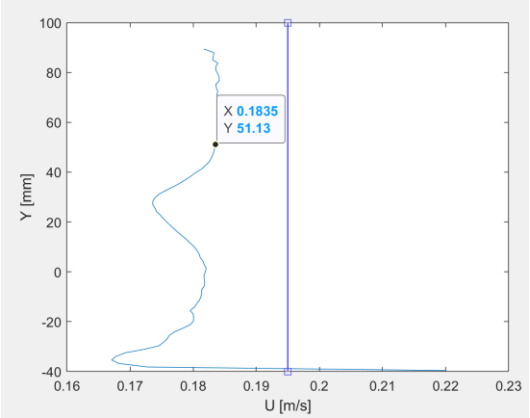

5. Drag the top endpoint of the blue line to an average velocity point in the freestream region above the wake. Drag the bottom endpoint to an average velocity point in the freestream below the wake. The freestream velocity will be calculated from the average of these two endpoints. Double click on the line to continue.

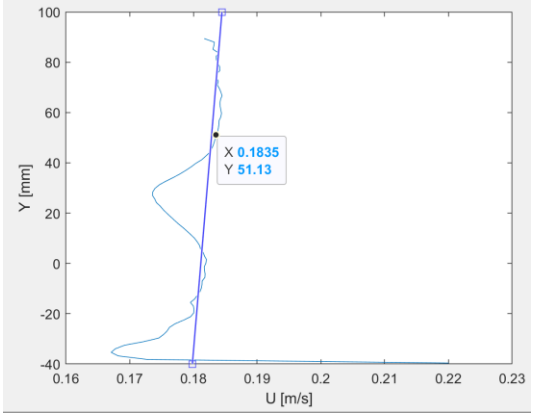

6. Enter the upper y-limit and the lower y-limit with the values obtained using the data tips tool in step 4. These bounds limit the velocity deficit integration for the drag coefficient to the wake region alone and thus mitigate error in the drag coefficient from noise in the wake region.
7. The code will now output values including the freestream velocity, chord-based Reynolds number, and drag coefficient. The code also outputs the drag coefficient of an idealized wake (labeled as "Uncertainty th") and the uncertainty of the calculated drag coefficient (calculated as its difference from the theoretical drag coefficient value and labeled as "Uncertainty"). The code also outputs a non-dimensionalized wake profile graph (Figure 1), a wake profile graph showing the region used to calculate the drag coefficient (Figure 2), a graph comparing the measured wake to the theoretical wake used to calculate the uncertainty (Figure 3), a 3D plot of the wake region (Figure 4), and a 3D plot of the vector field (Figure 5).

"PIV_Wake_Survey_TR_Vel.m" is used to obtain time-resolved velocity data at a given point in the flow field from the text files of individual image pairs. It also calls the file "import_PIV.m".

1. Open “import_PIV.m”, “PIV_Wake_Survey.m”, and “PIV_Wake_Survey_TR_Vel.m”. Ensure that the chord (line 9) and the kinetic viscosity value (line 256) are correct in “PIV_Wake_Survey.m”.
2. Run “PIV_Wake_Survey.m” for the **averaged** velocity vector field text file for the test being analyzed. When the average wake profile plot is open, use the data tips tool to find the y-value of the point at which you want to obtain the velocity value. Make note of that value. This value can either be within the wake or within the freestream. If within the freestream, ensure that the value is definitely outside of the wake, but avoid selecting a value too close to the edge of the field.

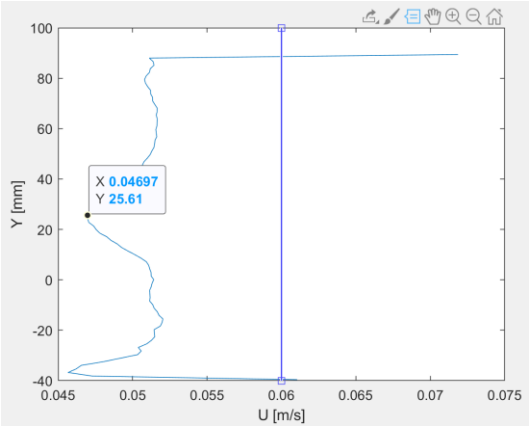

3. Switch to the “PIV_Wake_Survey_TR_Vel.m” tab, leaving the “PIV_Wake_Survey.m” open.
4. The velocity field size, wake y-value limits, and freestream velocity values obtained from the **averaged** velocity vector field text file in “PIV_Wake_Survey.m” will be applied to the individual image pairs analyzed in “PIV_Wake_Survey_TR_Vel.m”. To apply these values, copy the X_Limit, Y_Limit, y_up, y_low, and U_Infty values one at a time from the Workspace window and paste them into their corresponding variable instances at lines 66, 67, 75, 76, and 77, respectively, in the “PIV_Wake_Survey_TR_Vel.m” code.

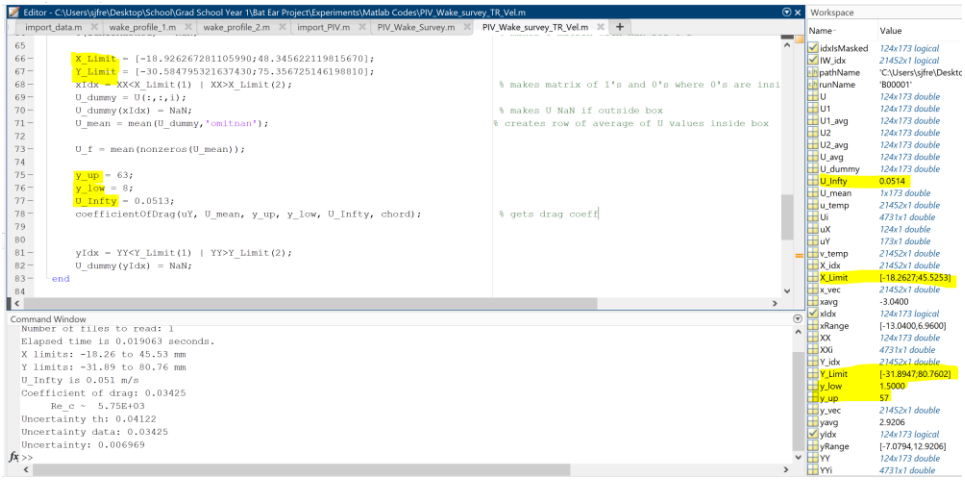

5. In line 96 of the "PIV_Wake_Survey_TR_Vel.m" code, enter the integers above and below the number obtained in step 2. For instance, if the value obtained from step 2 is 15.2, change the code to read: "if Y(i)>(15) && Y(i)<(16)".

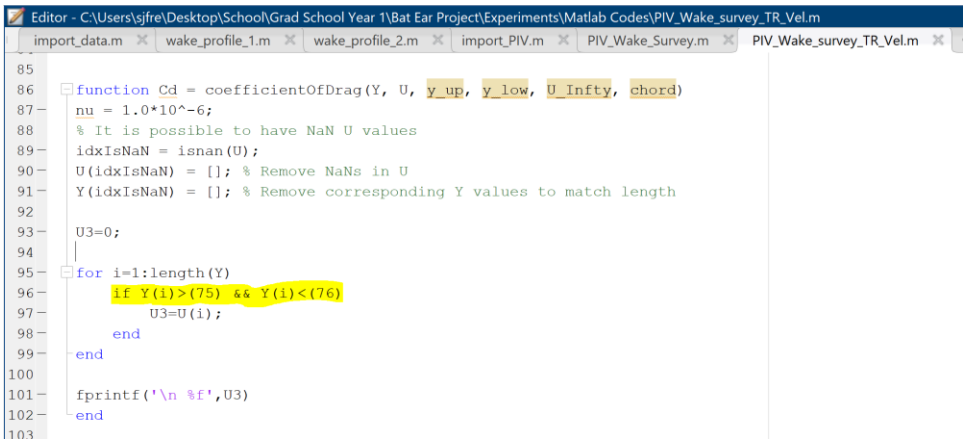

```
function Cd = coefficientOfDrag(Y, U, y_up, y_low, U_Infty, chord)
nu = 1.0*10^-6;
% It is possible to have NaN U values
idxIsNaN = isnan(U);
U(idxIsNaN) = []; % Remove NaNs in U
Y(idxIsNaN) = []; % Remove corresponding Y values to match length

U3=0;

for i=1:length(Y)
    if Y(i)>(75) && Y(i)<(76)
        U3=U(i);
    end
end

fprintf('\n %f',U3)
end
```

6. Now run the "PIV_Wake_Survey_TR_Vel.m" code. When prompted, select all of the text files from the individual image pairs that are to be analyzed.

7. This code outputs the individual velocity values at the y-value selected in step 2 for each of the image pairs selected. As the code currently stands, these values print into the command window and can be copied and pasted into Excel. The code could easily be modified to graph these values, though.

VITA

Sara Joy Fresella Fisher

Candidate for the Degree of

Master of Science

Thesis: COMPUTATIONAL AND EXPERIMENTAL INVESTIGATION OF BRAZILIAN FREE-TAILED BAT EAR TUBERCLES ON AN AIRFOIL LEADING EDGE

Major Field: Mechanical and Aerospace Engineering

Biographical:

Education:

Completed the requirements for the Master of Science in Mechanical and Aerospace Engineering at Oklahoma State University, Stillwater, Oklahoma in May, 2020.

Completed the requirements for the Bachelor of Science in Aerospace Engineering at Oklahoma State University, Stillwater, Oklahoma in 2018.

Completed the requirements for the Bachelor of Science in Mechanical Engineering at Oklahoma State University, Stillwater, Oklahoma in 2018.